

INFORMATION TO USERS

This material was produced from a microfilm copy of the original document. While the most advanced technological means to photograph and reproduce this document have been used, the quality is heavily dependent upon the quality of the original submitted.

The following explanation of techniques is provided to help you understand markings or patterns which may appear on this reproduction.

1. The sign or "target" for pages apparently lacking from the document photographed is "Missing Page(s)". If it was possible to obtain the missing page(s) or section, they are spliced into the film along with adjacent pages. This may have necessitated cutting thru an image and duplicating adjacent pages to insure you complete continuity.
2. When an image on the film is obliterated with a large round black mark, it is an indication that the photographer suspected that the copy may have moved during exposure and thus cause a blurred image. You will find a good image of the page in the adjacent frame.
3. When a map, drawing or chart, etc., was part of the material being photographed the photographer followed a definite method in "sectioning" the material. It is customary to begin photoing at the upper left hand corner of a large sheet and to continue photoing from left to right in equal sections with a small overlap. If necessary, sectioning is continued again — beginning below the first row and continuing on until complete.
4. The majority of users indicate that the textual content is of greatest value, however, a somewhat higher quality reproduction could be made from "photographs" if essential to the understanding of the dissertation. Silver prints of "photographs" may be ordered at additional charge by writing the Order Department, giving the catalog number, title, author and specific pages you wish reproduced.
5. PLEASE NOTE: Some pages may have indistinct print. Filmed as received.

Xerox University Microfilms

300 North Zeeb Road
Ann Arbor, Michigan 48106

73-26,918

STEVENS, Donald Wade, 1936-
DIFFUSION-INDUCED STRESSES AND PLASTIC
DEFORMATION.

The Ohio State University, Ph.D., 1973
Engineering, metallurgy

University Microfilms, A XEROX Company, Ann Arbor, Michigan

DIFFUSION-INDUCED STRESSES AND PLASTIC DEFORMATION

DISSERTATION

Presented in Partial Fulfillment of the Requirements for
the Degree Doctor of Philosophy in the Graduate
School of The Ohio State University


By

Donald Wade Stevens, B.S.Met.E.

* * * * *

The Ohio State University
1973

Approved by


Adviser
Department of Metallurgical Engineering

ACKNOWLEDGEMENTS

The meaningful technical contributions and considerate patience of my adviser, Professor Gordon W. Powell, are very gratefully acknowledged. The interest and suggestions by Professor John P. Hirth were appreciated. Thanks are due Mr. Richard Helferich for general laboratory assistance, Dr. Carl Svank for wet chemical analysis, Mr. George Strable for extensive electron microprobe assistance, Mr. Roland Farrar for scanning electron microscopy assistance, and Mssrs. Neil Farrar and Ross Justus for machine shop assistance.

Funding by the National Defence Education Act and the National Science Foundation is acknowledged.

To my wife, Carolyn, goes my deepest gratitude for her patience and understanding throughout this effort.

VITA

- February 3, 1936.. Born - Pittsburgh, Pennsylvania
- 1958-1960..... Technician, Westinghouse Commercial Atomic Power Department, Forest Hills, Pennsylvania
- 1963..... B.S.Met.E., University of Pittsburgh, Pittsburgh, Pennsylvania
- 1960-1964..... Technician, Assistant Scientist, E. C. Bain Fundamental Research Laboratory, United States Steel Corporation, Monroeville, Pennsylvania
- 1964-1965..... Research Metallurgist, Allison Division, General Motors Corporation, Indianapolis, Indiana
- 1965-1970..... Graduate Student, Research Associate, NDEA Teaching Fellow, Department of Metallurgical Engineering, The Ohio State University, Columbus, Ohio
- 1970-present..... Scientist, Xerox Corporation, Rochester, New York

PUBLICATIONS

Leslie, W. C., Stevens, D.W., and Cohen, M., "Deformation and Transformation Structures in Shock-Loaded Iron-Base Alloys", in High-Strength Materials, V. F. Zackay, ed., New York:J. Wiley Publ., 1965, p. 382.

Leslie, W. C. and Stevens, D. W. "The Magnetic Aging of Low-Carbon Steels and Silicon Iron", Trans. ASM, 57, 261(1964).

FIELDS OF STUDY

Major Field: Metallurgical Engineering

Studies in Diffusion. Professor Gordon W. Powell

Studies in Physical and Mechanical Metallurgy. Professors Gordon W. Powell, John P. Hirth, Joseph W. Spretnak

TABLE OF CONTENTS

	<u>Page</u>
ACKNOWLEDGMENTS.....	ii
VITA.....	iii
LIST OF TABLES.....	vi
LIST OF FIGURES.....	vii
INTRODUCTION.....	1
LITERATURE SURVEY.....	7
EXPERIMENTAL PROCEDURE.....	30
<u>Furnace Description</u>	30
<u>Sheet (couple half) Fabrication</u>	35
<u>Marker Application</u>	37
<u>Welding</u>	37
<u>Diffusion Annealing</u>	47
<u>Bulky Diffusion Couples</u>	49
<u>Sample Analyses</u>	49
RESULTS AND DISCUSSION.....	59
<u>As-Welded Couples</u>	59
<u>Diffusion Penetration</u>	64
<u>Plastic Deformation Penomena</u>	76
Grain Boundary Sliding.....	76
Destruction of Original Crystalline Boundaries, Subgrain Formation, Recrystallization, and Grain Growth.....	78
TEM Substructure.....	78
Surface Deformation.....	87

(continued)

TABLE OF CONTENTS--continued

	<u>Page</u>
Couple Bending.....	90
Internal Cracking.....	94
General Remarks.....	97
<u>Marker Shifting</u>	98
<u>Analyses of Marker Shifting and Couple Bending</u>	109
Introduction to the Hypothetical Models of Mass Flow/ Dislocation Climb.....	109
The Hypothetical Model of Marker Shifting via Mass Flow/ Dislocation Climb.....	113
The Hypothetical Model of Bending via Mass Flow/ Dislocation Climb.....	113
The Hypothetical Model of Marker Shifting and Bend- ing via Mass Flow/Dislocation Climb.....	116
Simplified Bending Stress Analysis.....	124
<u>Porosity</u>	143
Constraining Effects on Porosity.....	143
A Possible Relationship Between Porosity, Marker Shifting, and Bending.....	150
Porosity Shifting and Porosity-Entrapment of Markers.....	152
Porosity Networks.....	156
Porosity Shape.....	168
CONCLUSIONS.....	174
ABSTRACT.....	178
APPENDIX	
A. Thermal Expansion Bending of Thin-Sheet Couples.....	180
B. Measuring Shifting of Markers and Porosity.....	184
C. Computer Calculations of Stress Distributions Across Diffusion Couples.....	188
D. Future Experiment.....	196
LIST OF REFERENCES.....	198

LIST OF TABLES

	<u>Page</u>
1. Atomic misfit in some FCC binary alloys.....	5
2. Chemical diffusion coefficients of various couples.....	73
3. Comparing the extent of interdiffusion in various couples..	75
4. Marker shifting data.....	99

LIST OF FIGURES

	<u>Page</u>
1. Schematic cross sections of hypothetical A/B Kirkendall couples.....	3
2. Schematic of sample furnace and gas train.....	32
3. Furnace tube end assembly.....	34
4. Levigated iron oxide particles.....	38
5. Schematic of a thin-sheet Ag/Au couple.....	39
6. Pressure welding device.....	40
7. Concentration-penetration curve for a 2 μm -deep weld.....	44
8. Concentration-penetration curve for a 6 μm -deep weld.....	45
9. Dual-jet electropolishing unit.....	56
10. As-welded couples with and without markers.....	60
11. As-welded 88 μm -thick couple with a 4 μm -deep weld.....	62
12. As-welded 88 μm -thick couple with a 6 μm -deep weld.....	63
13. As-welded 335 μm -thick couple with a 6 μm -deep weld.....	65
14. Au grains in an as-welded 132 μm -thick couple.....	66
15. A well-behaved concentration-penetration curve from an 88 μm -thick couple.....	68
16. Irregularities in a concentration-penetration curve of an 88 μm -thick couple.....	69
17. Irregularities in a concentration-penetration curve of a 335 μm -thick couple.....	70
18. Irregularities in a concentration-penetration curve of a (bulky) 8 mm-thick couple.....	72

(continued)

LIST OF FIGURES--continued

	<u>Page</u>
19. Grain boundary sliding.....	77
20. Destruction of twin boundaries.....	79
21. Boundary destruction and subgrains.....	80
22. Recrystallization and grain growth.....	81
23. TEM defect structure.....	82
24. TEM subboundaries.....	85
25. Surface deformation of partially-homogenized couples.....	88
26. Examples of diffusion-induced bending.....	91
27. Couple bending vs diffusion time at 750°C.....	92
28. Internal cracking.....	95
29. Marker shifting for a series of semi-infinite 88 μm -thick couples diffused at 750°C.....	101
30. Equivalent marker shifting enhancement due to mechanical constraint or large mass constraint.....	103
31. Summary of marker shifting in Ag/Au couples diffused at 750°C.....	105
32. Markers in the couple 88 μm / 750°C/ 0.52 hr.....	108
33. Markers in couples having different amounts of porosity...	109
34. Hypothetical models of marker shifting or couple bending, both via mass flow/dislocation climb.....	111
35. Simultaneous marker shifting and couple bending.....	117
36. Relative error in measuring mass flow when couple bending is ignored.....	119
37. Comparing the observed and calculated values of enhanced marker shifting.....	122

(continued)

LIST OF FIGURES--continued

	<u>Page</u>
38. The stress distribution across 88 μm -thick couples diffused at 750°C.....	132
39. Variation of stress with time at the end of 88 μm -thick couples.....	135
40. Effect of couple thickness (mass constraint) on the stress distribution across identically-diffused couples.....	138
41. Effect of couple thickness (mass constraint) on the stress distribution of couples having the same fraction of inter-diffusion.....	139
42. Bending stress vs couple thickness and $C^2/4Dt$	141
43. Growth and shifting of porosity.....	144
44. Effect of couple thickness (mass constraint) on the amount of porosity in identically-diffused couples.....	146
45. Effect of mechanical constraint on the amount of porosity in identically-diffused couples having different thicknesses.....	147
46. Decreased porosity growth by mechanical constraint.....	148
47. Shifting of porosity and markers in semi-infinite, 88 μm -thick couples diffused free of mechanical constraint at 750°C.....	154
48. Porosity networks in partially-homogenized couples.....	157
49. Porosity network in a couple in the very early stage of homogenization.....	159
50. Porosity network in the semi-infinite couple 335 μm / 750°C/ 1.48 hr.....	160
51. Porosity network in a couple diffused to about its semi-infinite limit.....	162
52. Porosity networks in the semi-infinite couples 88 μm / 750°C/ times shown.....	163
53. Polyhedral pores in the semi-infinite couple 88 μm / 750°C/ 1.98 hr.....	170

(continued)

LIST OF FIGURES--continued

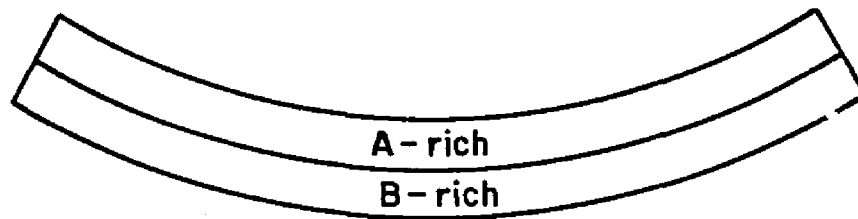
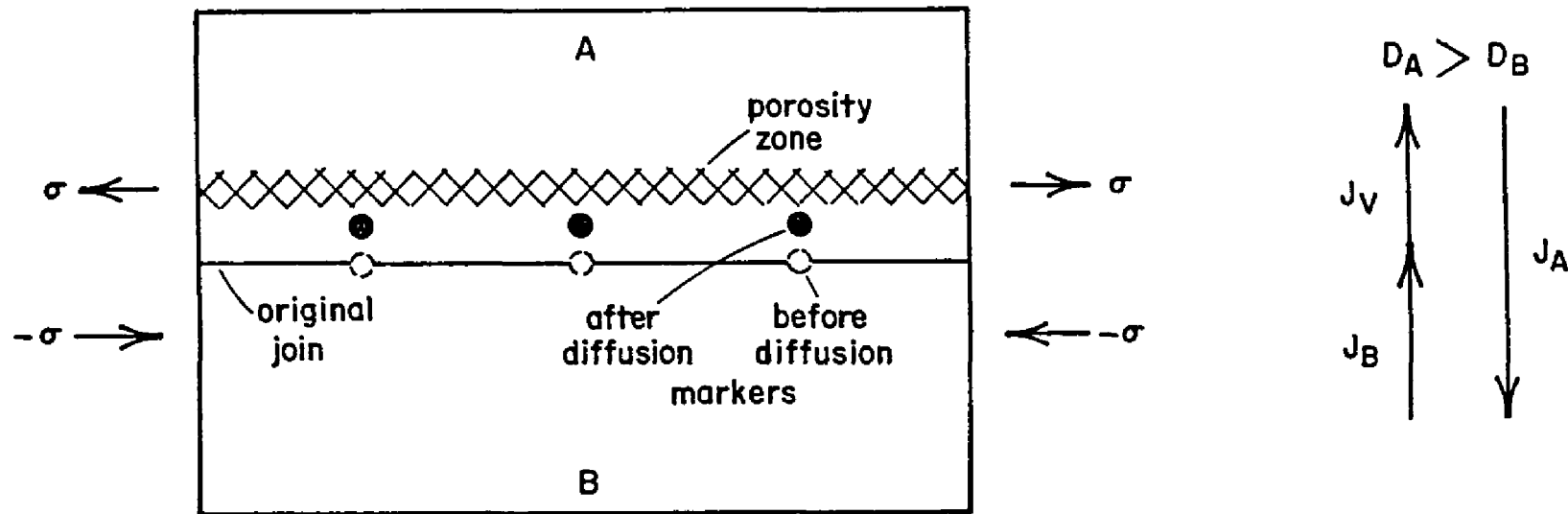
	<u>Page</u>
54. Porosity network open to the couple terminal surface.....	171

INTRODUCTION

During interdiffusion in binary metallic couples which form substitutional alloys, one of the metals exhibits a higher rate of diffusion than the other. No exceptions to these unequal diffusion rates has been reported, and the vacancy mechanism of diffusion is dominant in FCC alloys.¹ These unequal rates give rise to mass flow across the couple in the direction of the slower-diffusing metal, with vacancy flow and marker migration in the opposite direction. The mass flow and marker shifting phenomena together are known as the Kirkendall effect.² Porosity usually develops in the side of the faster-diffusing element because the vacancy flow into that side supersaturates the lattice with vacancies.^{2,3-6} Instead of precipitating at pores, some of the excess vacancies in the lattice are annihilated at internal sinks such as dislocations, grain boundaries, etc.^{3,6-10} This causes the lattice to contract, thereby placing the fast-diffusing side of the couple in tension. The opposite side of the couple is undersaturated in vacancies because of a gain in mass. Thus, this side of the couple tends to expand by creating lattice sites, thereby placing the side of the slower-diffusing element under compression. Consequently, when chemical stresses due to nonequilibrium vacancy concentrations are relieved by annihilating or creating lattice sites, the resultant volume changes can develop stresses in the interdiffusion zone.⁶⁻⁸ Stresses due to volume changes which arise from lattice parameter differences (atomic misfit) also can be induced during interdiffu-

sion.^{6,9-26} These amount to only a small fraction of the stresses caused by the presence of vacancy gradients in common FCC-metal couples such as Cu/Zn,^{2,9,10,12} Cu/Ni,⁶ and Ag/Au,²⁷ but can be very large in very high-misfit systems such as doped semiconductors.¹⁶⁻²⁶ Diffusion-induced stresses are three-dimensional at their inception, but the component parallel to the diffusion direction is commonly thought to relax to a negligibly-small value. This conclusion is based on the assumption that the couple material can elastically contract or expand freely in the diffusion direction.^{3,6-8,10,12} However, the couple mass is welded into an integral body which is not free to contract or expand in directions perpendicular to diffusion. Therefore, the two-dimensional stresses in these directions are not relieved by mass flow. A planar view of diffusion-induced stresses, marker shifting, and porosity are depicted schematically in Fig. 1(a) for a typical bulky Kirkendall couple comprised of hypothetical metals, A and B. The vast majority of investigations of chemical diffusion have involved solid/solid bulky couples having dimensions on the order of mm or cm. In the few cases where solid/vapor^{6,16} or solid/solid²⁷ couples were made very thin in the direction of diffusion, overall bending of the couples occurred as depicted in Fig. 1(b). (The side richest in the faster-diffusing element always forms the inner, concave surface). Two mechanisms have been proposed to explain bending. Barnes⁶ and Queisser¹⁶ attributed bending of their solid/vapor couples to diffusion-induced stresses. Barnes attributed these stresses in his Cu/Ni couples to vacancies and atomic misfit (mostly vacancies), whereas Queisser attributed them to misfit alone in his (high-misfit) Si/B

a) typical bulky couple



b) bending, thin-sheet couple

D_i = intrinsic diffusion coefficient of i , cm^2/sec

J_i = flux of i , $\text{moles}/\text{cm}^2 - \text{sec}$

σ = diffusion-induced stress

Fig. 1. Schematic cross sections of hypothetical A/B Kirkendall couples.

couples. As a second bending mechanism, Liu and Powell²⁷ suggested that dislocation climb parallel to the diffusion direction could have contributed to bending of their Ag/Au couples. The climb would occur to accommodate mass flow across the interdiffusion zone. They also noted that bend-producing climb would not contribute to marker shifting. However, nothing was known about marker shifting in thin-sheet couples to test this possibility. In fact, little else was known about bending couples except that substructure formed in them.^{6,16,27} In contrast to the scant knowledge of thin, bending couples, much was known of bulky, nonbending couples. Bulky couples have exhibited marker shifting and porosity, and various stress-induced plastic deformation phenomena occur in the interdiffusion zone. These are the destruction of the original crystallinity,^{6,12,28,29} the generation of dislocations or substructure,^{6,12,13,16-26,28} recrystallization,^{3,12,28,29} surface deformation^{12,28} and internal cracking,^{9,30,31} Diffusion-induced stresses also have been said to create⁸ or aid¹⁰ porosity formation. Information concerning these same phenomena in thin-sheet couples is sought here to describe and understand better the role of diffusion-induced stresses and plastic deformation in Kirkendall couples, especially with regard to bending. Also, such information would hopefully be useful to the recent technology of diffusion bonding of engineering components, especially with regard to thin-sheet laminate composites.³²

The Ag-Au system was selected for study in the present work primarily because it displays extremely little atomic mismatch^{15,33,34} or volume change³⁵ upon mixing, as indicated in Table I. This essen-

Table 1. Atomic misfit in some FCC binary alloys.

<u>Binary</u>	<u>% Atomic Misfit^a</u>	
	<u>25°C^b</u>	<u>720°C^c</u>
Ag-Au ^d	0.18	0.54
Cu-Ni ^d	2.54	
Au-Pd ^d	4.71	
Ag-Pd ^d	4.90	
Cu-Pd	7.35	
Ni-Pd ^d	9.89	
Au-Cu	12.05	
Ag-Cu	12.24	
Au-Ni	14.59	
Ag-Ni	14.78	

^aAtomic misfit is calculated from the atomic radii of the binary components, A and B, according to $\frac{|r_A - r_B|}{(r_A + r_B)/2}$.

^batomic radii from Pearson³⁴.

^catomic radii from high-temperature lattice parameters determined by Warlimont³³. The very small atomic misfit in Ag-Au is additionally supported by the maximum change in volume being only 0.63% upon forming homogeneous solid solutions at 600°C, and nearly zero for liquid solutioning³⁵.

^dBinary phase diagrams^{34,36} show complete mutual solubility with no ordering or immiscibility at temperatures generally employed in diffusion experiments.

tially eliminates the complicating factor of atomic misfit stresses in the interdiffusion zone. Thus, practically all diffusion-induced stresses in Ag/Au couples can be attributed to nonequilibrium vacancy concentrations created by the unequal diffusion rates of Ag and Au ($D_{Ag} \sim 2.5 D_{Au}$ in their alloy at 750°C^*). Also, the Ag-Au system is single-phase FCC with complete mutual solubility,^{34,36} and the univalent Ag and Au are immediate neighbors in Group 1B of the periodic table. Furthermore, Ag-Au diffusion kinetics are well-established,³⁸⁻⁴⁵ and a reliable method for determining the system's composition gradient by electron microprobe X-ray analysis is known.⁴⁶

*This constitutes a significantly large (but not the largest) Kirkendall effect relative to other FCC Kirkendall systems³⁷. However, other binary systems have moderate to large atomic misfits, as seen in Table I.

LITERATURE SURVEY

The Kirkendall effect in substitutional binary alloys was first described by Smigelskas and Kirkendall.² They found that molybdenum marker wires placed at the original join of their Cu/brass couples shifted parabolically toward the brass side during diffusion (marker shift = constant $\sqrt{\text{time}}$, or $X_m = kt^{\frac{1}{2}}$), indicating that Zn diffused more rapidly in alpha brass than did Cu. Volume differences due to lattice parameter changes during alloying accounted only for one-fifth of the shift. Etch pitting susceptibility on the brass side of the couple interface was interpreted as a decrease in brass density, which supported their contention that Zn was leaving the brass side faster than it was being replaced by the incoming Cu. Smoluchowski⁴⁷ stated that the above experiment convincingly indicated that, in addition to the two kinds of atoms, a third constituent, vacancies, was moving during diffusion. C. S. Smith¹¹ discussed the necessity of voids due to the net mass loss on the brass side; he also postulated that lattice parameter strains in the interdiffusion zone could result in extended lattice dislocations, slip, and microscale fissuring. Smith,¹¹ Mehl,⁴⁸ and Darken⁴⁹ concluded that Smigelskas and Kirkendall's results required that individual diffusion coefficients be assigned to each of the two diffusing atom species. Shortly afterward, Darken⁵⁰ derived expressions for the intrinsic coefficients in his analysis of the Kirkendall effect, and included phenomenological relationships between the various diffusion coefficients (tracer, intrinsic, and

chemical) and marker velocity. Based on the assumptions of (1) constant cross section area perpendicular to the diffusion flow, (2) constant molar volume throughout the couple, and (3) no porosity, Darken showed that

$$D = D_{ANB} + D_{BNA} \quad \dots 1$$

$$D_i = D_i^* \left(1 + \frac{\partial \ln \gamma_i}{\partial \ln N_i} \right) \quad i = A \text{ or } B \quad \dots 2$$

$$v_m = (D_A - D_B) \frac{\partial N_A}{\partial x} = \frac{X_m}{2t} \quad \dots 3$$

, where

D = chemical interdiffusion coefficient in a binary A/B couple, as determined by the Boltzman-Matano method.^{51,52}

D_i = intrinsic diffusion coefficient of A or B in alloy A+B.

D_i^* = radioactive tracer diffusion coefficient of A or B in a chemically homogeneous alloy A+B.

N_i = mole fraction of A or B.

γ_i = thermodynamic activity coefficient of A or B in alloy A+B.

v_m = marker velocity.

X_m = marker shift which occurs during isothermal diffusion time, t .

$\frac{\partial N_A}{\partial x}$ = slope of the concentration-penetration curve at the marker plane.

This treatment requires that the vacancy concentration to be the equilibrium value at all points in the diffusion zone. Darken's Eqn. 3 implies that all of the mass flow which occurred in the couple is given by the volume of material through which the markers moved. It is seen in Fig. 1(a) that this volume is given by the marker shift multiplied by the couple area normal to direction of marker shifting.

After deriving the above expressions, Darken showed that Eqns. 1 and 3 described reasonably well the Kirkendall behavior which was experimentally observed in a marker shifting study of Cu- α brass.² and that Eqns. 1 and 2 described, within experimental error, the diffusion behavior of the Ag-Au system³⁸ as determined from tracer diffusion experiments. A very extensive tracer diffusion study by Reynolds, Averbach, and Cohen³⁰ showed that Darken's relationships between tracer diffusivity and thermodynamic activity, given by Eqns. 1 and 2, describe well the Au-Ni system.

However, problems have been met in applying direct* marker shifting results to (Darken's) Eqns. 1 and 3, one of the problems being erratic, nonuniform marker shifting. While marker distributions within individual couples which contain several markers are not generally reported, radiation intensity distributions of tracer oxide markers in Ag/Au couples indicate that the markers in any given couple are scattered over a distance comparable to their "computed average" marker shift.^{42,45} It is more common to report only the computed average marker shift for each couple. When a series of like couples is diffused isothermally for various times, the average marker shifts of many of the couples deviate from the average parabolic shifting rate of the series. While these deviations sometimes amount to only a few percent,^{53,54} they are often significantly higher, and can be up to $\pm 25\%$,⁵⁵ and $\pm 50\%$. Reynolds et al.³⁰ found marker shifting to be too inconsistent to describe the Kirkendall effect in their Au/Ni couples.

*A "direct" marker shift is the difference between the marker positions measured directly from the couple before and after diffusion.

Da Silva and Mehl³ showed that direct marker shifting measurements in their various FCC couples was a "most unreliable" means of measuring the Kirkendall effect. Instead, they took the Matano plane to be the prediffusion position of the markers, employing graphical area measurements from concentration-penetration curves to determine the Matano plane (this is known as the "indirect" measure of marker shifting). Hartley et al.⁵⁶ experienced similar difficulties in BCC couples, often obtaining negative values for the chemical diffusion coefficients when using direct marker shifting results according to (Darken's) Eqns. 1 and 3. Kohn et al.⁵³ performed a careful experiment to test the Kirkendall effect in the Fe-Ni and Fe-Co systems by comparing results obtained from both tracer and marker methods. They showed that the Kirkendall effect predicted by theory is 2-3 times smaller than that actually displayed by marker shifting (the theory included both Darken's equations and Manning's modification of Darken's equations, which incorporates the vacancy wind effect). Dallwitz⁵⁷ also found a serious disagreement between the theoretical Kirkendall effect and that calculated from (wire) marker shifting data in Ag/Au couples. Part of the discrepancy between theory and experiment was believed due to some of the markers lying within pores⁵⁷ and spurious marker shifting caused by plastic deformation phenomena in the diffusion zone, such as the destruction of original crystallinity, polygonization, and recrystallization.^{3,53,56} These plastic deformation phenomena and some other features of Kirkendall couples are presented below.

An early, systematic verification of the Kirkendall effect was performed by da Silva and Mehl³. They varied several fabrication and

diffusion parameters in order to ascertain that the Kirkendall effect was real and not a consequence of the properties of the markers, imperfect joining, pre-existing porosity, degassing, or volatile mass transfer. To this end, they varied diffusion temperatures, heat treating atmospheres, couple fabrication techniques, couple dimensions, marker materials, and marker geometries in several binary alloy systems, Cu-Zn, Cu-Al, Cu-Sn, Cu-Ni, Cu-Au, and Ag-Au. Despite relatively large scatter in marker shifting data exhibited within any given alloy system, their experiments essentially confirmed the parabolic marker shifting behavior in Kirkendall-type couples. The rate constants, k , in $X_m = kt^{\frac{1}{2}}$ depended strongly on the metals and alloys from which the couples were made, as expected from Darken's analysis, Eqn. 3, where $D_A - D_B$ would vary according to the binary system. The marker motion was always in the direction of diffusion flow. Markers placed to detect lateral shifting (perpendicular to the diffusion flow) revealed that no such shifting resulted from the mass flow effect. Furthermore, the lateral markers shifted only one-tenth of the amount predicted from changes in the lattice parameter which occurred upon alloying in the interdiffusion zone. Thus, da Silva and Mehl concluded that changes in couple dimensions which occurred during diffusion were limited to the direction of diffusion flow.

Da Silva and Mehl's couples were made from round slabs which were either 6 or 12 mm-thick in the diffusion direction. Grain sizes were varied in some of these couples. On the basis that marker shifting was independent of slab thickness and grain size, they concluded that neither the sample surfaces nor grain boundaries were acting as pri-

mary sources or sinks for vacancies and, therefore, the net vacancy fluxes were occurring within the grains of the diffusion zone. This was in contrast to an earlier suggestion by Seitz⁵⁸ that grain boundaries and couple surfaces could be sources and sinks for point defects during the diffusion process. Da Silva and Mehl found porosity in the diffusion zone in some of their couples. It was always located on the side richest in the faster diffusing element. They noted that porosity in Cu-Zn couples was greatest near the markers and was located at some of the markers in the Cu-Zn and Cu-Al couples. The multigrain boundary which formed along the original join during welding was observed to migrate with the markers, and was interpreted as grain growth which possibly resulted from strain accompanying diffusion.

Da Silva and Mehl³ rationalized the existence of marker shifting, porosity, and dimensional changes by employing the vacancy mechanism of diffusion. Their selection of the vacancy mechanism was based, in part, on the argument by Seitz⁵⁸ that diffusion by direct atom interchange could not account for marker shifting; neither could Zener's⁵⁹ cooperative ring rotation mechanism. Da Silva and Mehl proposed that nonequilibrium vacancy concentrations within the diffusion zone on either side of the couple could be eliminated by forming edge dislocations. They suggested that these dislocations could be formed on the porous (excess vacancy) side by vacancies occupying former atom sites along a lattice row which was perpendicular to the diffusion flow. Interstitials would align accordingly on the nonporous side to form dislocations of opposite sign. Edge dislocations formed in this manner would result in the destruction of lattice sites on one side of

the couple and the creation of lattice sites on the opposite side. As the matrix relaxes in a direction parallel to the diffusion flow in order to accommodate the above process, markers would be displaced in a direction parallel to the diffusion flow. The authors felt that matrix relaxation, which was due to the formation of either dislocations or pores, was uninhibited in the direction of diffusion. The lack of similar relaxation in the lateral direction was presumed to be due to "...the elastic restraint of the couple as a whole that restricts contraction to the plane perpendicular to (the) direction of diffusion flow." Mott⁶⁰, in an analysis of vacancy formation at edge dislocation jogs, supported da Silva and Mehl's explanation of point defect condensation along edge dislocations. Also, he attributed porosity to the direct condensation of vacancies into macroscopic holes.

Shortly following the early work on the Kirkendall effect by Smigelskas and Kirkendall² and Darken⁵⁰, the vacancy mechanism of diffusion was treated from the standpoint of kinetic theory^{58,61,62}, and certain corresponding agreements with Darken's results were shown⁶². A condition required to correlate the vacancy diffusion mechanism with Darken's analysis was that vacancies are maintained in local thermal equilibrium. Grain boundaries and dislocations, acting as sources or sinks for vacancies, were to help maintain the required equilibrium⁶². Bardeen and Herring^{7,63} incorporated the above concepts in their treatment of vacancies in Kirkendall couples. Of particular interest here is their treatment of edge dislocations operating as sources or sinks for vacancies when in the presence of a thermodynamic chemical potential, μ_v , due to nonequilibrium vacancy concentra-

tions. They derived the relationship

$$\mu_V = kT \ln(n_V/n_V^e)$$

, where n_V , n_V^e = actual and equilibrium number of vacancies, respectively, in the diffusion zone. They next adopted Shockley's⁶⁴ suggestion that end-pinned edge dislocations could form a climbing analog of the Frank-Read source, and thus could operate as continuous sources or sinks for vacancies. Bardeen and Herring then calculated that vacancies could exert a chemical stress on dislocations according to

$$\sigma_{ch} = \mu_V/\Omega_0$$

, where Ω_0 = atomic volume. Equating the chemical stress to that required for "bow-out" operation of a climbing dislocation, they found that a mere 1% supersaturation, S , (or undersaturation) of vacancies could operate a regenerative climbing dislocation source, where

$$S = \frac{n_V}{n_V^e} - 1$$

Thus, the chemical potential of vacancies could be maintained very near their equilibrium value during Kirkendall diffusion by climbing dislocations which act as very effective sources or sinks. Bardeen and Herring⁷ also noted that the lack of lateral dimension changes in da Silva and Mehl's³ Cu/brass couples indicated a preferential growth of planes oriented perpendicular to the diffusion flow. To explain this, they proposed that preferential growth occurs for dislocation rings which lie in planes perpendicular to the diffusion flow, these planes being in the rapid diffusion zone where there is an unbalance of vacancies. Dislocation rings oriented parallel to the diffusion flow could also serve as sinks or sources, but these would grow out of the

region of vacancy unbalance and would eventually become disfavored.

The continued operation of the Bardeen-Herring (B-H) source requires that the climbing edge dislocation be pinned at its ends, such as by screw dislocations. In addition to pure edge dislocations, mixed dislocations can climb under chemical stresses created by vacancy supersaturations (osmotic forces); helical dislocations are formed in this manner.⁶⁵ Spiral dislocations can be similarly formed by pinning only one end of a climbing edge dislocation.⁶⁶ All of these climb mechanisms can operate under the same supersaturation of $\sim 1\%^*$. In TEM (transmission electron microscopy) studies, B-H sources⁶⁹ and helical dislocations⁷⁰ have been observed in quenched metal alloys having large vacancy supersaturations, and chemical stresses developed during diffusion have operated B-H sources in Au-doped Si.²⁶ However, B-H sources were not found in Ag/Au²⁷ or Cu/brass¹³ couples.

The very early experiments on the Kirkendall effect^{2,3} resulted in some metallographic evidence of stress in the diffusion zone (slight grain boundary motion, distorted marker positions). In a study of the Kirkendall effect, Barnes⁶ obtained convincing evidence of high stresses and plastic deformation in the diffusion zone by employing metallographic and X-ray diffraction techniques. Twin boundaries in the diffusion zone of his Cu/Ni couples ($D_{Cu} > D_{Ni}$) were observed to be curved, and some unidentified boundaries appeared as weak ghost boundaries. These boundary observations in the diffusion zone were taken as evidence of localized, violent distortion. Microfocussed back

*Generalized treatments of the osmotic forces produced by vacancies on dislocations can be found in texts by Hirth and Lothe⁶⁸ and Weertman and Weertman⁶⁷.

reflection Laue X-ray photographs revealed, via spot splitting, polygonization (substructure) in the same zones, the angle between each polygon being about 2° . The same X-ray technique was later used by Bolk²⁸ to show that substructure formed in his Au/Pt couples.

Barnes⁶ also investigated marker shifting and porosity in his Cu/Ni couples, employing as markers the small inclusions which existed naturally at the original join; this is often referred to as "welding debris".* By monitoring the density and external dimensions of his couples, he observed that the Cu/Ni couples underwent swelling, principally in the direction of diffusion flow. He also observed swelling in Cu/ α -brass couples by placing tungsten wire markers in the Cu material which was outside the interdiffusion zone, then comparing their shifting with those which were placed at the original join. Swelling was indicated by the outer markers shifting in a direction opposite of the Kirkendall markers. He attributed the swelling in both types of couples to void growth which developed from the condensation of excess vacancies. Observing that the volume occupied by the voids was only a fraction of the amount of vacancy flow indicated by marker shifting,** Barnes concluded that many vacancies were eliminated from the lattice by means other than condensation at the voids. He experimentally ruled out the couple surface as a sink or source by

*This practice, used by Barnes and others,^{5,44,56,71} is based on the observation of da Silva and Mehl³ that the moving boundary marked by welding debris is the actual marker (Kirkendall) interface. Conversely, it has been shown that this interface shifts measurably slower than inert markers placed purposely at the original join⁵⁷.

**In his analysis, Barnes assumed (as have others^{8,72}) that vacancies occupy the same volume in the voids as they do in the lattice. This is probably a poor assumption.

(1) diffusing couples comprised of sandwich stacks containing up to 48 welded strips (alternately Cu and Ni), then (2) observing that the outermost couples contained the same amount of porosity as the innermost. From this, Barnes concluded that vacancy sinks and sources were operating within the diffusion zone in the form of grain boundaries, subboundaries, or edge components of dislocations. Their operation would place the lattice in a tensile or compressive state of stress by the annihilation or generation of vacancies, respectively. These stresses could plastically deform the metal in the form of shrinkage where vacancies are annihilated, or expansion where they are created. The resulting dimensional changes would occur in directions having the least restraint. (This is the mass constraint effect described earlier³).

Barnes⁶ observed that many of the pores in his Cu/Ni couples had crystallographic (polyhedral) shapes. He attributed this to crystallographic faces having a lower surface energy than spherical voids, and that surface diffusion would allow the voids to adopt the lower energy configuration. His explanation was based in part on knowing that single crystal spheres of rocksalt assume crystallographic shapes upon annealing. Barnes' argument is further supported by the later work of Sundquist⁷³, who developed crystallographically-shaped (polyhedral) particles by annealing micron-sized condensed droplets of Ag, Au, Ni, Cu, and Fe. Sundquist calculated that the polyhedral shaping of the initially-rounded droplets was due to a minimization of surface energy. Additional indirect support is given by the inert gas bubbles formed in Cu by irradiating with 100 KV argon ions, then

annealing under hydrostatic pressure to grow bubbles. TEM studies show such bubbles to have polyhedral shapes along low indice planes.⁷⁴ Also, polyhedral pores form along low indice planes in Ni when vacancies precipitate out of Ni foils, the vacancies being created by electron bombardment during high energy (1MV) TEM of the thin foils.⁷⁵

A dramatic demonstration of the Kirkendall effect for a wide variety of binary metal systems (Cu-Ni, Ag-Au, Cu-Ag, Cu-Fe, Fe-Ni, Cu-Zn, Ni-Zn, Cu- α brass) was obtained by Kuczynski and Alexander⁴ by wrapping thin wires of one metal around a cylinder of its complementary binary metal, diffusing the wrapped sample, then metallographically observing the cross sections. Mass flow effects from unequal diffusion rates of the binary elements caused the wire of the slower-diffusing element to sink into the matrix of the faster-diffusing element (called "digging" by the authors). Porosity was often observed in the diffusion zone rich in the faster-diffusing material.

The density and shape of porosity were metallographically observed by Balluffi and Alexander⁵ in the Kirkendall systems Cu-Ni, Ag-Au, and Cu- α brass. They concluded that pore formation did not depend on the surface of solid/vapor because 0.14 mm-thick couples displayed the same amount of porosity as 2 mm-thick couples. The pores were often polyhedral in shape in the early stages of diffusion but became rounded after considerable diffusion, reportedly a sintering effect. For a given weight loss of Zn during dezincification*, porosity density decreased with increasing temperature. This, too, was attributed

*Dezincification, which occurs because $p_{Zn} \gg p_{Cu}$ and $D_{Zn} > D_{Cu}$, is carried out by heating brass in vacuum in order to obtain an outward flux of Zn.

(possibly) to sintering.

Seitz⁷² attempted to interpret the formation of voids in Kirkendall couples in terms of vacancy condensation at heterogeneous nucleation sites within the diffusion zone. He pointed out that his analysis was hampered by a lack of knowledge concerning the origin, size, and distribution of stable pore nuclei, and by the lack of agreement between different investigators concerning their observations of the density and distribution of porosity in similar couples of either Cu/Ni, Cu/Zn, or Ag/Au.

Balluffi⁷⁶ employed part of Seitz's analysis⁷², plus experimental porosity observations made by himself and others, to calculate that voids could form from vacancy supersaturations via heterogeneous nucleation at second phase impurity particles in the matrix and at the original join of Kirkendall couples. Excess vacancy concentrations of 0.01 or less were calculated to be sufficient for this purpose.

Balluffi and Seigle⁹ metallographically examined dezincified brass sheets and found that porosity was affected by both sheet thickness and grain size. The grain boundaries in their thinnest sheets ($\sim 15 \mu\text{m}$) acted as very effective sinks, resulting in a scarcity of pores near the boundaries and causing a contraction of the specimen in a direction perpendicular to the boundaries. This shrunk the samples in directions both parallel and perpendicular to the diffusion flow, but more in the parallel direction where mass constraint was less. While some grain boundaries behaved similarly in much thicker sheet samples, the converse was generally found, whereby voids were located preferentially at the grain boundaries. They suspected that

this difference between sheets of different thickness was due to inadequate grain boundary area for transporting vacancies in the larger-grained thick samples and/or to larger diffusion distances along the longer grain boundaries in the thick samples. Excess vacancy concentrations were generated by the preferential loss of Zn outward from the sheets. The resulting osmotic pressure created two-dimensional tensile stresses perpendicular to the diffusion flow, the stress component parallel to the flow being free to relax. The stresses perpendicular to the diffusion flow were likewise relaxed by contraction in the 15 μm -thick brass sheets because the interior of the sheets had also lost considerable Zn and contracted in the same manner as the outer surfaces. In the much thicker sheets, however, the loss of Zn was essentially limited to the narrow region along the surfaces, thereby leaving the interior in compression with respect to the surface. The two-dimensional stresses near the surface were thus restrained from relaxing by the interior mass. These stresses cracked open many of the void-ridden boundaries which were parallel to the diffusion flow, and some cases caused grain boundary sliding. Balluffi and Seigle believed that the diffusion-induced stresses were, along with vacancy currents, instrumental in void formation. Accordingly, they calculated that stable voids could be formed when the stresses reached the yield point of the brass and the vacancy supersaturation reached a mere 0.006 (0.6%). They also thought it possible that the dual role of grain boundaries in the thick sheets being either preferential void sites or void-free vacancy sinks could have resulted from stress differences due to elastic anisotropy, or differences in heterogen-

eous void nuclei at various boundaries.

Nearly simultaneous with the above stress-related analysis of porosity by Balluffi and Seigle⁹, Brinkman⁸ performed a similar but more sophisticated analysis of diffusion-induced osmotic stresses in Kirkendall couples to show that the two-dimensional stresses perpendicular to the diffusion flow can reach the yield point of the material when only 1% or more of the diffusion-generated vacancies are eliminated at edge dislocations or other internal sinks. He then calculated that the deformation yielding and fissuring which result from these shrinkage stresses can nucleate and grow stable voids, all without sustaining excess vacancy concentrations.

Internal cracking from diffusion-induced stresses in Kirkendall couples has also been reported to occur in the nonporous regions which are rich in the slower-diffusing element. Reynolds et al.³⁰ found internal ruptures in the Ni-rich (slow diffusion) side of several diffused Au/Ni couples. Ruth³¹ observed grain boundary cracking in the Au-rich (slow diffusion) side of his Ag/Au couples.

Balluffi and Seigle¹⁰ noted similarities in the nature of voids formed during creep and those formed in Kirkendall couples. They believed that internal stresses generated during Kirkendall diffusion were analogous to external creep stresses because either type of stress could promote porosity. They therefore re-examined the growth of voids in Kirkendall couples by combining treatments of void growth during creep with those obtained earlier by themselves^{9,76} and Brinkman⁸. Their calculations showed that a vacancy supersaturation of 0.01 is required to maintain stable pores when diffusion-induced stresses

attain the elastic yield limit in the diffusion zone.

Speculations concerning the nature, origin, and size of pore nuclei have been common to analyses of porosity formation, such as in those works mentioned above. Pore nuclei were suspected to be either impurity particles which were somehow ubiquitous in all Kirkendall couples^{9,10,71,72,76} or else fissures in the matrix created by diffusion-induced internal stresses^{8,11}. Such pore nuclei were generally assumed or calculated to be submicron spheres which grow under a driving force of vacancy supersaturation^{9,71,72,76} or diffusion-induced stresses⁸, or both¹⁰. However, direct observations of such nuclei are lacking and the nature of porosity formation remains largely uncertain.

Doo and Balluffi¹² employed metallography and X-ray diffraction to study diffusion-induced structural changes in dezincified single crystals of brass. Dislocations generated in the diffusion zone by diffusion-induced stresses formed, via climb and glide processes, subgrains a few microns in diameter with misorientations of $\sim 10^\circ$. As diffusion proceeded, recrystallization and grain growth occurred to lower further the strain energy of the matrix. Twins also were formed, along with surface grooves and overall surface roughening. Convincing crystallographic evidence led them to believe that the surface disruptions were due to subgrain boundaries and glide planes intersecting the surface. Bolz²⁸ observed surface ripples on his Au/Pt couples, and tacitly believed them to be glide steps.

Doo and Balluffi¹² also studied dimensional changes of their vapor/solid couples by sintering Mo marker wires into the surface of

the brass and measuring the marker positions before and after diffusion. As was found by others,^{3,6} dimension changes were essentially limited to the diffusion direction. In fact, the observed 0.7% contraction perpendicular to the diffusion flow was only $\sim 1/7$ of the 5% contraction which could have resulted from the lattice parameter change alone. Calculating that contraction from lattice parameter changes would amount to less than $1/6$ of the contraction due to the Kirkendall mass flow, they concluded that stresses induced from lattice parameter changes are small compared to stresses generated by mass flow effects.

Ayres¹³ employed etch pitting and TEM to examine the defect structure introduced during diffusion in bulky Cu/brass couples. He found that high densities of dislocations and subgrains were formed, and calculated that they could have been formed as a result of lattice parameter misfit.

Ruth³¹ found that rippled perturbations developed on the surfaces which bounded the interdiffusion zones in Ag/Au couples. These were in the form of grooves on the Ag-rich (fast diffusing) side, and protrusions of the Au-rich (slow diffusing) side. They had crystallographic shapes, their widths increased according to the laws of bulk diffusion, and no slip lines were found in the rippled regions. Ruth concluded that the surface perturbations resulted from mass flow being accommodated by both pipe diffusion along dislocation cores and by dislocation climb. He proposed that when the dislocations terminate at the surface, they form grooves when operating as vacancy sinks in the Ag-rich side, or protrusions when operating as vacancy sources in

the Au-rich side.*

Another type of surface deformation common to Kirkendall couples is called "bulge and dent" deformation which is formed within the diffusion zone. After considerable diffusion has occurred, a surface bulge appears on the slow-diffusing side and a dent appears on the fast-diffusing side of the couple. The position of the dent corresponds to the porosity zone. Such deformation has been reported for Ag/Au,^{38,77} Ag/Pd,⁷⁷ and Au/Pt²⁸ couples, and has been attributed to mass flow, whereby the dent results from a loss in mass in one side of the couple, and the bulge results from a gain in mass in the opposite side.⁷⁷

It was pointed out above that diffusion-induced stresses in the diffusion zone of Kirkendall-type couples could arise either from lattice parameter gradients due to atomic mismatch,^{6,10-12} or from changes in the number of lattice sites due to the elimination of non-equilibrium vacancy concentrations.^{6,8-10,12} The former case of stresses due to lattice parameter gradients are very prominent in

*Although no mention was made of it, the published figures of surface ripples appear (to this writer) identical for Ruth's³¹ Ag/Au, Bolk's²⁸ Au/Pt, and Doo and Balluffi's¹² dezincified brass. Their proposed dislocation mechanisms differ. To explain the ripples, Ruth described accommodation of mass flow by means of climb and pipe diffusion, whereas Doo and Balluffi attributed their ripples to climb and glide processes. Both explanations appear to be based on sound experimental information (Bolk presented no supporting evidence). Some difference could be expected because stresses due to atomic misfit would be nil in Ag/Au (Ruth) but significant in Au/Pt (Bolk) and Cu/Zn (Doo and Balluffi). However, the three different couples all experienced large amounts of mass flow, and similar surface ripples from this source would be expected in all three couples. Since this similarity was not reported or recognized, it appears that the origin and nature of the surface ripples may not be fully resolved or agreed upon.

semi-conductor devices, where doping (dilute alloying near the surface) often results in a combination of steep concentration gradients and high atomic mismatch between the host matrix (e.g., Si) and certain dopant elements (e.g., P, B).^{*} Queisser¹⁶ used etch patterns to show that stresses due to gradients of B in Si formed dislocations along common slip planes. Schwuttke and Queisser¹⁸ in a similar experiment employed X-ray diffraction to show that dislocations produced in Si by B- or P-doping were edge oriented. Prussin's¹⁷ etch-pit studies of B-doped Si also showed a polygonized dislocation structure. He calculated that the elastic limit of Si is exceeded when certain gradients of B and P are established during diffusion, thereby accounting for the observed formation of dislocations and subsequent slip. In similar experiments, Jaccodine¹⁹ observed dislocation networks in doped Si by using TEM. McDonald, Ehlenberger, and Huffman²¹ diffused various dilute amounts of P into Si which was initially dislocation-free and found that dislocation densities, revealed by etched slip patterns, increased drastically with increasing quantities of P. Czaja,²² employing both calculations and experimental observations of etched slip patterns, showed that the concentration profile of P-doped layers in Si controls both the generation and glide characteristics of the misfit dislocations which accommodate the atomic mismatch between P and the host Si matrix. Levine, Washburn, and Thomas^{23,24} employed TEM to characterize the formation of dislocation arrays and their subsequent motion into Si which results from doping with P or B. They found that the dislocation density was greatest at the depth given by

^{*}The Si-P atomic mismatch is $\sim 6\%$, and $\sim 25\%$ for Si-B; both P and B are undersized and dissolve substitutionally in Si.⁷⁸

the maximum gradient in impurity concentration. The dislocation arrays were found to move into the Si wafer crystals by either glide or climb, or both, depending on wafer orientation. Atomic mismatch defects have also been found in Au-doped Si,^{25,26} where atomic mismatch is also very severe. When atomic mismatch is very small, as in the case of Ga or As doping of Si, increased densities of dislocations were not found in the Si wafers.^{18,20}

With the exception of dezincified brass sheets,⁹ the diffusion experiments cited above employed typical massive couples having dimensions on the order of mm or cm. These massive Kirkendall couples displayed considerable evidence of plastic deformation in the diffusion zone, such as the destruction of twin and grain boundaries, grain boundary sliding, the generation of dislocations and their motion by glide and climb processes, deformation of the surface, grain boundary cracking and fissuring, and possibly to some extent or another, the nucleation and growth of pores. When couple thickness (mass constraint) parallel to the diffusion flow is drastically reduced, another mode of deformation appears, namely, overall bending of the sheet-like couple. The side richest in the faster-diffusing element is bent inwards to form the concave surface.

Couple bending was first reported by Barnes.⁶ He exposed one side of thin Ni sheets, 12- or 240 μm -thick, to a given amount of Cu vapor in order to obtain a gradient in Cu across the sheets. The resultant bending was more severe for the thinner sheet. Lattice parameter changes could only account for about 1/3 of the observed bending, and any bending due to differences in thermal expansion between Cu and Ni would have been in the sense opposite of that observed.

Barnes concluded that the stresses responsible for bending arose from the elimination at internal sinks and sources of nonequilibrium vacancy concentrations which were generated during Kirkendall diffusion. This caused shrinkage stresses on the side of the sheet with excess vacancies and expansion stresses on the opposite, vacancy-deficient side. Decreased bending in the thicker sheet was attributed to its larger mass constraint parallel to the diffusion flow.*

Liu and Powell²⁷ observed bending in thin-sheet couples of Ag/Au (150 μm thick) diffused such that the ends of the couples were partially homogenized. TEM of foils made from the Au-rich, nonporous side of the couple revealed that dislocations and subboundaries were created in order to relieve the chemical forces from nonequilibrium vacancy concentrations generated during diffusion. They pointed out that dislocation climb parallel to the diffusion flow could contribute to couple bending, and that such climb would relieve nonequilibrium vacancy concentrations without contributing to marker shifting.

When Queisser¹⁶ diffused B into one face of a 50 μm -thick Si sheet, the sheet bent because of high atomic mismatch strains intro-

*It is interesting to compare bending of Barnes¹⁶ Cu/Ni couples with cracking in Balluffi and Seigle's⁹ dezincified brass sheets, both being solid/vapor couples. Grain boundary cracks extended inward from both faces of the brass sheets because both of these near-surface portions were placed under severe tensile stresses by dezincification. The Cu/Ni couples bent rather than cracked because diffusion inward from the single solid/vapor surface had placed that side under compression and the opposite side under tension. In either case, the deformation stresses causing bending or cracking originated principally from the elimination of nonequilibrium vacancy profiles which were generated during Kirkendall diffusion.

duced across the sheet.*

Plastic deformation effects from atomic misfit strains have also been observed by TEM in ultrathin binary couples, $\sim 2,000\text{\AA}$ thick. Such couples have been made by vapor depositing a thin, epitaxial, single crystal layer of metal onto a similar layer of its binary counterpart, then diffusing.^{14,15} In such a study of the Au/Pd system, Matthews and Crawford¹⁴ observed that high mismatch strains at the interface were accommodated either by forming mismatch dislocations or by locally bending portions of the couple to form protruding, cap-shaped grains which were free of dislocations. As the misfit strains decreased with increasing interdiffusion, the dislocations rearranged into subboundaries, then grain boundaries, by climb and glide processes, and the cap-shaped grains became less curved. Matthews and Jesser¹⁵ subsequently repeated the above experiment for a series of six, single phase, Kirkendall systems having atomic misfits which decrease in the order Cu-Au, Pd-Ni, Pd-Au, Cu-Ni, Pt-Pd, and Au-Ag. They found that the fraction of film occupied by curved grains decreased as misfit decreased, the Cu-Au films being completely occupied by curved grains and Au-Ag having none. This demonstrated that internal strains decrease markedly with decreasing atomic mismatch.

*Observations of couple bending have not been restricted to the relatively simple cases of single phase, binary systems. Metal strips oxidized on one surface bend severely because of stresses related to oxygen gradients, volume changes from phase transformations within the strip, oxide layer formation, and thermal expansion differences between the newly-formed phases^{79,80}. However, these cases are too complex to be of direct interest here.

The very minor Ag-Au atomic mismatch which was demonstrated above¹⁵ is compared with other Kirkendall systems in Table 1 (see Introduction). Note that the Ag-Au mismatch remains very small at 720°C, which is a useful high temperature diffusion treatment for the Ag-Au system.^{81,82}

EXPERIMENTAL PROCEDURE

Very thin polycrystalline sheets of pure Ag and pure Au were pressure-welded to form thin-sheet couples. The thickness parallel to the diffusion direction of most of these couples was either 88 or 335 μm ; a few were 132, 163, or 170 μm thick. Some of the couples contained inert markers at the original join. Isothermal diffusion anneals were performed for various times at 750 $^{\circ}$, 800 $^{\circ}$, or 850 $^{\circ}$ C, most often at 750 $^{\circ}$ C. During diffusion, some of the couples were mechanically constrained to prevent bending by graphite pistons held firmly against the broad faces of the couples. After diffusion annealing, the couples were examined to determine the concentration profile, microstructure, and the amount of marker movement and bending. The following subsections describe the equipment and methods used to accomplish the foregoing. Because the same inert atmosphere furnace was used for couple fabrication and diffusion annealing, its description is given first.

Furnace Description

A purified argon atmosphere was selected in order to avoid complications arising from (dissolved) oxygen interactions with vacancies in either Ag⁸³ or Au⁸⁴, especially since Ag dissolves 0.03 at.% oxygen³⁶ at the diffusion temperature of 750 $^{\circ}$ C. Clarebrough et al.,⁸⁵ in controlled-atmosphere quench and anneal experiments with Ag, attributed unusually rapid decreases in electrical resistivity to vacancy-oxygen interactions when heating was done in wet argon or air.

They also observed considerable precipitation, particularly on dislocations in an air-heated sample. Liu and Powell²⁷ found large dislocation loops associated with small particles, possibly Ag_2O , in Ag/Au couples diffused at 880°C . On the basis of a thermodynamic calculation, they indicated that their commercially-pure argon atmosphere could have furnished sufficient oxygen to account for the observed precipitation.

The sample furnace and the argon gas purifying train are shown in Fig. 2. The gas train and sample furnaces were each 30 in. long with a 2.5 in. bore diameter and were resistance heated by helically-wound Kanthal A-1^{TM*} wire. Each contained a 2 in. internal diameter stainless steel furnace tube (type 304, schedule 40) cooled at its extremities by circumferential water jackets. The gas train tube was densely packed with pure cooper wool and was maintained at 700°C . Commercially-pure (99.995%) argon, dynamically stabilized at about 0.5 psig throughout the system, was passed through a drying column of CaCl_2 desiccant, then through a hot copper furnace where residual oxygen and moisture were further reduced.⁸⁶ The gas was maintained at near-equilibrium with the hot copper by limiting the gas flow rate to about 10^{-3} cu. in. per sec. The copper wool was periodically changed when that half of the hot zone copper nearest the incoming argon appeared to be slightly oxidized. The purified argon was protected within an all-metal gas transfer system (valves, tubing, connections, etc.), with either neoprene O-rings or TeflonTM seals at appropriate assembly points. Each (furnace) tube end assembly was externally threaded onto

*TM is an acronym for Trade Mark

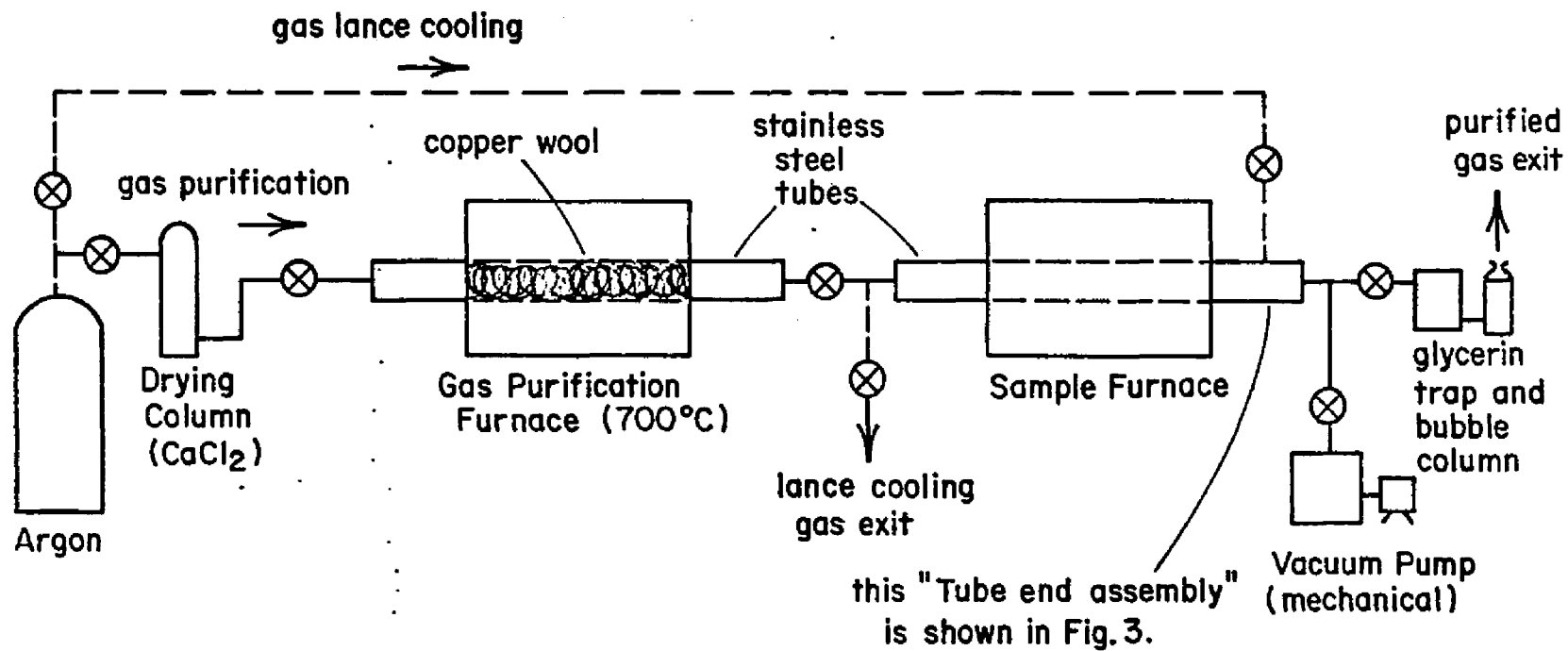


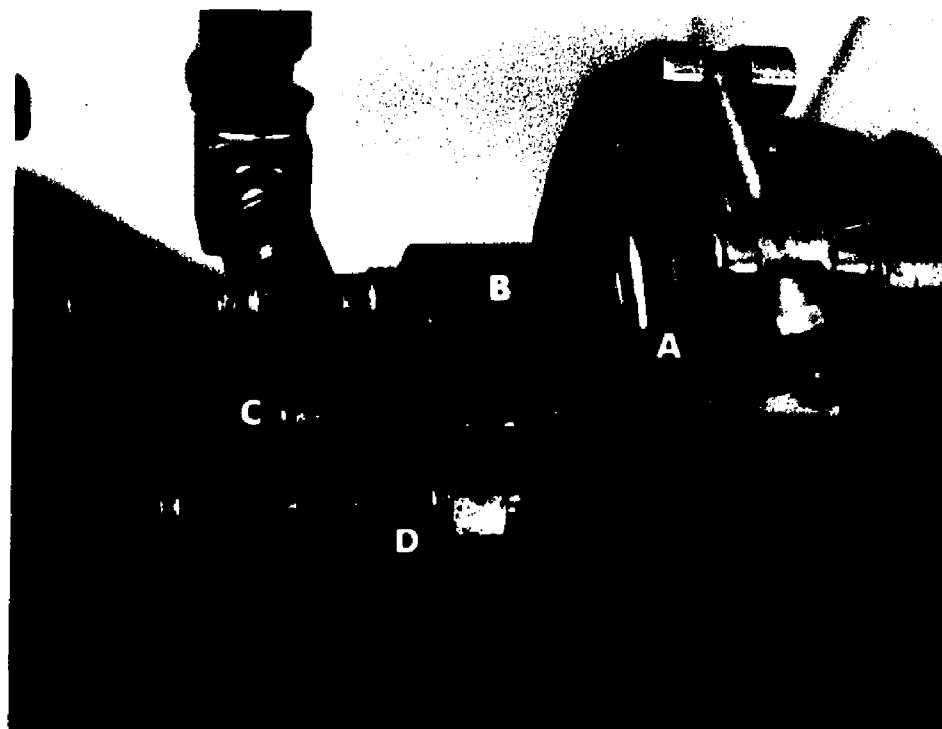
Fig. 2. Schematic of sample furnace and gas train.

the tube and sealed at the butt end of the tube with an O-ring. The end assembly that served as an access port for the sample furnace had an O-ring sealed end cap that conveniently detached. This end cap also featured a sample positioning rod, a gas port, and a sample monitoring thermocouple (Fig. 3).

In practice, the loaded sample holder was positioned at the cold end of the tube, the end cap sealed, and the tube repeatedly (5 or more times) evacuated and backfilled with argon in order to remove ambient air. Next, a dynamic atmosphere of purified argon was established and the furnace brought to equilibrium temperature. Then the sample was rapidly transferred to the hot zone by means of the (sliding) sample positioning rod which was attached to the sample holder. This rod slipped through its SwagelokTM fitting without disrupting seal integrity.* Thus, sample positioning within the furnace did not noticeably contaminate the inert atmosphere.** By withdrawing the sample holder from the hot zone to the water cooled end of the tube, a cooling rate comparable to air cooling was obtained. Much more rapid cooling was obtained by lancing a 50 psig stream of argon directly onto the sample holder via the gas port in Fig. 3; the argon was simultaneously vented at the opposite end of the furnace tube.

*Both the sample positioning rod and monitoring thermocouple sheath rod were sealed by a TeflonTM ferrule and ring combination that was compressed and swaged around the rod to affect a seal. The thermocouple wires were also sealed with a SwagelokTM fitting by replacing the ferrule and ring with a TeflonTM sphere containing two holes drilled specifically to accept the wires.

**When not in use, the system was left sealed under vacuum (about 80 μm Hg, using a mechanical vacuum pump). This minimized ambient contamination and served as a continuing monitor for leakage.



- A. vee-flanged end cap
- B. gas port
- C. sample positioning rod; exploded view of SwagelokTM fitting with TeflonTM seals
- d. sample monitoring thermocouple

Fig. 3. Furnace tube end assembly.

Temperature control was maintained by a "Leeds & Northrup"TM on-off controller with its chromel-alumel control thermocouple placed between the furnace winding and furnace tube at the center of the hot zone. To minimize temperature fluctuations, a variable autotransformer in the power line was adjusted at each temperature setting to give equal on-off times during power cycling. The sample furnace taps were shunted to give a symmetrical, 2 cm-long hot zone of $750 \pm 0.5^{\circ}\text{C}$ (and a 4 cm length of $\pm 1^{\circ}\text{C}$). The chromel-alumel thermocouples used for sample monitoring were calibrated and guaranteed accurate to 0.5°C (at 750°C) by the vendor. During furnace calibration, the monitoring thermocouple was placed at the sample position inside the sample holder. During actual sample heat treatment, it was necessary to place this thermocouple between the outer surface of the sample holder and the inner wall of the furnace tube. In so doing, the thermocouple was kept immediately adjacent to the sample itself. The couple output was determined on a research potentiometer sensitive to 0.1°C . Considering the above factors, the diffusion anneal temperatures are reliable to within $\pm 1^{\circ}\text{C}$.

Complete thermal histories were recorded during all welds and diffusion anneals. Interdiffusion which occurred during the nonisothermal heating and cooling cycles was calculated from the resultant time-temperature data.⁸⁷

Sheet (couple half) Fabrication

The starting materials were 99.999 wt. % Au or Ag wire, 1 mm in diameter.* In order to obtain sufficiently large sheets of each

*Purchased from Leytess Metal and Chemical Corp., 500 Fifth Ave., New York, N. Y. 10036.

material, the wires were melted in spectrographically-pure graphite crucibles into cylindrical ingots about 18 mm in diameter by 15 mm long. Furnace cooling the ingots yielded an average grain size of 8 mm. Any surface contaminants, such as entrapped flecks of graphite, were removed by electropolishing a 50 μm layer from each ingot. The ingots then were cross cold-rolled to minimize sheet texturing.* After the ingots were reduced to 5 mm-thick slabs, they were given a recrystallization anneal by heating to 800°C, then furnace cooling. Subsequent cold reduction yielded sheets 25 mm wide with thickness from 44 to 168 μm . Within any given sheet, no thickness gradients were detectable by micrometer measurements and cross section metallography. Disks 15 mm in diameter were razor cut from the center of the sheets and the cut edges were hand-dressed. Although the rolling mill was scrupulously cleaned prior to rolling, the disks were hand-polished with 1 μm Cr_2O_3 slurry to assure clean surfaces. The disks then were given a full recrystallization anneal of 20 min. at 800°C, followed by furnace cooling. The annealed disks were bright and flat. The average grain size was equivalent to the sheet thickness, with many of the larger grains extending across the entire sheet thickness. Final surface cleaning of the annealed disks was done with a hand-held cotton swab containing a dilute slurry of 0.5 μm Cr_2O_3 particles.** The disks were retained on an optically-flat glass plate during polishing,

*In cross rolling, the rolling direction is alternated 90° between successive reduction passes.

**Some of the earlier disks were electropolished in 5 or 10% KCN, but this practice was discontinued because of preferential polishing of some of the grains (chemical anisotropy effect).

and extremely little pressure was applied in order to minimize surface deformation.

Marker Application

A suitable marker material, levigated iron oxide (Fe_2O_3),* was prepared by levigating an aqueous slurry of jeweler's rouge 5 times, each time decanting the finer-particled suspension from the mixture and discarding it. The final slurry of the heavier particles was diluted in a solution of one (1) drop of "Kodak" Photo-FloTM (a wetting agent) in twenty (20) ml of distilled water. The resulting particles are shown in Fig. 4. The marker slurry was applied by eye dropper onto the welding surface of a couple half to obtain a uniform particle distribution with an average particle (or particle agglomerate) marker size of a few μm and an average interparticle spacing of 150 μm .

Welding

Pairs of Ag and Au disks were pressure-welded to form thin-sheet couples, as depicted in Fig. 5. Welding was done in the pressure welding device shown in Fig. 6. All of the device components were machined from high-purity graphite, except for the hollow stainless steel expansion plug, B.** Graphite was used because of its low

*Several other types of inert markers were tried throughout the experiment, but these proved unsuccessful in one or more respects. These included 8 μm tungsten wire, 1 μm Cr_2O_3 particles, and 5 μm SiC particles. Since the successful iron oxide marker method was developed late in the research, the earlier couples did not yield marker information.

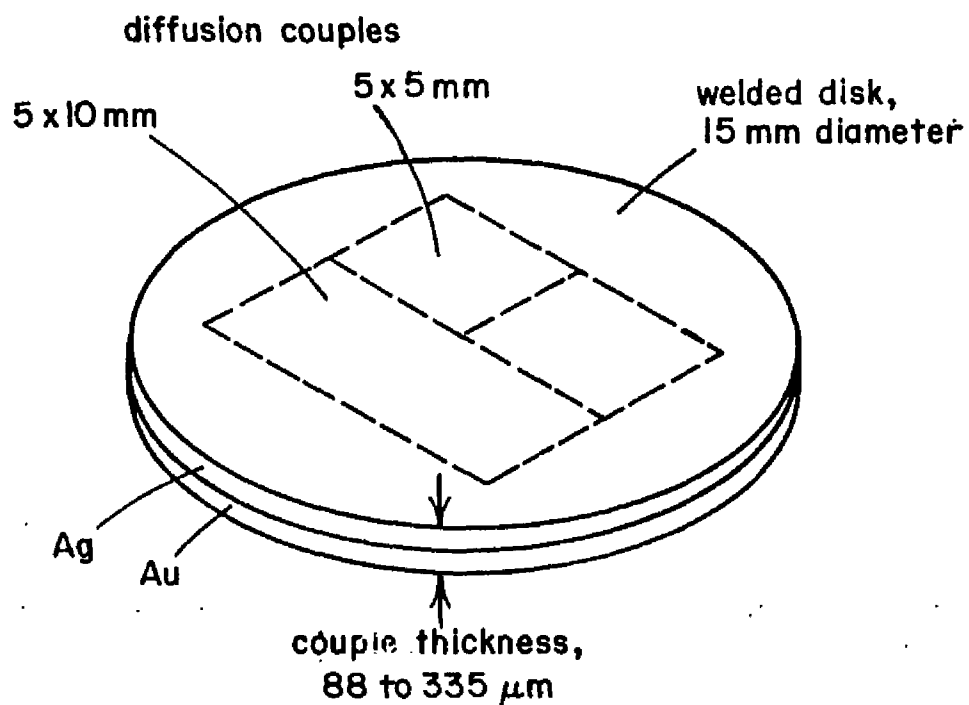
**Because the coefficient of thermal expansion of stainless steel ($11.2 \times 10^{-6}/^\circ\text{F}$)⁸⁸ is about 12 times greater than that of graphite ($0.9 \times 10^{-6}/^\circ\text{F}$)⁸⁹, the steel plug exerts pressure on the couple when the device is heated during welding, thereby contributing to good weld plane contact.



420X

Most particles are a few μm in diameter. Particle density shown here is greater than that employed in couples, the couples having interparticle spacings of $\sim 150 \mu\text{m}$.

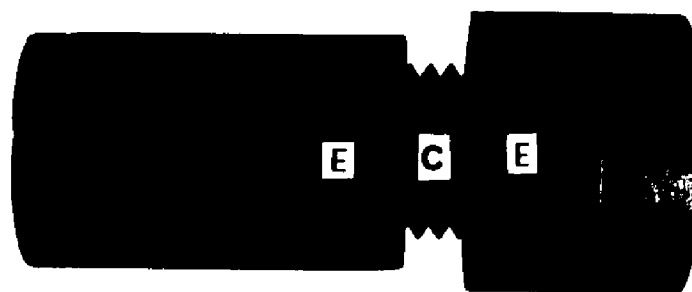
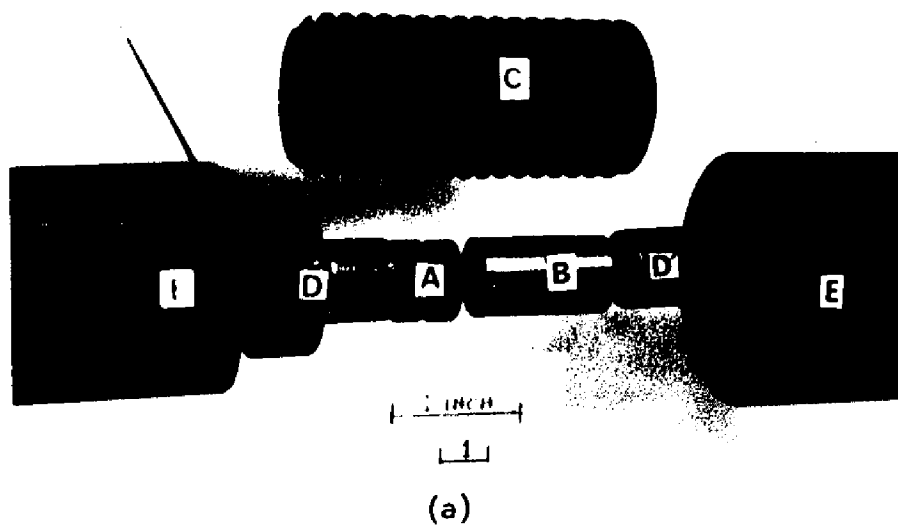
Fig. 4. Levigated iron oxide markers.



Couple thickness is exaggerated here for illustrative purposes.

Diffusion couples (dotted lines) were obtained from the center-most portion of the welded disk.

Fig. 5. Schematic of a thin-sheet Ag/Au couple.



(a) Disassembled. Couple halves to be welded are placed between short pistons, A. All pistons (A,B,D,D') are subsequently loaded into bored cylinder, C.

(b) Assembled. End caps, E, are threaded onto cylinder, C. All components are graphite, except for the stainless steel expansion plug, B.

Fig. 6. Pressure welding device.

thermal inertia and inertness relative to Ag and Au. Referring to Fig. 6(a), a disk of Ag and one of Au were sandwiched between the short pistons (A) and inserted, along with the other pistons (B,D,D'), into the smooth-bore cylinder (C),* whereupon the end pistons (D,D') protruded partially from the cylinder. The end caps (E) were then threaded onto the cylinder and tightened to maintain 30 psi compression on the broad faces of the semicouples.** The assembled welding device is shown in Fig. 6(b).*** The longitudinal center-bore in the device accepted the monitoring thermocouple.

Interdiffusion during welding (weld depth) was initially limited to $2\ \mu\text{m}$ so that a substantial portion of nondiffused material would be available for subsequent diffusion annealing of the $88\ \mu\text{m}$ -thick couples. During subsequent diffusion annealing, many of the couples began cracking open, often along the welding interface. Of course, cracking automatically disqualified a couple from further analysis or consideration. Cracking was initially suspected to be the result of poor welding, especially since similar weld failures have been reported^{3,56,57} for pressure-welded bulk couples having weld depths 1 or 2 orders of magnitude larger than the $2\ \mu\text{m}$ -deep welds initially em-

*In order to assure intimate face matching and subsequent good welding, ultra-parallel faces were required on the short pistons (A) which bounded the semicouples. Accordingly, these pistons were lapped to a thickness deviation of less than $\pm 1.25\ \mu\text{m}$.

**Compression was established by placing a drift pin through the bored-out end cap (E) and onto the piston (D), then loading the pin to 10 pounds. After securing the end caps, the load and drift pin were removed.

***Small vent holes (not visible in Fig. 6) were drilled throughout the weld device to permit unrestricted outgassing of the device when in the furnace.

ployed here. Weld depths were therefore increased to 4 and 6 μm , and weld plane integrity was ascertained via examination and testing. Only after these efforts assured the integrity of welding interfaces could the couple cracking be unambiguously associated with the subsequent diffusion anneal process (this cracking phenomenon will be reported later). From subsequent trial and error experiments, it was found that couples no longer cracked during 750°C diffusion when 4 or 6 μm -deep welds were employed. The 4 μm welds were limited to 88 μm -thick couples which were scheduled for the shorter diffusion anneals; otherwise, 6 μm welds were employed. An exception to this was the 30 μm -deep welds obtained specifically for a set of 163 μm -thick couples scheduled for 850°C diffusion. The various weld depths were obtained by altering the heating, cooling or soak cycles during welding.* The methods of measuring, inspecting, and bond-testing the welds are given next.

Weld depths were measured graphically from the weld's concentration-penetration** curve by constructing a tangent slope at the composition center ($N_{\text{Ag}} = 0.5$) and using its intersections with the couple

*Penetration

Depth	Welding Method
2 μm	Rapid heating ^a to 700°C + maximum argon lance cooling ^b
4 μm	Rapid heating to 700°C + moderate argon lance cooling ^c
4 μm	Rapid heating to 725°C + maximum argon lance cooling
6 μm	Soaking for 0.5 hr at 600°C + air cooling
30 μm	Heating to 770°C in 770°C furnace + air cooling

a "rapid heating" ($\sim 200^\circ\text{C}/\text{min}$) was obtained by plunging the weld device into a 1000°C hot zone, then immediately withdrawing after reaching the desired temperature of 700 or 725°C.

b "maximum argon lance cooling" rate was $\sim 125^\circ\text{C}/\text{min}$ from 700° to 400°C.

c "moderate argon lance cooling" rate was \sim twice as rapid as air cooling.

**obtained with the electron microprobe, as described in the "Chemical Analysis" section.

distance axis to define the penetration depth. This operation is depicted in Figs. 7 and 8 for the 2 μm and 6 μm -deep welds, respectively.* (In these and the following concentration-penetration curves, the couple distance of zero denotes the x-axis position where N_{Ag} becomes unity.) Ignoring the apparent interdiffusion which lies outside of the graphically-determined penetration zones in Figs. 7 and 8 serves to compensate somewhat for the electron beam diameter of $\sim 3 \mu\text{m}$. Without such compensation, a nondiffused butt joint would appear to have an interdiffusion zone roughly the size of the electron beam. Although the graphical method for determining weld depth becomes less valid as interdiffusion increases, it is suitable for the steep-gradient, small-interdiffusion welds employed here. As a check, weld penetrations were alternately determined by calculating the diffusion contribution from the nonisothermal (heating and cooling) weld cycles. Using the approximation

$$x \sim (\pi D t_{\text{eff}})^{\frac{1}{2}}$$

, where $2x$ = calculated depth of interdiffusion

D = chemical diffusion coefficient at 750°C (1.54×10^{-10}

$$\frac{\text{cm}^2}{\text{sec}})$$

t_{eff} = effective time at 750 C, calculated from heating and cooling time-temperature data

, the calculated weld depths were within 25% of those determined graph-

*The electron microprobe data for Fig. 7 was obtained from a sample whose cross section was inclined in the mount to give a 2X mount magnification. Otherwise, the microprobe's $\sim 3 \mu\text{m}$ electron beam would not yield the spatial resolution indicated in the figure.

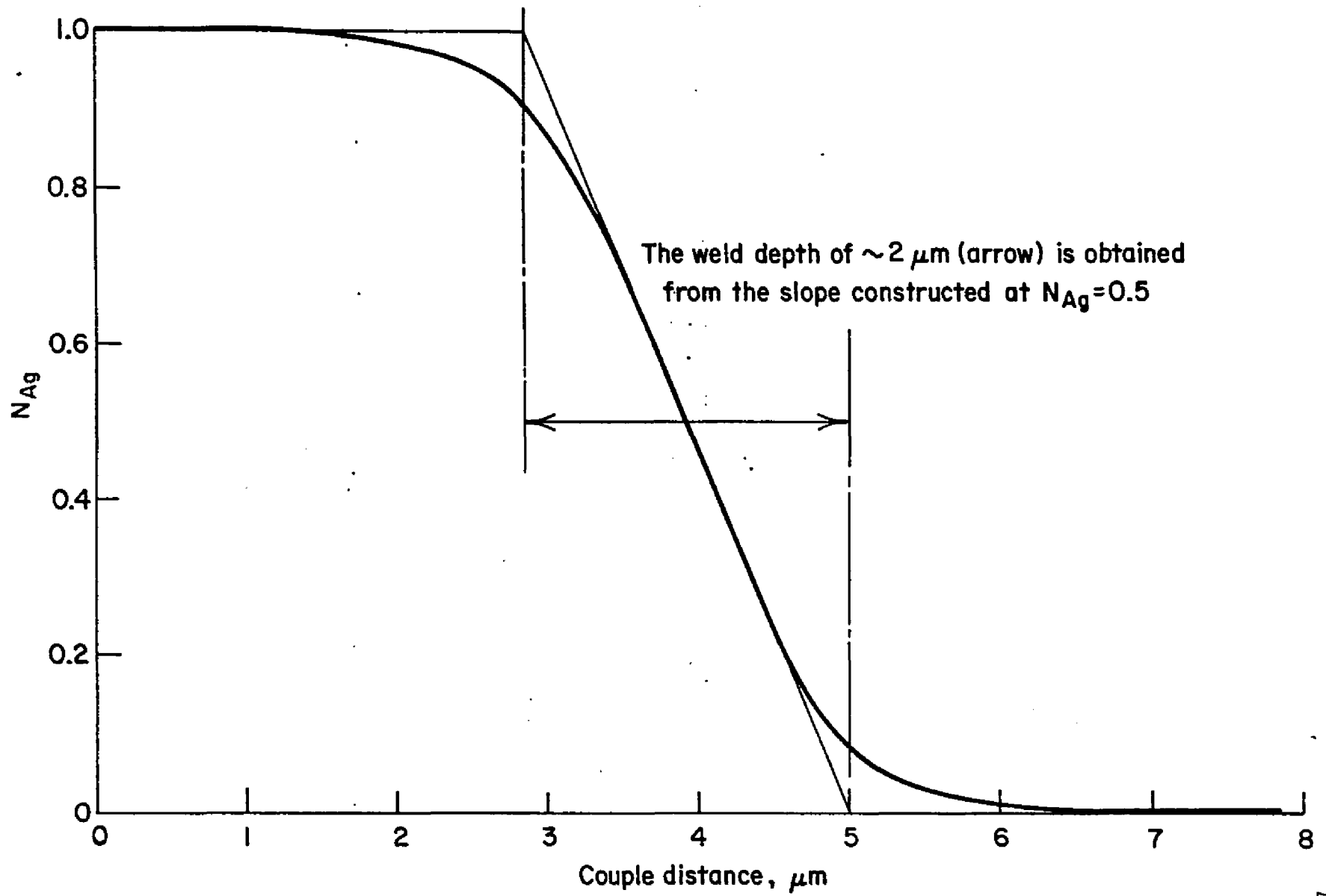


Fig. 7. Concentration - penetration curve for a $2 \mu\text{m}$ -deep weld.

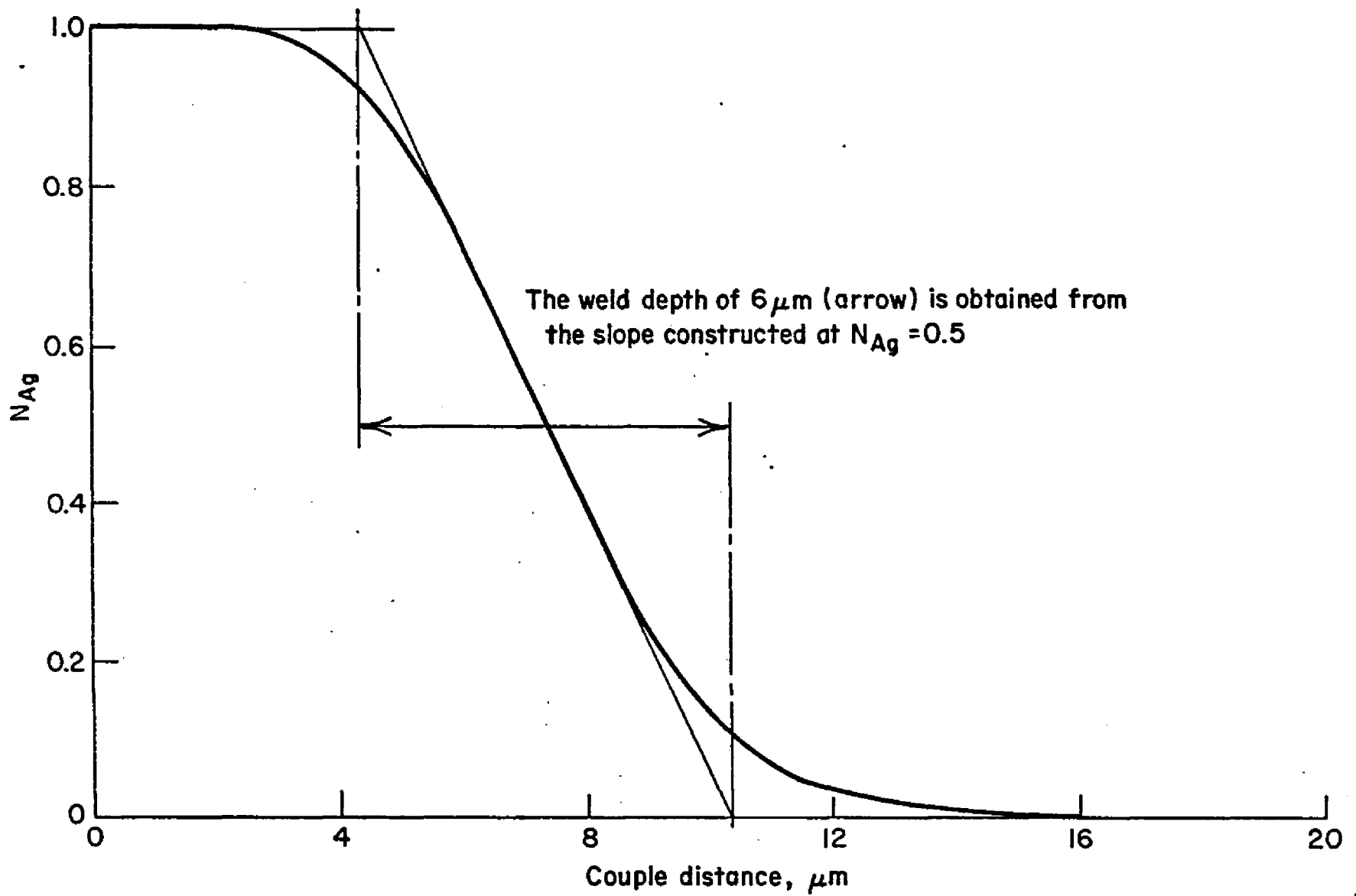


Fig. 8. Concentration- penetration curve for a $6 \mu\text{m}$ - deep weld.

ically. This is reasonable agreement between the two methods. For consistency, the graphical method was selected to describe weld depths.

Weld plane integrity of every welded disk was ascertained routinely by metallographic examination, electron microprobe analysis, and destructive testing of chord segments taken from each welded disk (chord segments are seen in Fig. 5). When mildly-etched metallographic cross sections were examined, any interface cracks were clearly delineated. During microprobe analysis, abrupt increases in the slope of the concentration-penetration profile occurred at these same faulty interface regions. The destructive tests involved a simple tearing apart of the welded sample along its weld plane.* Weld integrity was indicated by resistance to tearing offered by the couple and by visual evidence of Au-Ag adhesion on the tear-exposed surfaces. Completely bonded weld joints were characterized by a thin, adherent covering of ultrafine Ag flecks over the entire Au surface. Any localized region of spotty or sparse Ag flecking on the Au surface was evidence of poor bonding. Early in the experiments, several entire disks were destructively tested. After sound welding became routine, the destructive tests were limited to the chord segments of the welded disks.

Another indication of weld plane integrity resulted during subsequent diffusion. Wherever appreciable diffusion took place within a couple, overall microroughening appeared on the broad, terminal surfaces of the thin-sheet couples. If, however, a weld joint suffered

*This was usually done by splitting the outer edge of the weld plane with a razor blade, grasping these split segments with tweezers, then pulling (tearing) the sandwiched couple apart.

a localized discontinuity, the lack of diffusion across the discontinuity yielded a conspicuously-smooth spot on an otherwise-microroughened couple surface.

In a separate experiment, weld plane integrity was tested by plastically deforming as-welded couples before diffusion, believing that regions of poor bonding would likely fail during couple deformation and would, therefore, be quite obvious (exaggerated) in post-diffusion analysis. To this end, three 88 μm -thick couples in the form of 5 x 10 mm strips were identically fabricated and given 4 μm -deep welds. Two of these were permanently bent around glass rod mandrels of different radii. One couple was bent to an arc of 11 mm radius, the other to 4 mm.* The third couple was not bent in order to serve as a control sample. The three couples were diffused to about their semi-infinite limit (2.37 hr at 750°C), then examined. All three couples exhibited identical diffusion penetrations and metallographically-sound interfaces, evidence that the welding interfaces were well-bonded and continuous.

Diffusion Annealing

A few of the earlier 15 mm-diameter disk couples were diffused in their entirety. The centermost portions of all other welded disks were sectioned into couples 5 x 5 mm or 5 x 10 mm, as indicated in Fig. 5. Cutting was done carefully with new, 77 μm -thick jeweler's saw blades, with the broad face of the disk supported on a flat LuciteTM plastic block. The blade was maintained parallel to the face

*The bending was easily done by hand. In order to make the couples conform permanently to the mandrel surface, it was necessary to strain harden the couples by pressing them repeatedly (cold working) around the mandrel.

of the couple to avoid edge ripping. After sectioning, the cut edges were lightly hand dressed with 600 grit SiC paper.

Those couples monitored for bending behavior were physically unconstrained in a graphite holder during diffusion annealing. Other couples were mechanically constrained from bending by performing the diffusion annealing in the welding device. Mechanical constraint was applied by graphite pistons (A, in Fig. 6) held firmly against the broad faces of the couple by a 1.3 cm length of steel expansion plug (the expansion plug used during welding was twice this length).

The couples were diffused at 750^o, 800^o, or 850^o, mostly at 750^oC,* for times varying from about one-half to several hr. None of the diffusion anneals were interrupted.** Most of the diffused couples were semi-infinite, i.e., the terminal ends of the couple were still pure Ag or pure Au after completion of the diffusion anneal. Others were partially homogenized. Many of the couples were diffused in a systematic manner, e.g., (1) a series of 88 μ m-thick couples was diffused at 750^oC for various (increasing) times, and (2) identical diffusion anneals were given to couples of varying thickness.

*750^o was selected for most of the couples in order to avoid serious diffusion time errors inherent in the shorter times dictated by higher diffusion temperatures. Even at 750^oC, homogenization began shortly after \sim 2 hr in the thinnest (88 μ m) couples. Increasing the diffusion time by lowering the temperature below 750^oC is inadvisable because of the significant grain boundary diffusion of Ag below 700^oC. 81,82,90,91

**All diffusion anneals were terminated with maximum argon lance cooling. In order to minimize nonisothermal contributions to diffusion during heating and cooling, the unconstrained coupled diffused for very short times (\sim 30-45 min) were contained in a small (40 g.) graphite boat instead of in the larger, 160 g. welding device.

Bulky Diffusion Couples

In addition to the above thin-sheet couples, three bulky couples were similarly fabricated.* diffused, and examined for comparison with the thin-sheet couples. The size of these couples, 2 mm in diameter by 8 mm in the diffusion direction, is typical of most bulky couples. Although markers were incorporated in these bulky couples, marker measurements were found to be meaningless because of inaccurate reference points and will not, therefore, be reported.

Sample Analyses

Thickness and bending measurements:

A vernier micrometer, accurate to $\pm 1.25 \mu\text{m}$ and equipped with anvil ball tips, were employed for thickness and bending measurements. Couple thickness was monitored before and after diffusion annealing. Couple bending was calculated from data obtained by placing the bent couple on a flat glass slide such that the couple was concave downward, (dome-like), then measuring the bending height.

Cross section metallography:

Cross section metallography surfaces, parallel to the diffusion direction, were prepared in order to examine the microstructure, porosity, and markers, and to serve as electron microprobe samples. Metallographic samples included annealed sheets prior to welding,

*These bulky couples were fabricated by Richard Helferich as part of his undergraduate experimental investigation requirement in the Dept. of Metallurgical Engineering, The Ohio State University. The 2 mm diameter by 4 mm long cylindrical couple halves were cast from the melt into graphite cylinders. The welding surface of each couple half was ground and polished flat, the couple halves annealed, then very lightly repolished, then pressure-welded to depth of $24 \mu\text{m}$.

as-welded couples, and diffusion-annealed couples. The "as-weld" samples were those remnant chord segments of the welded disks that were generated when diffusion couples were sectioned from the disks, as depicted in Fig. 5. All metallographic samples were plated with about 1-3 mil of electrolytic nickel in order to preserve the outer edge features of the cross section. Nickel was selected because its X-radiation does not interfere with Ag or Au X-radiation in the electron microprobe analysis. The plated samples were mounted edgewise in BakeliteTM and wet ground with 220-grit SiC paper to a depth greater than twice the couple thickness. The resultant cross section thus was representative of bulk, and not surface, diffusion. Continuously finer grinding through 4/0-grit SiC paper was followed by 0.25 μm diamond polishing on a silk cloth. Although the "silk cloth + diamond" polish yielded the very flat, smear-free surface required for electron microprobe analysis, it was necessary to final polish briefly with 0.3 μm α -Al₂O₃ (Linde ATM) in order to lower the scratch density. Disturbed metal then was removed by a mild (2 sec.) etch in 2% KCN, followed by a very light "Linde A" repolish.

Chemical or electrolytic etching of the couples was complicated by the very marked passivity of the Au-rich material with respect to the Ag-rich material, thereby necessitating a compromise, two stage etching procedure. This involved a 2% KCN etch to reveal the Ag-rich structure, and a subsequent etch in 1 part 10% KCN: 1 part 5% ammonium persulfate to reveal the Au-rich structure. The latter etch, depending on etching time, would either over-etch or dissolve the previously-examined Ag-rich material.

Metallography was done on a Bausch and Lomb metallograph, where marker positions were measured with a reticle grating at 800X or more. Although marker positions were measured with respect to both Ag and Au terminal ends, reported marker shifts were determined only from those measurements made from the Au end. As previously reported,^{92,93} this circumvents the error associated with couple swelling which occurs when porosity forms in the Ag-rich region.* Also, surface irregularities which developed during diffusion were observed to be more predominant along the Ag terminus, making measurements there less reliable than those obtained from the Au terminus. Marker identity during microscopic measurements was quite unambiguous. They were usually identified by their red color, and their plane of focus was usually higher than the small pores which often resembled markers. Also, the electron microprobe, set for a third order iron $K\alpha$ line of $\lambda = 5.81\text{\AA}$, was used to ascertain the identity of markers. This proved especially useful when SiC grinding particles occasionally became entrapped in the porous region adjacent to the real markers and were sometimes difficult to visually distinguish from the markers.

Because the thin-sheet couples were bent by diffusion or tilted slightly in the mount, the metallographic surfaces were often not perpendicular to the weld interface, thereby magnifying the cross section thickness of the couple. To correct for this "mount magnification", all distances measured on the metallographic surface, e.g.,

*Conversely, marker displacements can be measured to purposely include dimensional changes caused by porosity swelling^{6,53,54,83}. This was not done here.

marker positions, were multiplied by the ratio

$$\frac{\text{true couple thickness (measured by micrometers)}}{\text{apparent couple thickness (measured from the metallographic cross section)}}$$

Chemical Analysis:

An ARL EMX model 21,000 electron microprobe X-ray analyzer was used to determine chemical compositions on metallographic cross sections. The profile method of analysis was used, where the X-ray intensity was recorded continuously along a line perpendicular to the weld interface. In some cases, profiles also were made parallel to the weld interface in order to ascertain the absence of concentration gradients which might exist from grain boundary diffusion, internal fracturing of the couple, etc. Prior to microprobe analysis, the polished samples were given an extremely light etch (1 sec. in 2% KCN) so that regions of interest in the couple could be identified in the microprobe. *

Usually, Ag ($\lambda = 4.154 \text{ \AA}$) was continuously recorded during profiling, but either Au (alone) or Ag and Au duplex stepping analysis was used on a few occasions. A 25 kV electron beam with a diameter of $\sim 3 \mu\text{m}$ was employed. Recorded profiling was usually done at a

*This very mild etching was done to reveal better the following interfaces: Ag:Ag (weld), couple matrix: marker, Ag:Ni, and Au:Ni. The etch was quite insufficient to reveal the crystalline microstructure of the Ag-rich material. Conventional etching to reveal crystalline microstructure was detained until the microprobe analysis was complete because (1) such etching disrupts the planarity of the surface, thereby altering microprobe results⁹⁴, and (2) the possibility exists for Au to chemically replace Ag, thereby altering the chemical composition of the surface.^{39,95}

sample velocity of 2 or 8 μm per min., while 96 μm per min. traverses were often used for sample area selection purposes. Chart speed was generally 1.5 in. per min. Length corrections were made for profile lines which were not exactly perpendicular to the weld interface in a manner analogous to the above "mount magnification" correction.*

The methods of electron microprobe analysis and data conversion were largely adopted from Ziebold and Ogilvie.⁴⁶ In order to obtain the empirical constant required for conversion of X-ray intensity to chemical composition, a series of Ag-Au alloy standards was made by melting well-mixed blends of pure Ag and pure Au powders (-100 mesh) into button ingots, then homogenizing for 5 days at 900°C. Each of the four ingots, nominally 20, 40, 60, and 80 wt.% Au, plus button ingots of pure Ag and pure Au, were divided in two. One set of the alloy samples was electrochemically cleaned, then (wet chemistry) analyzed by gravimetric determination of AgCl precipitation. The duplicate set was mounted and polished metallographically to serve as microprobe standards. X-ray intensity data from these standards was related accordingly to the atom fraction values established by wet chemistry.⁴⁶ The resulting expression relating intensity and atom fraction was used thereafter (via computer) to convert all microprobe profile data into concentration-penetration curves. As-welded couples were always included in the metallography mounts so that their pure Ag or pure Au portions could serve as peak and off-peak background standards. Peak intensities on the pure metal standards

*Fortunately, profile lengths could be measured from the "ghost trails" left on the sample surface by electron beam contamination.

were recorded immediately before and after each profiling operation in order to monitor specimen current stability. Whenever shifts in the specimen current during profiling detectably altered the peak intensities from these pure standards, that particular profile was considered quantitatively invalid and was, therefore, usually re-determined. Such profile repeating was commonplace, with an average of four profiles made for every valid one obtained.

The resulting concentration-penetration data were analyzed with the well-known Boltzman-Matano relationship^{51,52} in order to obtain the chemical diffusion coefficient, D , where

$$D = -\frac{1}{2t} \frac{1}{dN/dx} \int_{N_0}^N x \cdot dN \quad \dots 4$$

with t = diffusion time, dN/dx = slope of the concentration-penetration curve at the composition, N . The value of the integral equals the area under the concentration-penetration curve bounded by N and the terminal composition, N_0 . Computer solutions of the Boltzman-Mantano analysis were obtained on an XDS (Xerox Data Systems) Sigma 7 computer. The program used was a language-modified Fortran IV program which was originally devised by Hartley and Hubbard.⁹⁶

Transmission electron microscopy (TEM*):

Thin foils were made from some of the couples and examined by TEM in order to observe the defect structure generated during diffusion. The plane of each foil was essentially perpendicular to the

*TEM is a common acronym for transmission electron microscop(y,e)

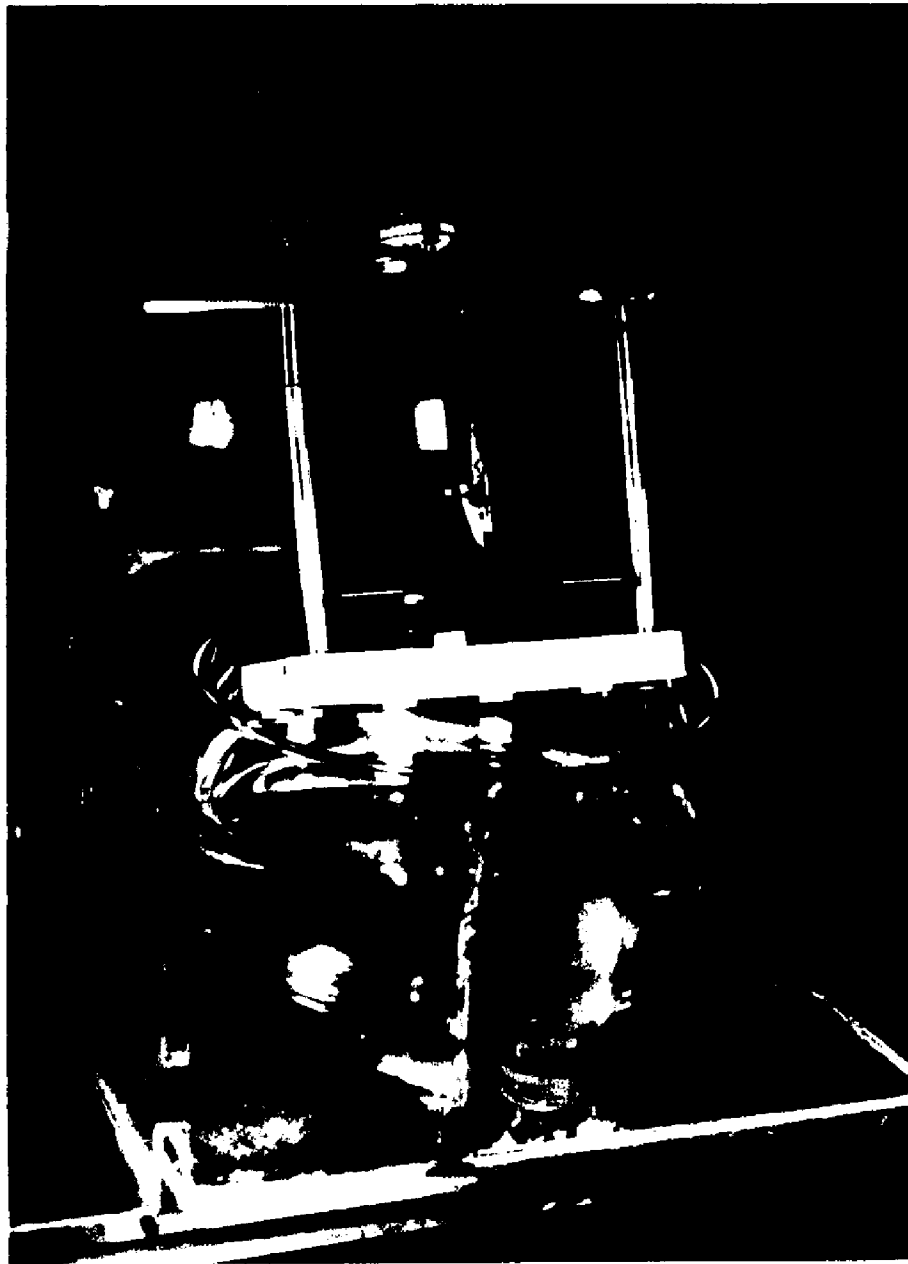
diffusion direction. In order to avoid introducing defect structure during foil preparation, the foils were electropolished directly from the diffusion couples, and no scalpel trimming was done in the vicinity of the foil sample. Since success in obtaining suitably thin foils depends markedly on the starting thickness, only the thinner couples were selected for foil preparation.

Electropolishing was done with the unit* shown in Fig. 9. This dual-jet unit features hollow stainless steel cathodes through which the electrolyte is pump-circulated to impinge on the sample surface. The 10% KCN electrolyte was maintained near 2°C (35°F) by ice water circulated around and below the glass dish containing the electrolyte. It was found advantageous to replace the electrolyte 2 or 3 times during each foil electropolish and to continuously interrupt the voltage in an on-off mode (usually 2 sec. on, 1 sec. off) in order to remove the anolyte layer.⁹⁷ Stop-off (nonconducting) paint was used on the sample to maintain masked edges and to mask the rapid-polishing Ag-rich face of the couple so that terminal portions of the slow-polishing Au-rich material could be polished away. The optimum polishing voltage during electropolishing was selected by maximizing the brightness of the sample surface as revealed by a reflected beam of focussed light.**

The foils were examined in a Philips EM300 TEM operated at 100KV. A liquid nitrogen anticontamination device was employed to minimize

*Purchased from Precision Scientific Co. 3737 W. Cortland St., Chicago, Ill. 60647.

**The surface appeared bright at the proper voltage, etched at under-voltage, and hazed a bluish-grey, or pitted, at overvoltage. The clear electrolyte did not obscure these observations.



Diffusion couple to be electropolished is shown positioned between jet cathodes. The sample-cathode assembly lowers into beaker of electrolyte for electrothinning operation.

Fig. 9. Dual-jet electropolishing unit.

foil contamination. The foils were manipulated extensively in the goniometer stage in order to bring otherwise-invisible or obscure defect structure into contrast.

Following the TEM work, the chemical composition of each thin foil was determined in the electron microprobe. Each foil was cut in two and each segment was flat-mounted on an aluminum block to expose either side of the foil to the microprobe beam. This was done so that the very minor chemical composition difference across the thickness of the foil could be accounted for by averaging the two values. The foil segments were cemented and electrically-grounded to the mounting block with AlkadagTM, a colloidal suspension of graphite in alcohol. During the analysis, the microprobe beam was positioned as close to the foil's thinnest edge as possible. Because of matrix effects from the underlying Al and the roughness of the foil samples, the composition values of the foils can only be approximate, probably to ± 0.05 atom fraction.

The TEM effort was severely hampered by problems encountered during thin foil preparation. These problems are identified here so that they might be considered if and when similar experiments are attempted. The original intent was to obtain foils of different compositions by preparing them from various positions along the concentration gradient of the couples. This goal was seriously impeded by two electropolishing complications. The first of these was caused by the highly-porous region that had been generated in the Ag-rich side of the couple during diffusion. During electropolishing, accelerated and nonuniform attack occurred sporadically along the por-

osity, resulting in a rough, spongy surface with no thin sections suitable as foils. Over 20 diffusion couples were expended in various attempts to circumvent this problem, all to no avail. The foils finally obtained were, therefore, all from the Au-rich portion of the couples. The second impedance to obtaining good thin foils was caused by the steep concentration gradients across the thin-sheet couples. As electropolishing removed material, the Ag-Au surface alloy being polished was continuously changing. This required nearly continuous adjustment of the electrode potential (from 5 to 30V) because the correct polishing voltage is strongly dependent on composition in the Ag-Au system.* Such adjustments were often difficult to make accurately. In retrospect, it seems likely that the recently-developed ion bombardment machining devices might be much more suitable for thinning such couples. These devices have recently been made available commercially.**

Scanning electron microscopy:

The cross sections of two diffusion couples were examined in a MAC (Materials Analysis Corp.) scanning electron microscope in order to substantiate the porosity features seen in light microscopy. The instrument was operated at 20KV in the secondary electron mode.

*Examples: Ag polishes well at 5V, whereas 30V is required for Au. At 20V, pure Ag is removed during electropolishing 50 times faster than a counterpart pure Au sample.

** 1. Commonwealth Scientific Corp.
500 Pendleton Street
Alexandria, Va. 22314

2. Edwards High Vacuum Inc.
3279 Grand Island Blvd.
Grand Island, N. Y. 14072

RESULTS AND DISCUSSION

As-Welded Couples

Sound welds featuring minimal interdiffusion zones of 2, 4, or 6 μm were obtained. The welding interface for the 2 μm -deep welds appeared to be linear, whereas both the 4 and 6 μm deep welds exhibited sharp serrations along the entire welding interface. The amplitude of these serrations was equivalent to the magnitude of the welding zones. Porosity was not detected in the 2 or 4 μm -deep welds, but was found in the 6 μm -deep welds. For all couples, the grain size of both the Ag and Au was roughly equal to the couple halfthickness.

Fig. 10(a)* shows a nonmarked couple with a 2 μm -deep weld. After mild etching, the welding interface appeared to be relatively straight and free of porosity. The slight curvature of the couple (concave downward) is attributed to thermal expansion bending which results from the coefficient of thermal expansion of Ag being greater than that of Au. The radius of curvature for such a couple heated to 750°C is calculated to be 2.35 cm in Appendix A. However, bending observed in welded couples was either much less or apparently absent

*The cross section micrographs are usually presented in the following manner: (1) metallographic nickel plating encases the couple, (2) the couple is oriented with the Ag-rich material above the Au-rich material, (3) reported magnifications are the combined metallographic and print enlarging magnifications and do not include any mount magnification that might exist because of sample inclination in the mount (these mount magnifications were found to be typically 2-10%).

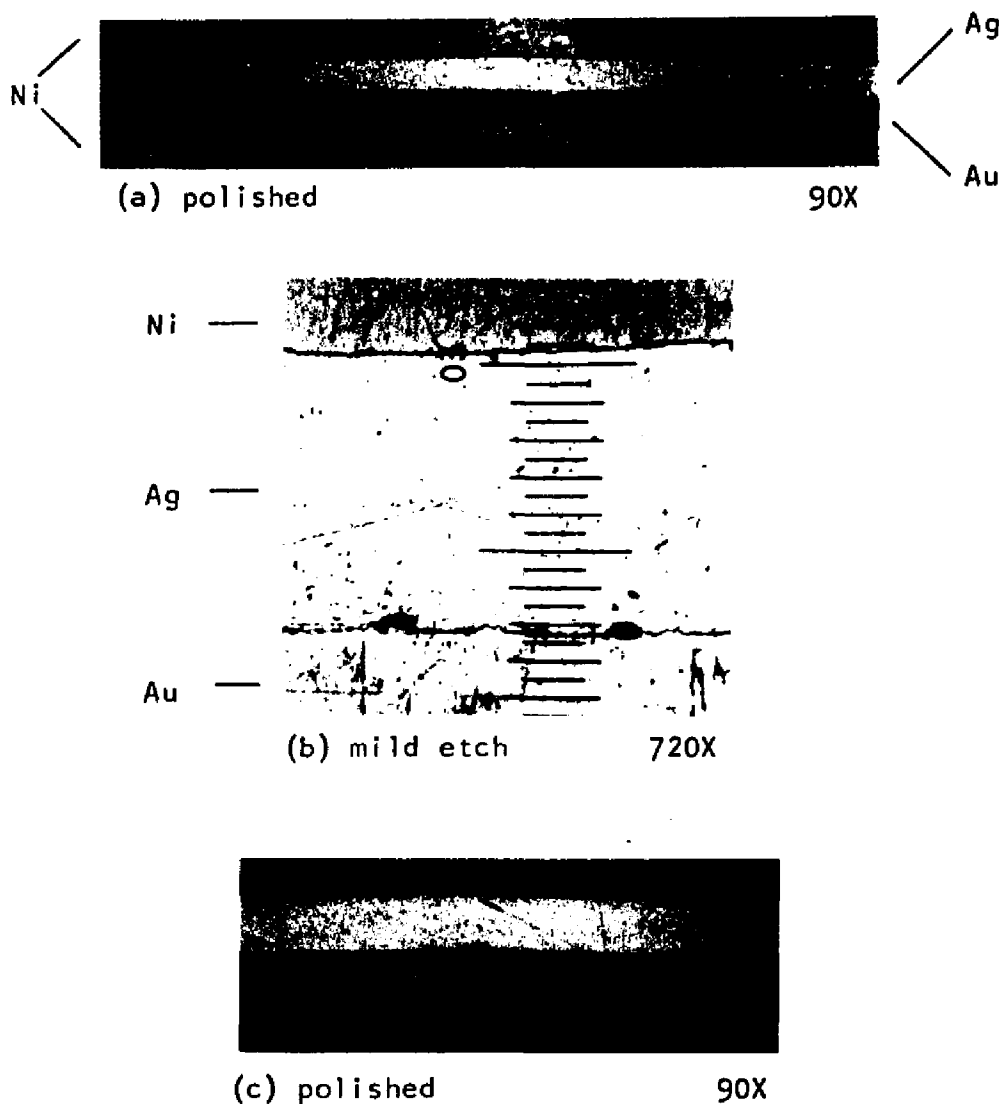


Fig. 10. As-welded couples with and without markers.

(a) 88 μm-thick couple without markers; weld penetration = 2 μm. Slight bending (concave downwards) is due to thermal expansion bending.

(b) 88 μm-thick couple with two iron oxide markers, one on either side of the grating; weld penetration = 4 μm. Note continuous integrity of welding interface.

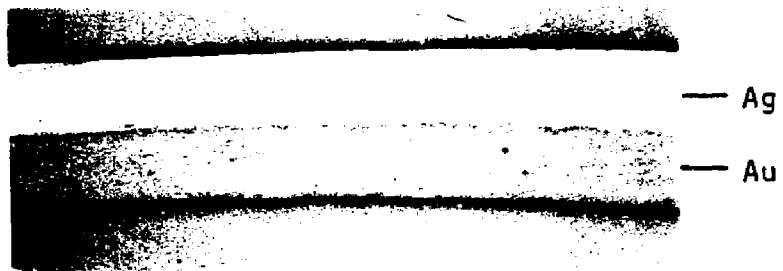
(c) 163 μm-thick couple with 8 μm-diameter tungsten wire marker; weld penetration = 6 μm. Note poor interface bonding in the marker region.

the couples receiving the deeper penetration (4 or 6 μm) welds, and no systematic account could be made of these as-welded curvatures. Because of this and the subsequent observation that diffusion-related bending was considerably more pronounced, the bending of the welded couples was not incorporated into the diffusion-related bending data.

Iron oxide marker particles at the welding interface are shown in Fig. 10(b) in an 88 μm -thick couple having a 4 μm -deep weld. Interface bonding around the marker particles appears to be completely integral, with no apparent degradation of the welding interface. For comparison, Fig. 10(c) shows poor bonding near an 8 μm tungsten wire which was rejected for this reason as a candidate marker material.

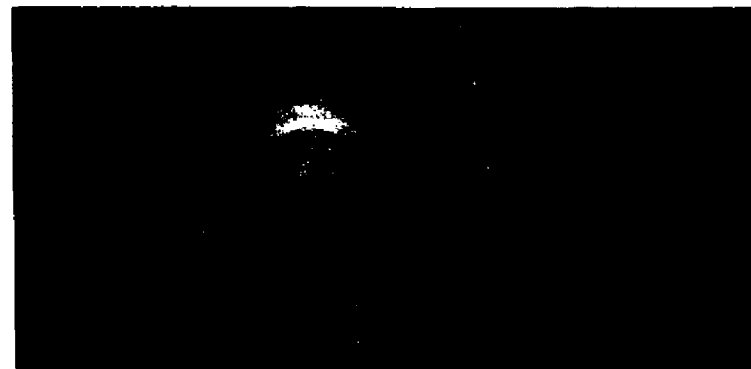
An 88 μm -thick couple having a 4 μm -deep weld is shown in Fig. 11 in the as-polished, mildly-etched, or moderately-etched conditions. As in the case of the 2 μm -deep weld, the 4 μm -deep weld is free of porosity. However, the welding interface is no longer linear but is, instead, serrated. The 6 μm -deep weld in Fig. 12 also displays a serrated interface. While the serrated peaks often advance preferentially into the Ag-rich grain boundaries, they generally exist with a somewhat-regular frequency along the entire welding interface, e.g., Figs. 11(b), (c), and (d). Their peak-to-trough magnitude, perpendicular to the welding interface, is equal to the depth of their corresponding interdiffusion zones of 4 or 6 μm . These sharp serrations tend to become rounded during subsequent diffusion annealing*. This welding interface is a multigrain boundary which was observed in these

*This can be seen in several subsequent micrographs, e.g., Figs. 32 and 49.



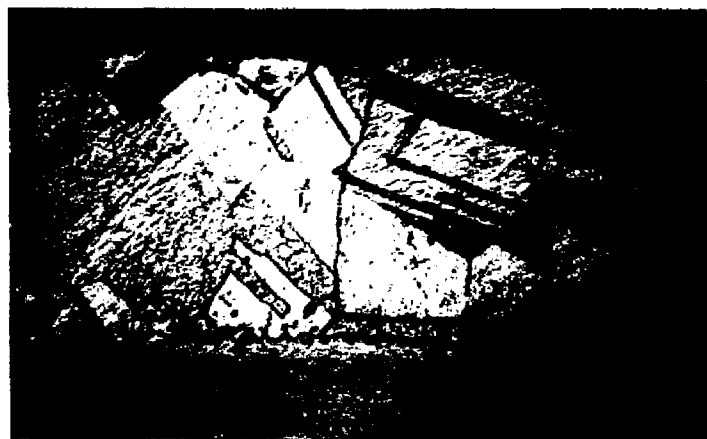
(a) polished

180X



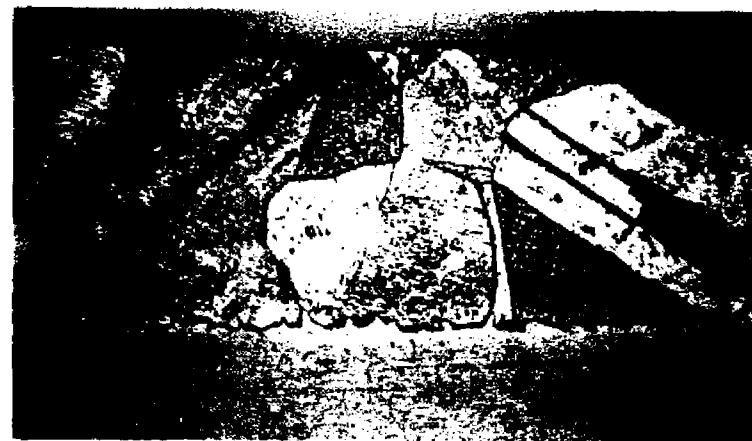
(b) mild etch

360X



(c) moderate etch

720X

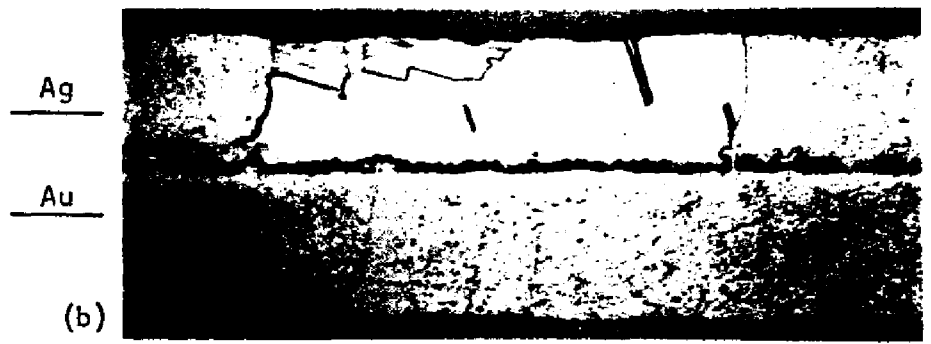
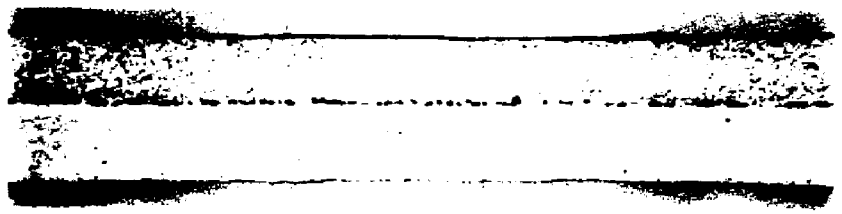


(d) moderate etch

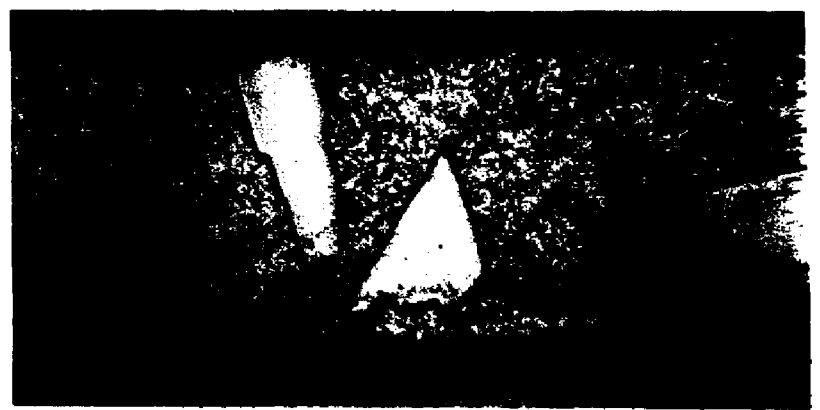
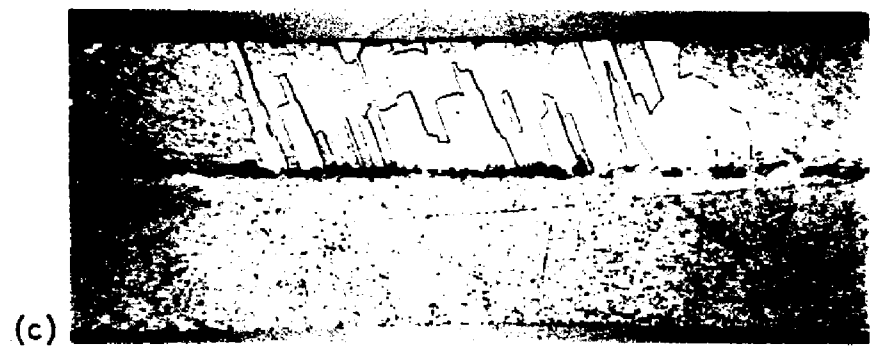
720X

Fig. 11. As-welded 88 μm -thick couple with a 4 μm -deep weld.

(a) mild etch 180X



(b), (c), (d): moderate etch, 360X



(e) this area also seen in (d) 720X

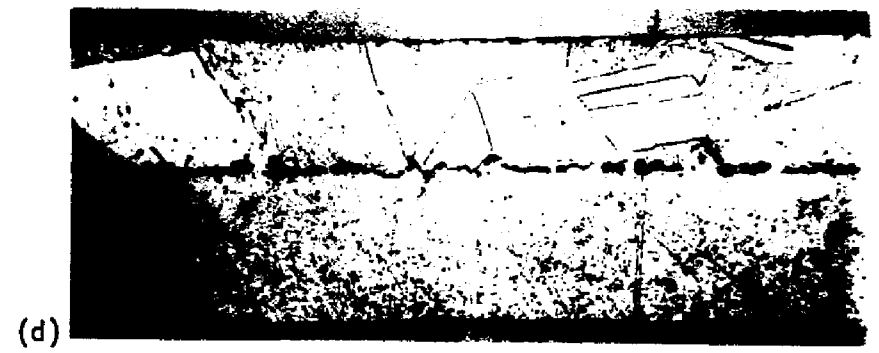


Fig. 12. As-welded 88 μm -thick couple with a 6 μm -deep weld.

couples and others^{3,12,54} to migrate during diffusion toward the side of the couple richer in the faster-diffusing element (Ag, in this case), presumably driven by strain energy introduced during welding and diffusion.³

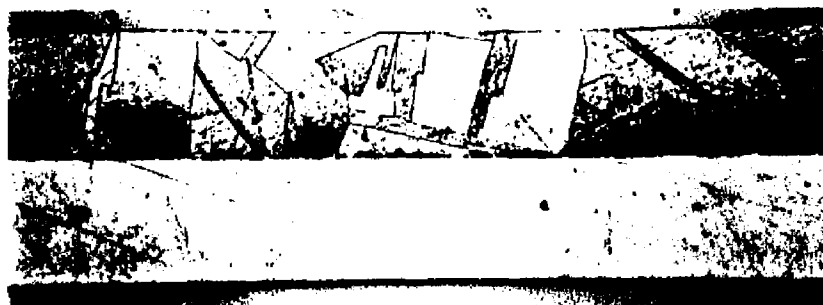
Unlike the porosity-free 2 and 4 μm -deep welds, a thin, discontinuous line of pores was found to exist along the welding interfaces of all couples with 6 μm -deep welds, e.g., see Figs. 12 and 13. Mild etching was required to reveal this welding interface porosity (Figs. 12(a) and 13(c)), and additional etching enlarged it (Figs. 12(b)-(e)). The marker particles appeared to be either slightly less advanced (nearer to the original join) or approximately colinear with the interface porosity, but this was very difficult to judge because of uncertain etchant enlargement of the pores. Most of the marker particles appeared not to be located preferentially at porosity sites. More will be said of this later.

It is seen in Figs. 11 and 12 that the Ag grain size in the 88 μm -thick couples varies considerably and roughly equals the couple half-thickness, C . This correspondence between Ag grain size and couple halfthickness was maintained for all thin-sheet couples, e.g., see Fig. 13 of the 335 μm -thick couples. The Au grains are likewise equivalent to couple halfthickness, as seen in Fig. 14*.

Diffusion Penetration

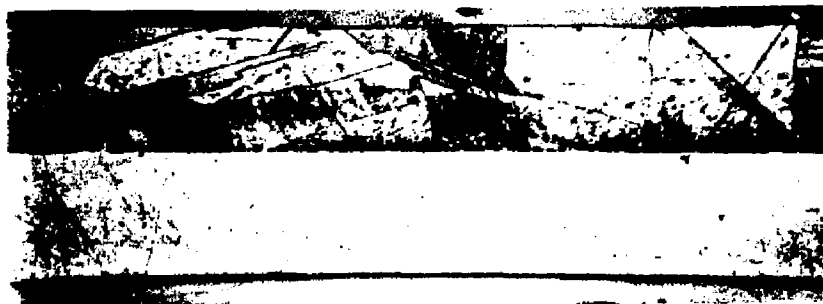
Since values of diffusion coefficients for the Ag-Au system have

*The much more rapid etching of Ag relative to Au is apparent in this and other figures throughout this work.



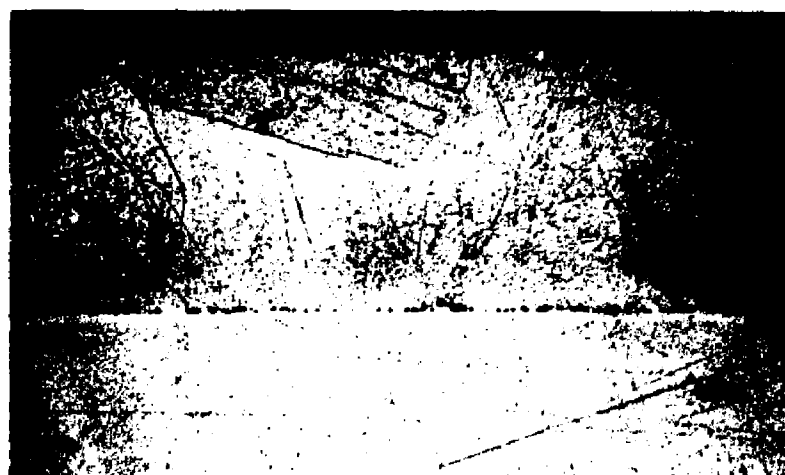
(a) moderate etch

90X



(b) moderate etch

90X



(c) mild etch

180X

Fig. 13. As-welded 335 μm -thick couple with a 6 μm -deep weld.



Ag is leached during the severe etching required to reveal the Au structure.

Fig. 14. Au grains in an as-welded, 132 μm -thick couple.

already been well-established,³⁸⁻⁴⁵ concentration profiles were obtained across several selected couples primarily to determine the extent of interdiffusion. Some general features of the concentration-penetration curves are shown next.

Several concentration-penetration curves from various couples had well-behaved, normal distributions, as shown in Fig. 15 for an 88 μm -thick couple diffused at 750°C for 0.52 hr, resulting in $C^2/4Dt = 17$. This couple is described* as "88 $\mu\text{m}/ 750^\circ\text{C}/ 0.52 \text{ hr}$ ($C^2/4Dt = 17$)", where C = couple halfthickness (44 μm in this case), D = chemical interdiffusion coefficient, and t = net diffusion time.** Obtaining such a well-behaved curve from any given couple usually required several attempts to avoid surface depressions or holes in the porosity zone of the Ag-rich material. Despite these efforts, concentration-penetration curves free of porosity zone effects were often not attainable on many of the couples.*** Typical irregularities in the porosity region of the concentration-penetration curves are shown next. Fig. 16 shows anomalously-low Ag compositions around $N_{\text{Ag}} \sim 0.75 \pm 0.1$ in an 88 μm -thick couple diffused less than an hour. Fig. 17 shows abrupt decreases in Ag composition near $N_{\text{Ag}} \sim 0.80 \pm 0.1$ in a much thicker (335 μm) couple diffused for ~ 16 hr. The more gradual curve irregularities in Fig. 16 and the more abrupt ones in Fig. 17 are both typical of the porosity zone effects observed in all

*This identification format will be retained throughout.

**It is convenient to know that $C^2/4Dt = 18$ corresponds to the interdiffusion zone occupying about $\frac{1}{2}$ of the couple thickness, and $C^2/4Dt = 4$ corresponds to about the semi-infinite limit, i.e., the interdiffusion zone extends entirely across the couple.

***Even when the electron beam passed across a region which was apparently free of pores, underlying (hidden) or adjacent pores would often alter the X-ray output intensity.

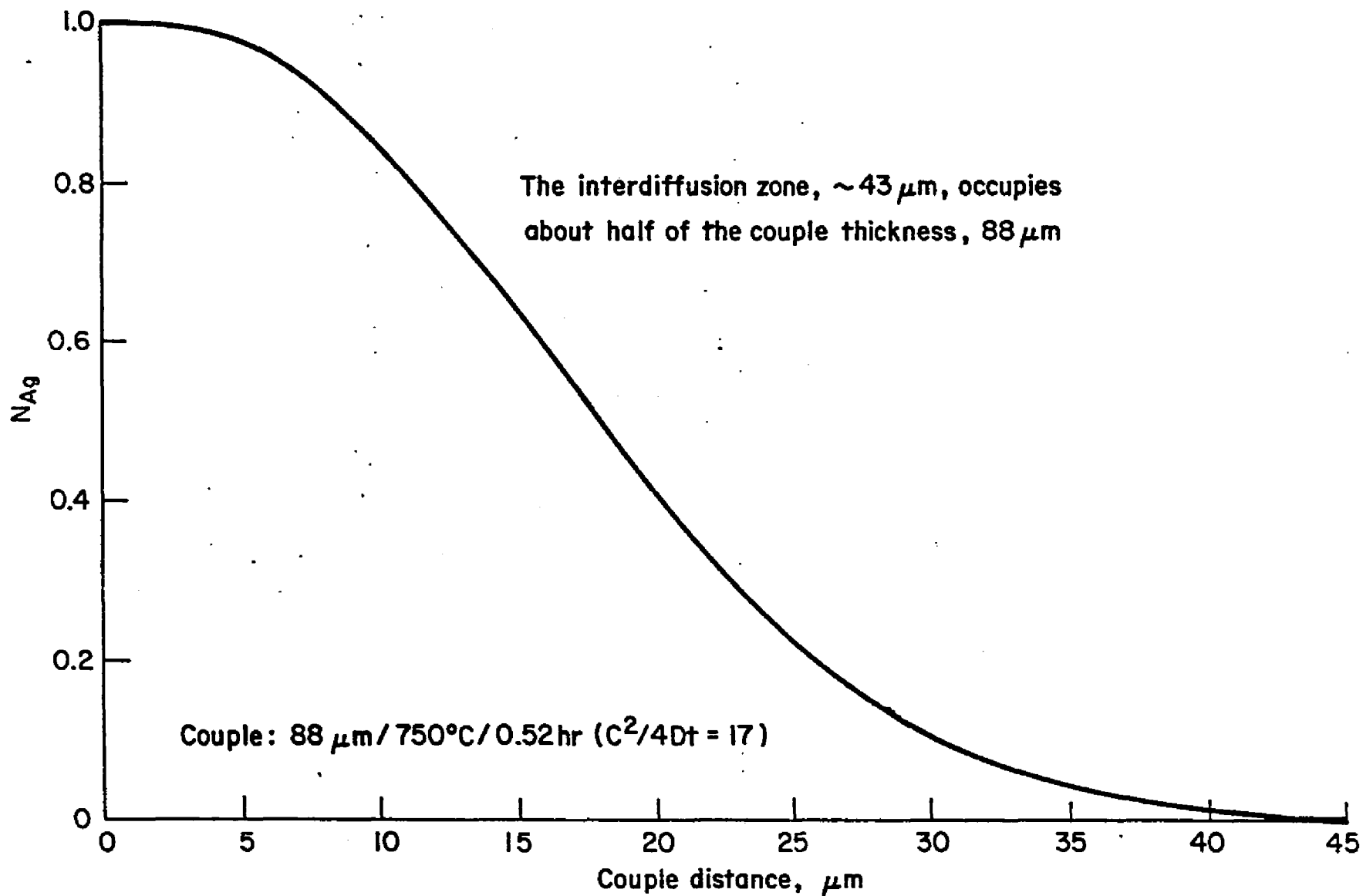


Fig. 15. A well-behaved concentration-penetration curve from an $88 \mu\text{m}$ -thick couple.

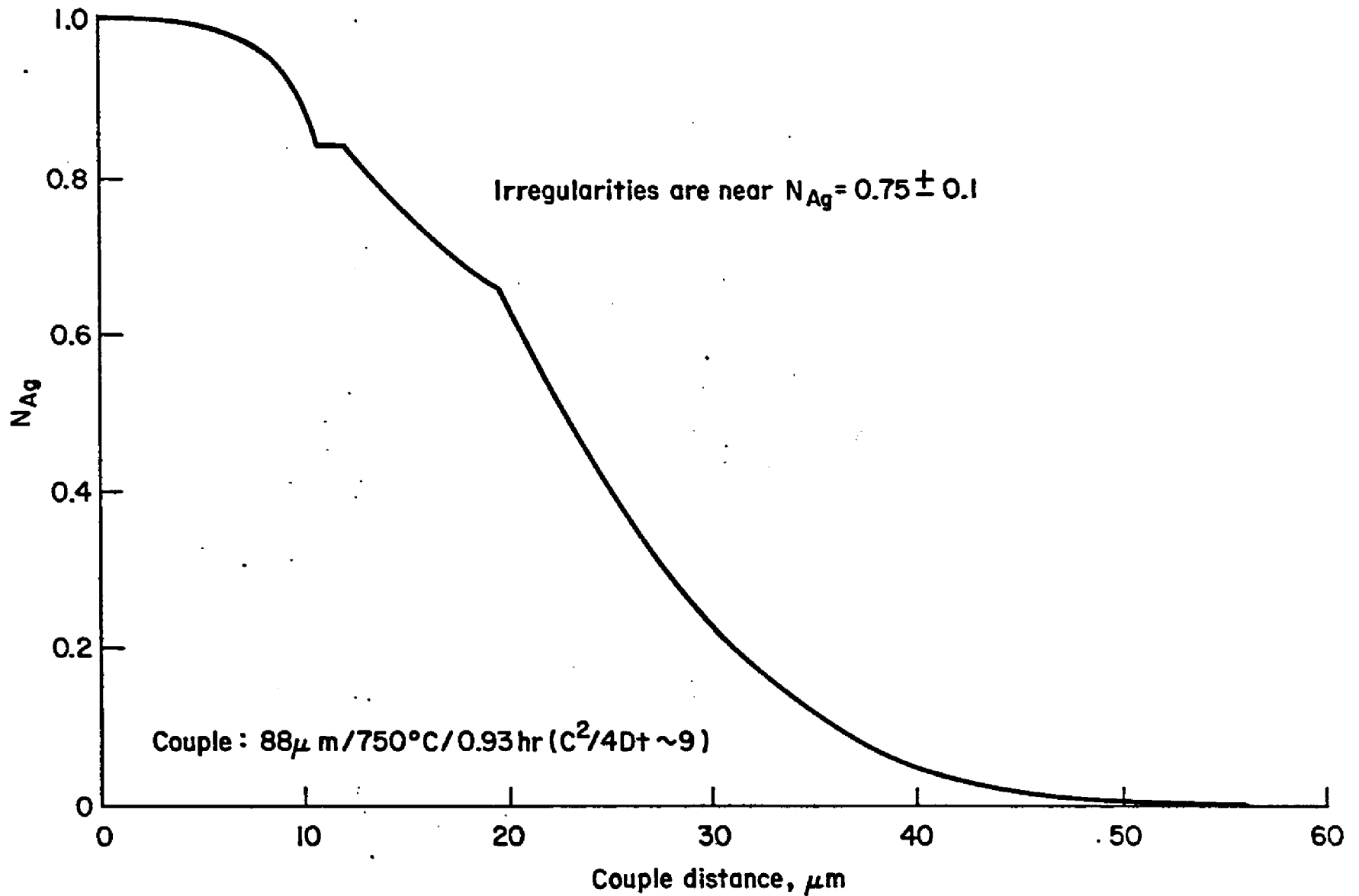


Fig. 16. Irregularities in a concentration - penetration curve of an $88 \mu\text{m}$ - thick couple.

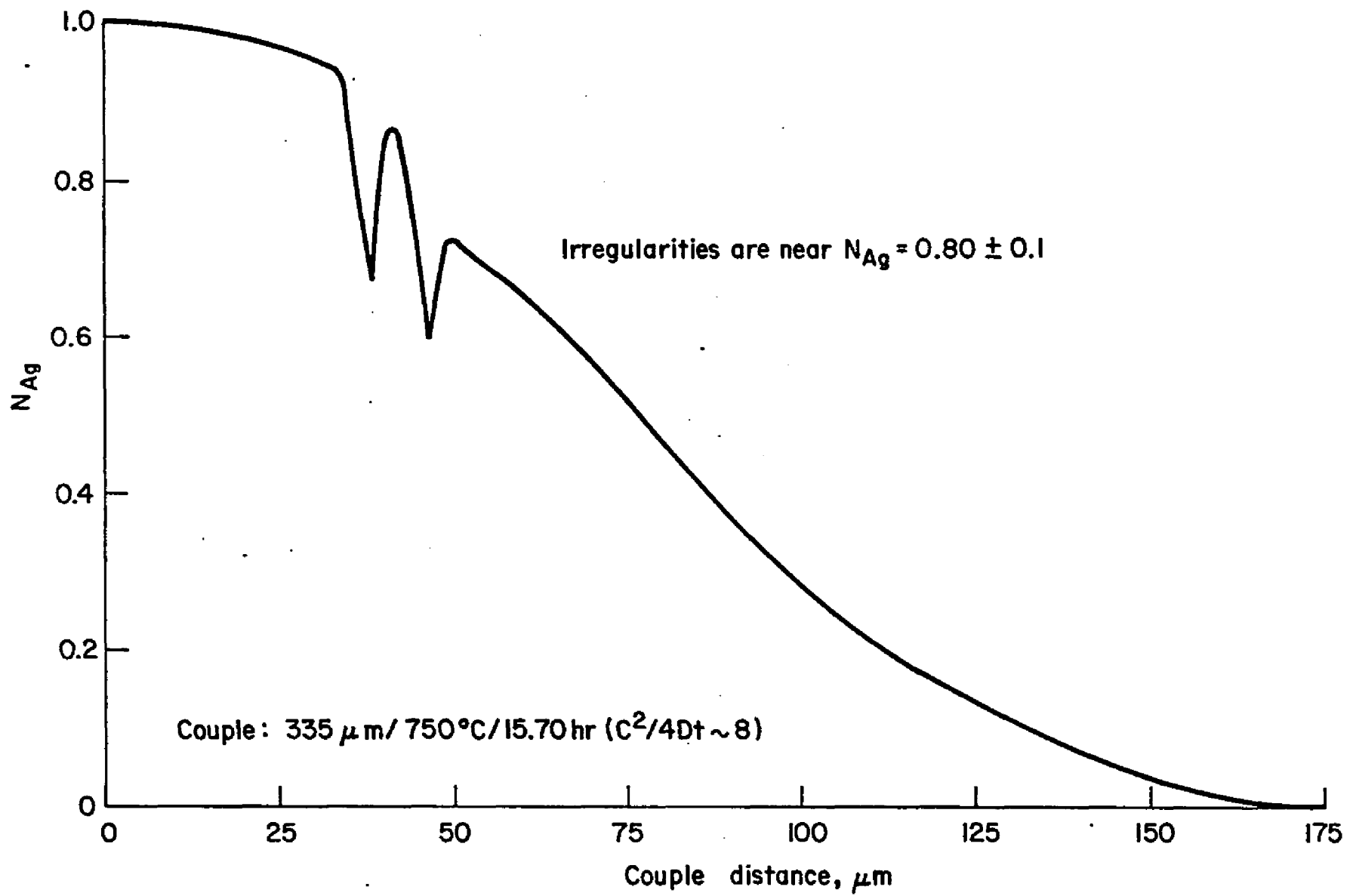


Fig. 17. Irregularities in a concentration-penetration curve of a $335 \mu\text{m}$ - thick couple.

couples containing considerable porosity, regardless of couple thickness or diffusion penetration. An example of similar porosity effects in widely-different couples can be seen by comparing Fig. 16 of a very thin couple (88 μm thick) with the very massive couple (8 mm thick) in Fig. 18. As expected, Au profiles also had anomalously-low compositions in the porosity region. No short-circuiting interdiffusion was detected along or near grain boundaries and pores.

Because of the porosity-related irregularities in most concentration penetration curves, calculations of diffusion coefficients and determinations of the composition at the markers (which were very near the pores) were, in general, not warranted. Even so, some curves were obtained which exhibited little or no apparent anomalies due to porosity. These were analyzed by the Boltzmann-Matano method, Eqn. 4, in order to determine the interdiffusion coefficient, D , at $N_{\text{Ag}} = 0.5$. The results are shown in Table 2, along with the corresponding value taken from Johnson's results.³⁸ The D 's from this experiment are seen to lie with $\sim \pm 15\%$ of the accepted (Johnson) value, with no apparent systematic variations with regard to couple thickness, mechanical constraint, or diffusion time. Agreements within 10-15% are generally taken to be acceptable in determinations of D by the Boltzmann-Matano method. Moreover, much of the variation in D of the thin-sheet couples could be due to large potential errors associated with short diffusion times and couple swelling due to relatively large amounts of porosity. Similar errors in bulky couples are much smaller because of much longer diffusion times and, as will be shown later, porosity occupying smaller fractions of their interdiffusion

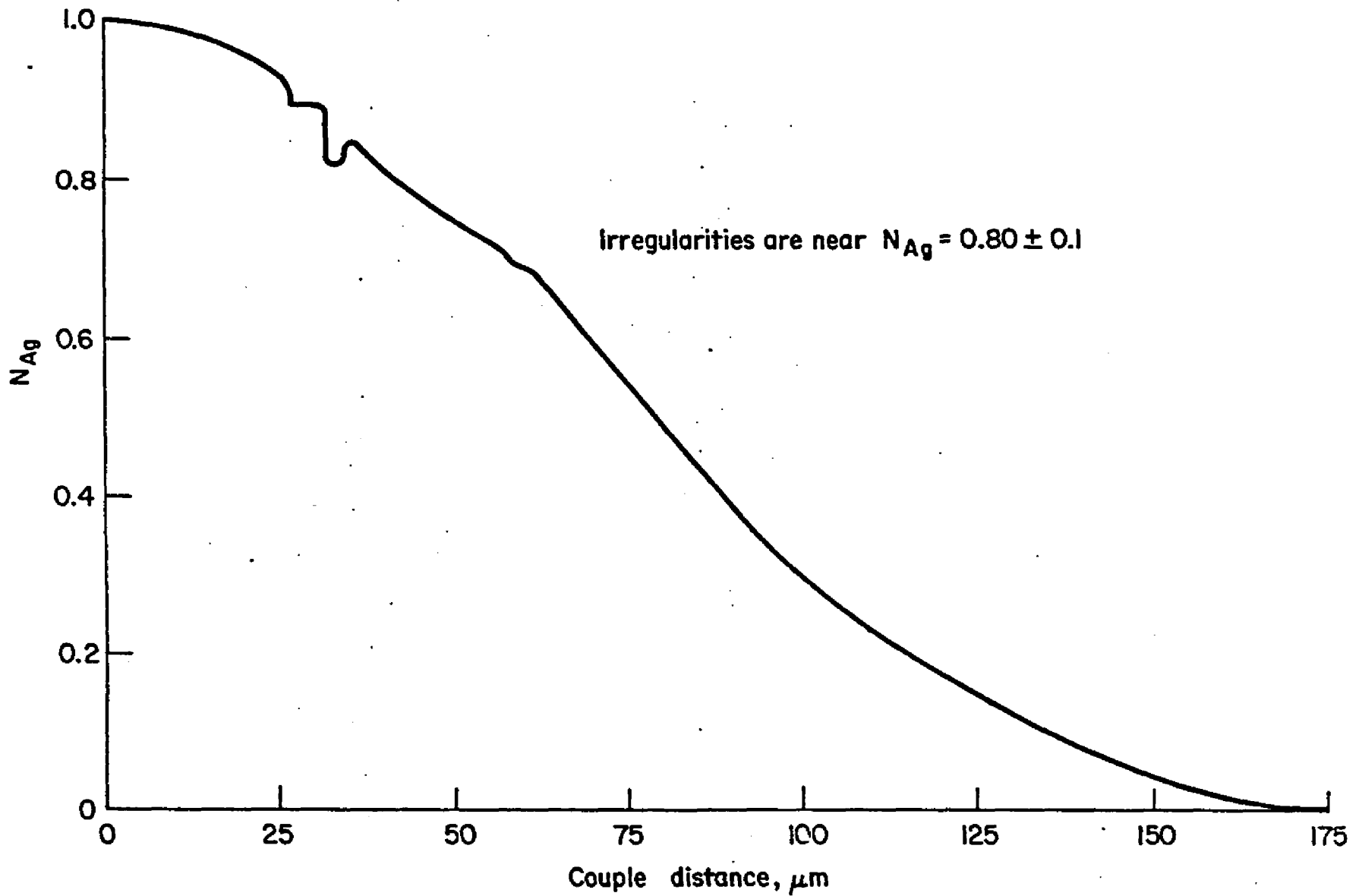


Fig.18. Irregularities in a concentration-penetration curve of a (bulky) 8 mm-thick couple.

Table 2. Chemical diffusion coefficients of various couples.

<u>Diffusion Couple</u>	<u>$D \times 10^{10}$ cm^2/sec^*</u>
88 μm / 750°C/ 0.52 hr ($C^2/4Dt=17$)	1.51
88 μm / 750°C/ 0.93 hr ($C^2/4Dt=9.4$)	1.51
88 μm / 750°C/ 1.48 hr ($C^2/4Dt=5.9$)	1.77
ibid**	1.28
88 μm , mech. constr./ 750°C/ 2.06 hr ($C^2/4Dt=4.2$)	1.28
170 μm / 750°C/ 1.48 hr ($C^2/4Dt=22$)	1.32
335 μm / 750°C/ 0.70 hr ($C^2/4Dt=180$)	1.29
335 μm / 750°C/ 1.48 hr ($C^2/4Dt=85$)	1.36
335 μm / 750°C/ 2.06 hr ($C^2/4Dt=61$)	1.64
335 μm , mech. constr./ 750°C/ 15.70 hr ($C^2/4Dt=8.1$)	1.62
8 mm/ 750°C/ 1.6 hr ($C^2/4Dt=45,100$)	1.47
8 mm/ 750°C/ 5.4 hr ($C^2/4Dt=13,400$)	1.44
8 mm/ 750°C/ 16.2 hr ($C^2/4Dt=4,450$)	1.36
ibid**	1.31
Johnson, ³⁸ tracer methods	1.54

*D = chemical diffusion coefficient in Ag-Au at $N_{\text{Ag}} = 0.5$, $T = 750^\circ\text{C}$

**analysis of a second concentration-penetration profile obtained from a different region in the same couple.

zones. Since variations in D preclude their use in comparing diffusion kinetics of the different couples, another means was sought for this purpose.

When several concentration-penetration profiles obtained from different regions along the same couple were compared, it was found that the depth of interdiffusion remained essentially unchanged,* even when the profiles exhibited different porosity zone irregularities or yielded different values of D . This was characteristic of a wide variety of couples. Thus, the depth of penetration was selected as an appropriate means to compare the kinetics of diffusion between the thin-sheet couples diffused at 750°C for the same times, but having variations in mass constraint (couple thickness), mechanical constraint, or prediffusion deformation. These comparisons, listed in Table 3, indicate that interdiffusion penetration in the thin-sheet couples was independent of either mass constraint (couple thickness) or mechanical constraint (graphite pistons held against the broad faces of the couple to prevent bending during diffusion). Furthermore, moderate amounts of prediffusion plastic deformation (via hand bending) did not affect the extent of the interdiffusion in semi-infinite couples. The invariance of interdiffusion with couple thickness was expected from general diffusion principles. The invariance of interdiffusion with respect to prediffusion straining eliminated the minor concern that interdiffusion might be affected nonsystematically by

*There is in these comparisons an uncertainty of $\sim 1\ \mu\text{m}$ in locating either terminal position of curve because of the very gradual slopes there.

Table 3. Comparing the extent of interdiffusion in various couples.

.....Semi-infinite couples.....

Variation in mass constraint

88 μm / 750°C/ 0.70 hr ($C^2/4Dt=12.4$)	same penetration depth ($\sim 46 \mu\text{m}$)
335 μm / 750°C/ 0.70 hr ($C^2/4Dt=180$)	

Variation in mass constraint

88 μm / 750°C/ 1.48 hr ($C^2/4Dt=5.9$)	same penetration depth ($\sim 61 \mu\text{m}$)
170 μm / 750°C/ 1.48 hr ($C^2/4Dt=21.9$)	
335 μm / 750°C/ 1.48 hr ($C^2/4Dt=85$)	

Mechanical constraint, with variation in mass constraint

88 μm , mech. constr./ 750°C/ 2.03 hr ($C^2/4Dt=4.3$)	same penetration depth ($\sim 69 \mu\text{m}$)
170 μm , mech. constr./ 750°C/ 2.03 hr ($C^2/4Dt=16$)	
335 μm , mech. constr./ 750°C/ 2.03 hr ($C^2/4Dt=62.3$)	

Variation in mechanical constraint

335 μm / 750°C/ 15.70 hr ($C^2/4Dt=8.06$)	same penetration depth ($\sim 177 \mu\text{m}$)
335 μm , mech. constr./ 750°C/ 15.70 hr ($C^2/4Dt=8.1$)	

Variation in prediffusion deformation

88 μm / 750°C/ 2.37 hr ($C^2/4Dt=3.7$)	same penetra- tion depth (88 μm); same respec- tive terminal compositions ($N_{\text{Ag}} = 1$ or 0)
88 μm , prebent to R=11 mm/ 750°C/ 2.37 hr ($C^2/4Dt=3.7$)	
88 μm / prebent to R=4 mm/ 750°C/ 2.37 hr ($C^2/4Dt=3.7$)	

.....Partially-homogenized, couples.....

Variation in mechanical constraint

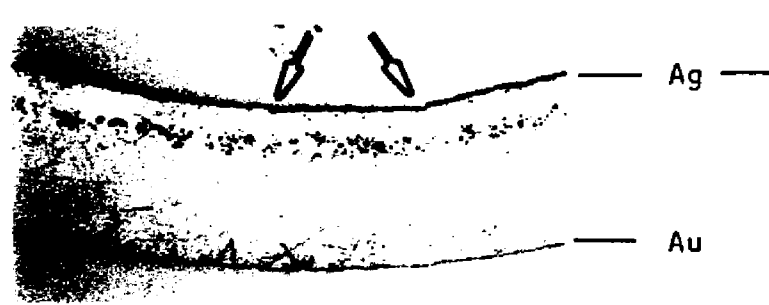
88 μm / 750°C/ 15.70 hr ($C^2/4Dt=0.56$)	same respective terminal compositions ($N_{\text{Ag}} = 0.735$ or 0.320)
88 μm , mech. constr./ 750°C/ 15.70 hr ($C^2/4Dt=0.56$)	

small strains introduced during handling of the extremely soft, thin sheets from which the couples were fabricated. All of the above comparisons of interdiffusion were done primarily to verify that mass or mechanical constraint did not alter interdiffusion so that differences found subsequently in marker shifting, porosity, or bending could be attributed to other factors.

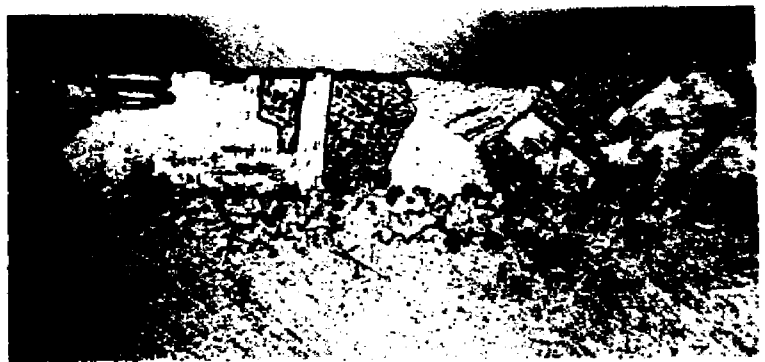
Plastic Deformation Phenomena

Grain Boundary Sliding:

Grain boundary sliding, similar to that found in high-temperature creep samples, was observed along the terminal surfaces of all thin-sheet couples in which interdiffusion zones extended halfway or more across the couples. Its frequency and magnitude increased with increasing interdiffusion. Although it occurred on both sides of the couple, sliding generally appeared earlier along the Ag surface. Examples are given in Fig. 19 and can also be seen in other figures. Sliding was very nonuniform, being very pronounced along some boundaries but essentially nonexistent along others which were similarly inclined to the surface. Such anisotropy of grain boundary sliding has been shown to be very large in low-stress creep tests of pure Ag wire, where sliding rates varied by a factor of 200 or more from one grain boundary to another.⁹⁸ The same work⁹⁸ revealed that sliding did not occur along twin boundaries; this was also true for the couples of this research. Grain boundary sliding is not reported for bulky couples, but it has been observed in nonbending, thin brass sheets dezincified from all surfaces.⁹



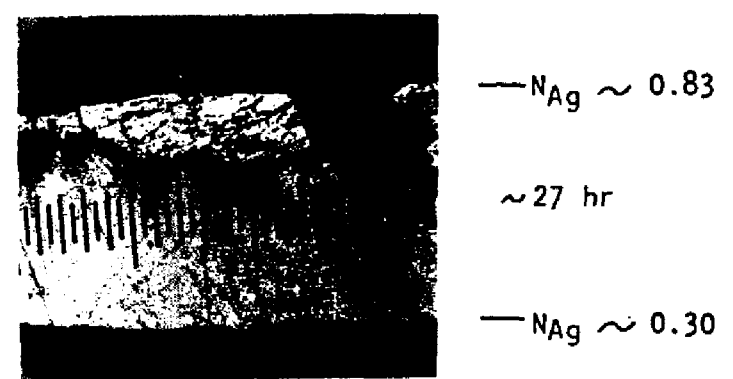
(a) polished 180X



(b) same couple as (a), etched 720X



(c) mildly etched 240X



(d) etched 180X

Fig. 19. Grain boundary sliding. (a),(b): $88 \mu\text{m} / 750^\circ\text{C} / 2.37 \text{ hr}$, diffused to about the semi-infinite limit. (c),(d): $132 \mu\text{m} / 750^\circ\text{C} / \text{times shown}$, partially homogenized.

Destruction of Original Crystalline Boundaries, Subgrain Formation, Recrystallization, and Grain Growth:

Plastic deformation in diffusion zones was evidenced by the disappearance (metallographically) of original crystallographic boundaries near the porosity zone. This is shown for twin boundaries in Fig. 20, and for both twin and grain boundaries in Figs. 21(a) and (b). This boundary destruction began very early in the diffusion process (at or before 0.5 hr at 750°C) and persisted into the homogenization stage. In substantially-diffused couples, large subgrains were frequently found in regions where diffusion flow and diffused-induced stresses had been greater earlier in the diffusion process. This is shown in Fig. 21. After extensive interdiffusion, the subgrain regions appeared to recrystallize, and grains from the Au-rich of the couple migrated across the original join and into the recrystallized regions on the Ag-rich side. These recrystallization and grain growth processes are seen in the partially-homogenized couple of Fig. 22.

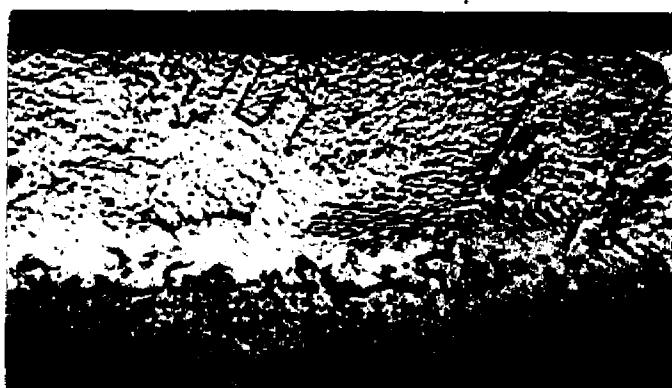
TEM Substructure:

TEM of thin foils electropolished from the Au-rich side of thin-sheet couples revealed that substructure had also formed there during diffusion. Subgrains ranging in size from about 1 to several microns in diameter were characteristic of the foils. This is shown in Figs. 23 and 24. This type of TEM substructure is also produced during creep.^{99,100} Fig. 23 shows stacking faults which were generated at the foil's edge during examination. The very mobile partial dislocations which generated these stacking faults moved rapidly far into the foils until being arrested at boundaries (subgrains, twins, or



(a) 0.52 hr

etched, 720X



(b) 0.52 hr

etched, 720X



(c) 1.48 hr

etched, 780X

Fig. 20. Destruction of twin boundaries. This is shown (arrows) in the plastic deformation regions in the interdiffusion zones of the semi-infinite couples $88 \mu\text{m} / 750^\circ\text{C} / \text{times shown}$.

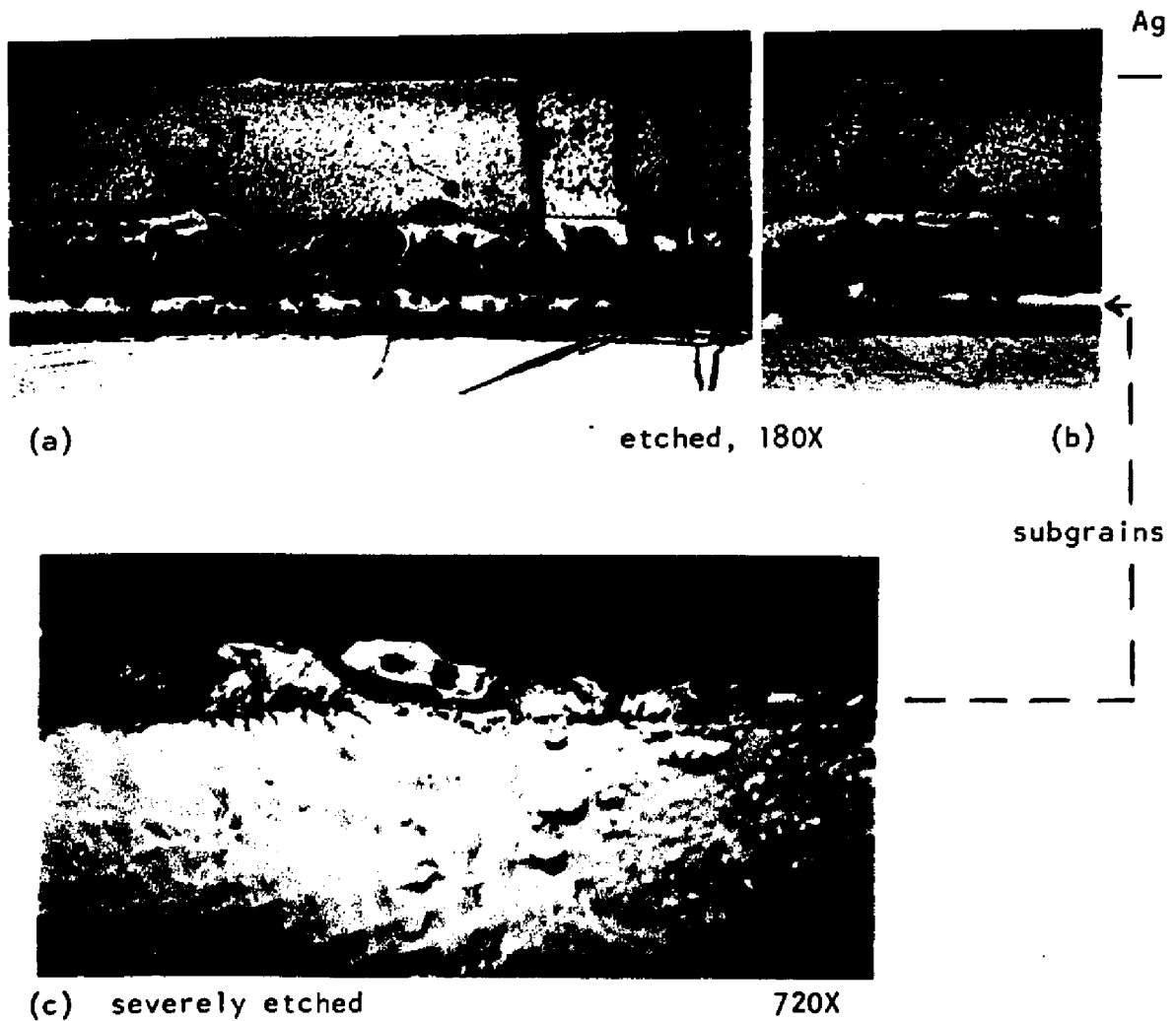
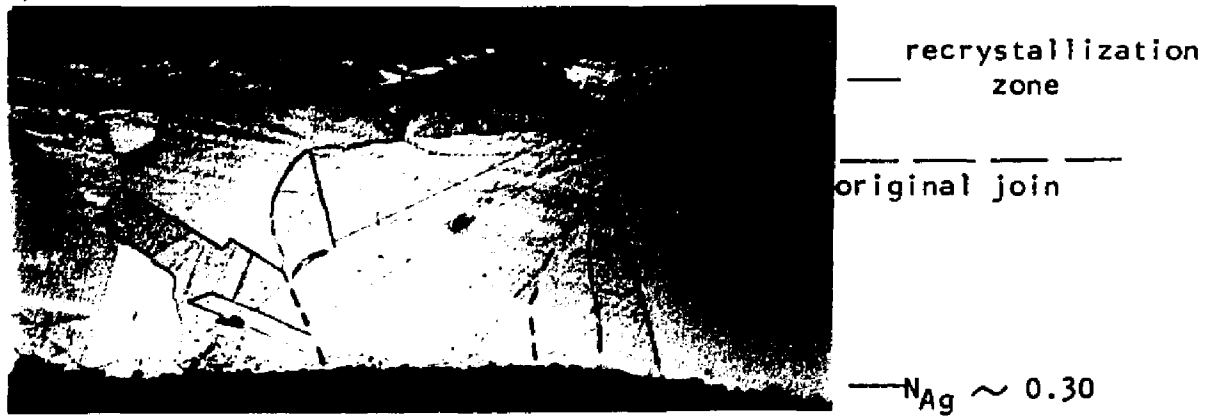


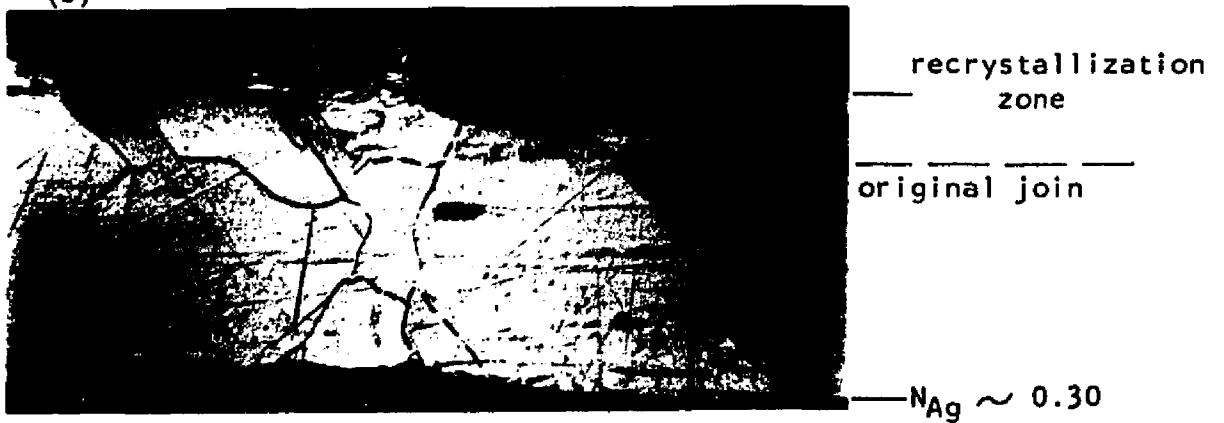
Fig. 21. Boundary destruction and subgrains. Shown is the semi-infinite couple $335 \mu\text{m} / 750^\circ\text{C} / \sim 24 \text{ hr}$. (a), (b): destruction of twin (t) and grain (g) boundaries; (porosity is enlarged by etching). (c): subgrains are revealed by additional etching, which also leached away porosity and much of the Ag-rich material. The dotted arrow to (b) indicates the location of the subgrains prior to their being revealed by additional etching.



(a)



(b)



(c)

Fig. 22. Recrystallization and grain growth. Shown at 360X is the partially-homogenized couple 132 μm / 750°C/ \sim 27 hr. The porosity zone and some Ag-rich material leached out during etching. Dash marks were added to faint boundaries.



(a) 33,000X

The partial dislocations generated at the edge of the thin foil in (b) moved into the interior of the foil where they were arrested at the subboundaries in (a). The dislocations actually traversed a much greater distance than is indicated by the dashed lines. A portion of the area seen in (a) is included in (c).

Fig. 23. TEM defect structure.
 Couple: $132 \mu\text{m} / 750^\circ\text{C} / \sim 6 \text{ hr}$,
 diffused about to the semi-infinite
 limit. Thin foil composition
 is $N_{\text{Ag}} = 0.38$. Parts (c)-(f)
 follow.

(continued---)



(b) 53,100X

edge
of
thin
foil



(---continued) Fig. 23(c).

75,000X

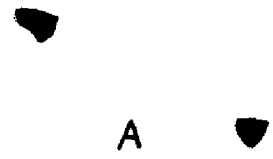


(d)
98,500X



(e)
98,500X

enlargement
of region A
in (e).



(f)
5000,000X

100 Å
|—|

(---continued) Fig. 23 (d), (e): subboundaries and stacking fault tetrahedra. (f): stacking fault tetrahedra.



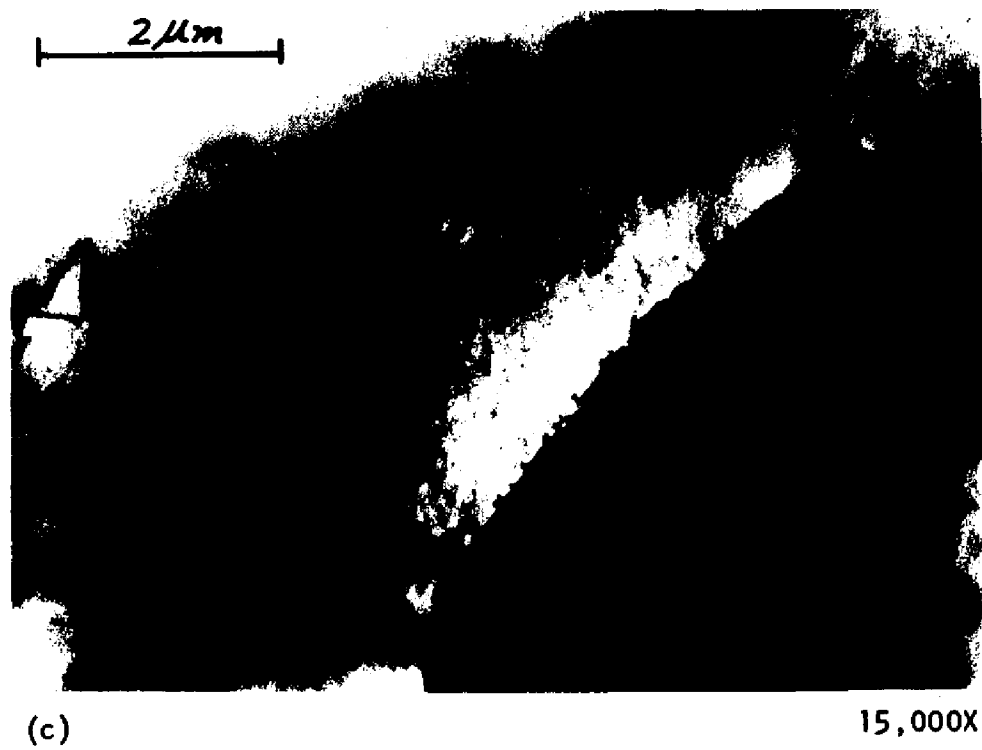
(a)
18,600X



(b)
31,000X

Fig. 24. TEM subboundaries. Shown is the couple $88 \mu\text{m} / 750^\circ\text{C} / \sim 12$ hr, partially homogenized to $N_{\text{Ag}} = 0.83$ or 0.30 . Thin foil composition is $N_{\text{Ag}} = 0.15$. Area "A" is common to (a) and (b).

(continued---)



(---continued) Fig. 24(c): a subgrain having an average diameter of $\sim 3\ \mu\text{m}$.

grains). These partial dislocations, presumably $1/6 \langle 112 \rangle$, were never observed prior to their generation by the electron beam at the foil's edge. Small ($\sim 50\text{\AA}$), widely scattered, stacking fault tetrahedra were occasionally observed, as shown in Fig. 23(e,f). It is uncertain whether these are intrinsic or extrinsic in nature. Judging from their Au-rich compositions, the foils represented vacancy undersaturation regions of their couples. Therefore, the faults may be extrinsic (formed from interstitials). Also, it is possible that the occasional stacking fault tetrahedra resulted from ion bombardment damage to the foil while in the TEM,¹⁰¹ or from a slight vacancy supersaturation generated during rapid cooling of the couple from the 750°C diffusion anneal; this quenching could conceivably yield intrinsic faults. Liu and Powell²⁷ observed subboundaries in their TEM study of Ag/Au couples but did not observe completely-enclosed subgrains as found here. Ayres¹³ observed high dislocation densities and substructure in his Cu/brass couples. Bardeen-Herring sources were not found in this research nor in Ag/Au²⁷ or Cu/brass¹³ couples, but were found in Au-doped Si crystals²⁶ where the atomic mismatch is very high. While the TEM results from this research and that by others^{13,26,27} differ in detail, they all give evidence of considerable plastic deformation in diffusion zones.

Surface Deformation:

Bulge and dent deformation of surfaces which were parallel to diffusion flow was observed for the substantially-diffused thin-sheet (88 to $335\ \mu\text{m}$ thick) and bulky (8 mm thick) Ag/Au couples of this research. This is demonstrated in Fig. 25, where the dents in (a)

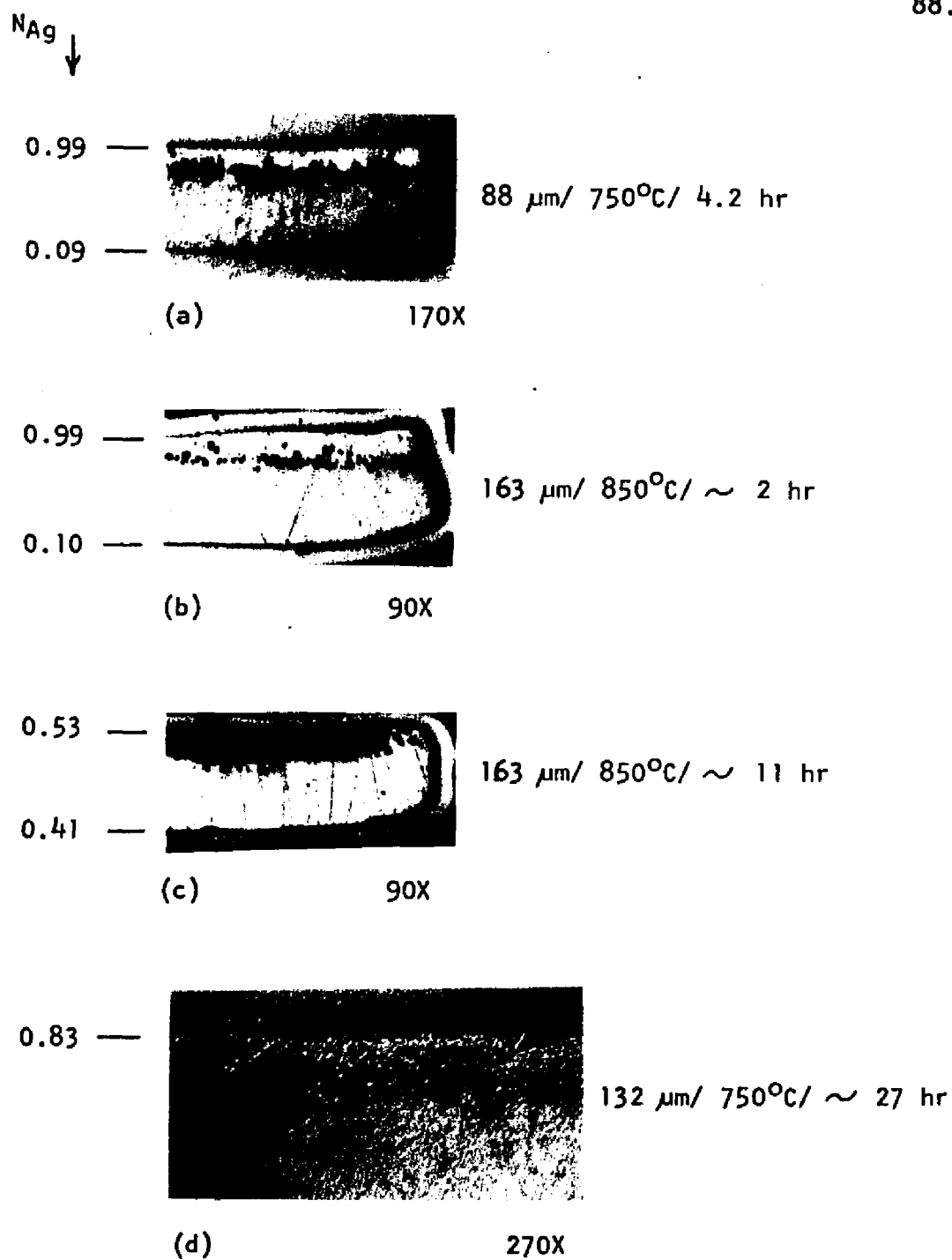


Fig. 25. Surface deformation of partially-homogenized couples. All: as-polished. The "bulge and dent" deformation shown in (a) and (b) disappeared, perhaps by sintering, after additional homogenization occurred, as shown in (c). Surface rippling is shown in (d).

and (b) correspond to the position of the porosity zone. Similar bulge and dent deformation has been observed by others^{28,30,77} in bulky couples, and the positioning of the dent at the porosity zone led them to the tentative conclusion that the bulge and dent were caused by mass flow (loss of mass in the dent side, gain of mass in the bulge side). In addition to this, it seems possible that diffusion-induced stresses perpendicular to the diffusion flow may also contribute to the bulge and dent. This is based on the fact that the regions undergoing mass flow are also regions of diffusion-induced stresses. These stresses could be relieved near the surface by the sense of material relaxation exhibited by the bulge and dent. The bulge and dent deformation no longer exists in the extensively-homogenized couple of Fig. 25(c); more will be said of this later.

Surface ripples were observed on those surfaces which bounded zones of interdiffusion. This rippling was especially evident for partially-homogenized couples where the Ag-rich terminal surface material had undergone considerable homogenization, e.g., Fig. 25(d); (other micrographs also show this, e.g., Figs. 48 and 49). Thermal etching was eliminated as a possible cause of surface ripples when individual sheet samples of pure Ag and pure Au remained smooth, bright, and shiny upon annealing for times and temperatures identical to those of the diffusion anneals. Similar surface rippling was studied in some detail on Ag/Au couples by Ruth³¹ and on Cu/brass couples by Doo and Balluffi.¹² Their analyses showed that rippling can result from dislocation climb,^{32,12} diffusion along dislocation pipes,³¹ and glide caused by diffusion-induced stresses.¹²

Couple Bending:

It will be shown that couple bending increased with increasing diffusion time or temperature, and was inhibited by increasing the couple thickness (mass constraint). Also, unbending of couples occurred during the advanced stages of homogenization.

The increase of bending with increasing diffusion time at 750°C is illustrated in Fig. 26 for $88\ \mu\text{m}$ -thick couples. The bending was relatively uniform, except for slight curling at the corners. The couples bent with the Ag or Ag-rich side forming the concave (interior) surface. The earliest measurable bending occurred after diffusing at 750°C for ~ 0.5 hr., where the interdiffusion zone occupied about half of the couple thickness. Bending progressed during homogenization until the opposite sides of the couples impinged on each other, as seen in Fig. 26. Very weak spot welding at surface contact points was found on these self-impinged couples. Since self-impingement interfered with bending, bending data from such couples were ignored.

Bending radii are plotted against diffusion time in Fig. 27 for a series of $88\ \mu\text{m}$ -thick couples and two pairs of $132\ \mu\text{m}$ -thick couples, all diffused at 750°C . Data for the $88\ \mu\text{m}$ -thick couples includes both the semi-infinite and partially-homogenized stages of diffusion, whereas the data for the $132\ \mu\text{m}$ -thick couples is limited to the partially-homogenized stage. Comparing the bending of the two sets of couples in Fig. 27 illustrates the significant restraint to bending imposed by the larger mass of the thicker couples. This bend-restraining mass was parallel to the diffusion direction, i.e., normal

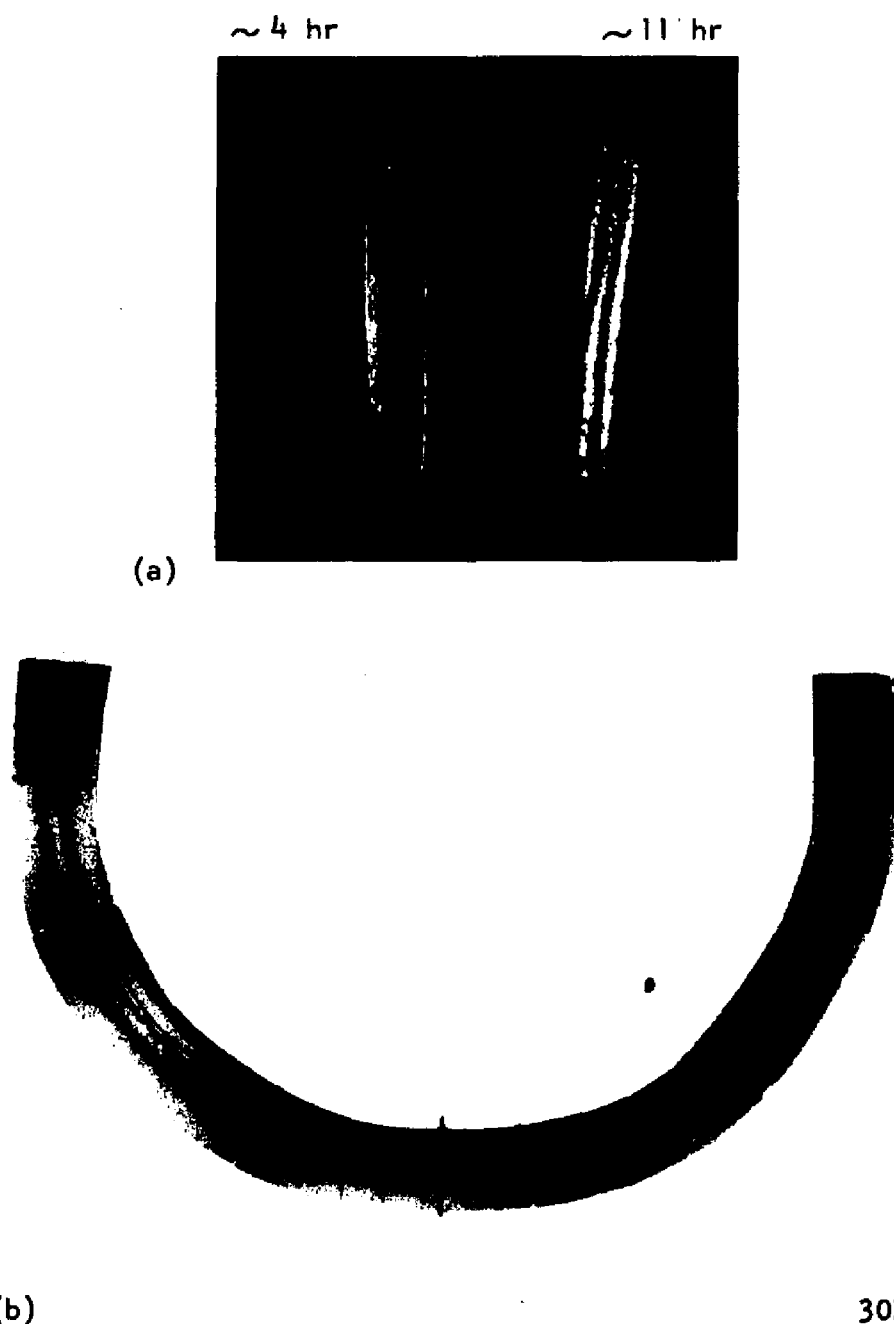


Fig. 26. Examples of diffusion-induced bending.

(a) Couples $88 \mu\text{m} \times 5 \text{ mm} \times 10 \text{ mm}$, diffused at 750°C for times shown. left: $\sim 4 \text{ hr}$, partially homogenized to $N_{\text{Ag}} = 0.99$ or 0.09 ; right: $\sim 11 \text{ hr}$, partially homogenized to $N_{\text{Ag}} = 0.84$ or 0.29 .

(b) as-polished cross section montage of the $\sim 4 \text{ hr}$ couple. The couple, indicated by arrows, is completely encased in metallographic nickel.

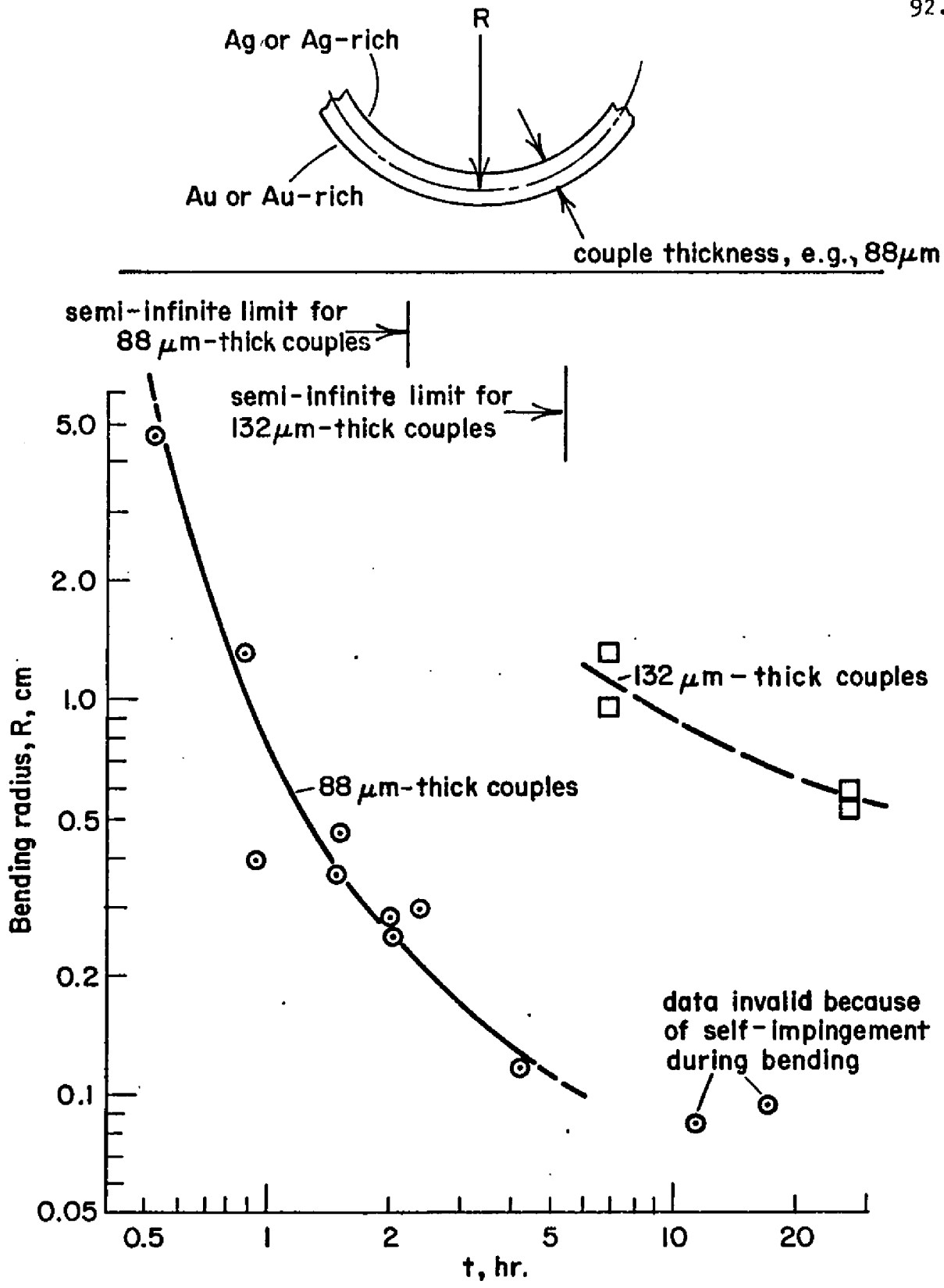


Fig. 27. Couple bending vs diffusion time at 750°C.

to the bending axis.* The mass constraint effect on couple bending was further demonstrated by the absence of measurable bending of 170 and 335 μm -thick couples diffused at 750°C for times comparable to those of the bent, thinner couples of Fig. 27. As expected, all of the mechanically-constrained couples were still flat after diffusion. It is convenient to describe those couples in which bending was restrained by either mass constraint (e.g. quadrupling the couple thickness from 88 to 335 μm) or mechanical constraint (restraining the broad couple faces between firmly-positioned pistons) as being "high constraint" couples. "Low constraint" refers to the 88 μm -thick couples that bent readily.

Computer-fitting the bending data of the semi-infinite, 88 μm -thick couples in Fig. 27 yields the expression

$$\log R = 0.876 - 2.08 \log t + 1.39 (\log t)^2 \quad \dots 5$$

, with R in mm and t in hr.

A qualitative check revealed that bending was promoted by higher diffusion temperatures. This was based on the observation that 170 μm -thick couples did not bend measurably during diffusion at 750°C, whereas couples of nearly the same thickness (163 μm) bent drastically when comparable amounts of interdiffusion were obtained at 850°C.

Unlike the 88 μm / 750°C couples, the bent 163 μm / 850°C couples did not self-impinge and become spot welded during homogenization. Instead, they unbent to near-flatness during the advanced stages of

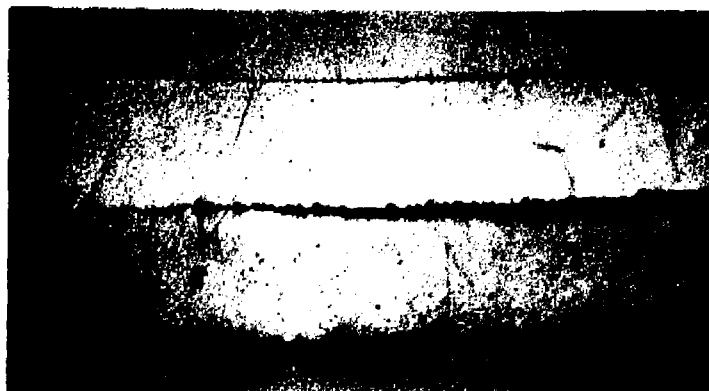
*Experiments with three different pairs of couples showed that bending behavior was not altered when the couple dimensions normal to the diffusion direction were changed from 5 x 10 mm to 5 x 5 mm.

homogenization. Their deformation behavior was as follows. After ~ 0.6 hr, the couples were still semi-infinite and bending was just perceptible.* After 2 hr, homogenization was underway and gross bending was evident. This gross bending was still present in the couple diffused for ~ 6 hr. After ~ 11 hr, where homogenization had decreased the Ag gradient to ~ 0.15 mole fraction across the couple, the couple had unbent to become nearly flat again. This unbending observation was verified by a separate experiment involving an 11 mm-diameter couple, 163 μm -thick, which bent into a deep bowl shape after 3 hr. at 850°C , then unbent to near-flatness after additional diffusion resulted in considerable homogenization. The occurrence of unbending in the advanced stages of interdiffusion eliminates evaporation loss of Ag as a principal cause of bending. Furthermore, evaporation losses were found by weighing to be undetectably small in thin-sheet Ag disks annealed for several hours at 750°C and 850°C in simulations of diffusion annealing.

Internal Cracking:

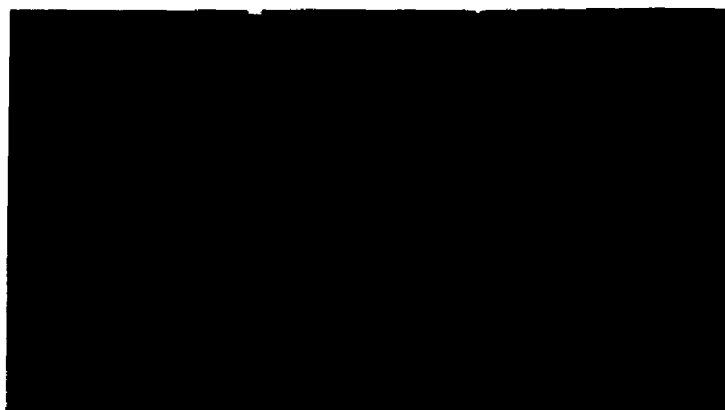
Several diffused couples made early in this research cracked open approximately parallel to the original join. Typical cracking is shown in Fig. 28. The cracking path followed either the pores, or lacking considerable porosity, the welding interface. This is probably because either of these are mechanically weak paths. Welding interdiffusion, couple thickness, diffusion temperature, and mechani-

*Bending descriptions, rather than bending data, are used here because the pie-shape geometry of this set of 4 preliminary trial couples did not permit meaningful measurements.

weld penetration = 2 μm 335 μm / 750°C/ \sim 2 hr(a)
polished
90X

—Ag

—Au

(b)
scanning
electron
micrograph
of crack
to left of
E in (a),
2,000Xweld penetration = 4 μm 335 μm / 800°C/ \sim 9 hr(c)
polished
180X

—Ag

Ag-rich half of couple

Fig. 28. Internal cracking. In (a), E is the path of the electron microprobe beam.

ical constraint all affected the propensity for cracking. The weld depth factors were presented earlier. Porosity and/or the concentration profiles revealed that couples cracked only after considerable interdiffusion had occurred. As seen in Fig. 28(c), cracking was often nonuniform, occurring in some regions before others.* Most often the cracks did not extend along more than half of an entire couple. Cracking was significantly greater in those mass-constrained couples which experienced little or no bending. For example, during 750°C diffusion of couples having 2 μm-deep welds, the bending 88 μm-thick couples never cracked, whereas the nil-bent 170 and 335 μm-thick couples cracked extensively. Comparing cracking behavior for various couples diffused at 750°, 800°, and 850°C revealed that cracking was more prevalent at the higher temperatures. Although 6 μm welds prevented cracking of the thin-sheet couples diffused at 750°C, the same couples cracked during 850°C diffusion. No cracking occurred at 850°C for 163 μm-thick couples welded deeply to 30 μm. Also, none of the mechanically-constrained couples cracked. Thus, cracking during diffusion annealing was promoted by either mass constraint or increased diffusion temperatures, and was retarded or prevented by deeper welding. Mechanical constraint always prevented cracking. Internal cracking of one sort or another has been reported for a variety of couples,^{3,9,30,31,56,57} but with one exception,⁹ few if

*About 30 μm of interdiffusion occurred in the couple in Fig. 28(a). About 20 μm of interdiffusion occurred in the left (nonporous) region of the couple in (c), compared to ~ 120 μm for its right (porous) region.

any details concerning the cracks were given. Some of the cracks were attributed to faulty welding,^{3,56,57} while others were believed due to diffusion-induced stresses.^{9,30,31} Results of the bending analysis, to be presented later, indicate that diffusion-induced stresses are responsible for cracking of the thin-sheet couples of this research.

General Remarks:

The plastic deformation phenomena, namely, grain boundary sliding,⁶³ destruction of original crystalline boundaries,^{3,6,12,28,29} generation of dislocations or substructure,^{3,6,12-21,23,28} recrystallization and grain growth,^{3,12,28,29} small surface ripples,^{12,28,31} large bulge and dent deformation of surfaces which are parallel to the diffusion flow,^{28,38,77} internal cracking,^{9,10,30} and couple bending,^{6,16,27} have been observed in other binary couples (solid/solid or vapor/solid types). In some cases, two, three, or four of these processes were observed for a single type of couple e.g., Cu/Ni,⁶ Cu/brass,^{9,12} Ag/Au.^{27,38} But in no case, save for the thin-sheet Ag/Au couples of this research, have they all been observed to occur in a single type of couple. Thus, all of the above phenomena are common to at least one type of couple (thin-sheet Ag/Au), and consideration of the above-referenced evidence indicates that they are common to all Kirkendall couples. Furthermore, all of these plastic deformation phenomena occur in a system (Ag/Au) which is practically free of atomic mismatch. Hence, while atomic mismatch undoubtedly produces deformation stresses, stresses which arise solely from vacancy

gradients are sufficient to produce all of the observed plastic deformation phenomena in Kirkendall couples.

It is generally accepted that diffusion-induced stresses are responsible for grain boundary sliding, destruction of original crystalline boundaries, generation of dislocations or subboundaries, recrystallization and grain growth, and internal cracking. Although the nature of surface deformation is not well understood, both diffusion-induced stresses and mass flow effects appear to be related to both surface rippling and bulge and dent formation. However, it is not at all clear at this point whether diffusion-induced stresses or mass flow, or both, are responsible for couple bending. Barnes⁶ and Queisser¹⁶ stated that diffusion-induced deformation stresses were the cause of bending, whereas Liu and Powell²⁷ suggested that accommodation of mass flow by dislocation climb parallel to diffusion flow could contribute to bending. The latter authors also observed that such bend-producing climb would not produce marker shifting. Experimental results from the present research will be employed below to show that couple bending is caused primarily by diffusion-induced stresses. To do this it is first necessary to present marker shifting results.

Marker Shifting

Marker shifting results representing 286 marker positions in 15 couples are given in Table 4. (Appendix B describes in detail the method of making marker shifting measurements.) Some indication of marker distributions within each couple is given in Table 4 and depicted graphically for couples 1-5 in Fig. 29. These show that scat-

Table 4. Marker shifting data.

No.	<u>COUPLE</u> Identity	<u>MARKER DATA</u> *			
		\bar{X}_m (μm)	S, std. dev. (μm)	Range about \bar{X}_m (μm)	n, no. markers
1	88 μm / as-weld for couples 2-5	--	1	4 (-2 to +2)	32
2	88 μm / 750°C/ 0.52 hr ($C^2/4Dt=17$)	8	1.5	5 (-3 to +2)	13
3	88 μm / 750°C/ 0.93 hr ($C^2/4Dt=9.4$)	11	1.5	5 (-3 to +2)	11
4	88 μm / 750°C/ 1.48 hr ($C^2/4Dt=5.9$)	12.5	2.5	9 (-4 to +5)	17
5**	88 μm / 750°C/ 1.98 hr ($C^2/4Dt=4.4$)	12.5	2	6 (-3 to +3)	18

(continued---)

* \bar{X}_m = average marker shift = $\sum_{i=1}^n X_i/n$, where n = number of individual marker shift values, X_i .

S = standard deviation = $\left[\sum_{i=1}^n (X_i - \bar{X}_m)^2 / (n-1) \right]^{1/2}$. \bar{X}_m and S are given to the nearest 0.5 μm because of the 0.5 μm probable measuring error which affected each marker measurement (see Appendix B).

**Marker data are unreliable because advanced markers were entrapped in pores.

Table 4. Marker shifting data--continued

<u>COUPLE</u>		<u>MARKER DATA*</u>			
<u>No.</u>	<u>Identity</u>	\bar{X}_m (μm)	S, std. dev. (μm)	Range about \bar{X}_m (μm)	n, no. markers
6	88 μm / as-weld for couples 7-10	--	0.5	2 (-1 to +1)	32
7	88 μm , mech. constr./ 750°C/ 0.70 hr ($C^2/4Dt=12.4$)	11.5	3.5	7 (-3 to +4)	33
8	88 μm , mech. constr./ 750°C/ 2.06 hr ($C^2/4Dt=4.2$)	20	2.5	11 (-5 to +6)	34
9	88 μm / 750°C/ 15.70 hr ($C^2/4Dt=0.56$)***	22	2	7 (-3 to +4)	10
10	88 μm , mech. constr./ 750°C/ 15.70 hr ($C^2/4Dt=0.56$)***	34	4.5	16 (-8 to +8)	24
11	335 μm / as-weld for couples 12-15	--	1	3 (-1 to +2)	14
12	335 μm / 750°C/ 0.70 hr ($C^2/4Dt=180$)	12	0.5	2 (-1 to +1)	10
13	335 μm / 750°C/ 2.06 hr ($C^2/4Dt=61$)	23	4	13 (-9 to +4)	13
14	335 μm / 750°C/ 15.70 hr ($C^2/4Dt=8.1$)	42	5.5	18 (-9 to +9)	10
15	335 μm , mech. constr./ 750°C/ 15.70 hr ($C^2/4Dt=8.1$)	45	4.5	16 (-9 to +7)	15

***partially homogenized

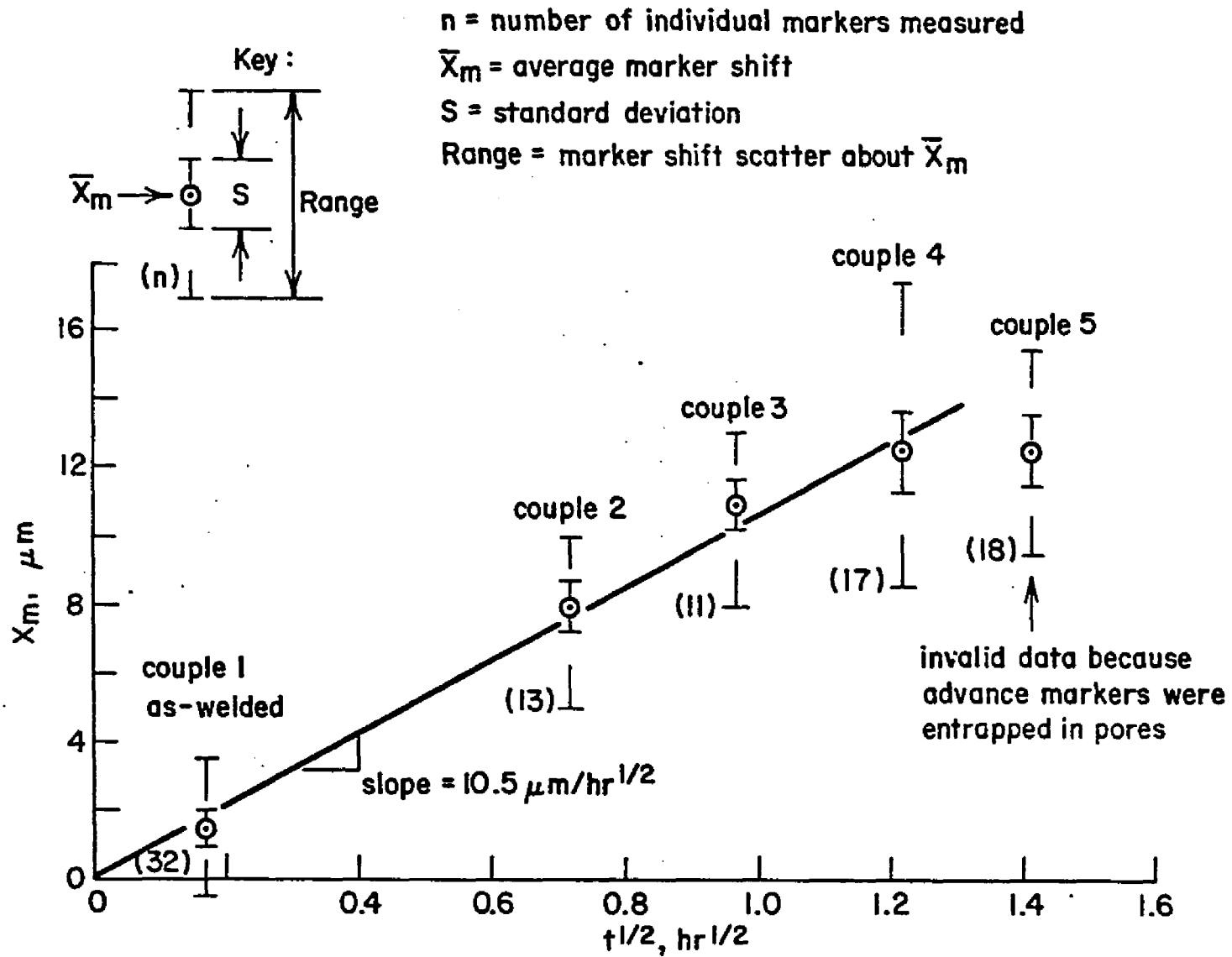


Fig. 29. Marker Shifting for a series of semi-infinite, $88\mu m$ -thick couples diffused at $750^\circ C$.

ter in marker positions within a couple generally grows larger as diffusion increases. Only a small part of this scatter is comprised of the $0.5 \mu\text{m}$ probable measuring error which affects each marker measurement. The standard deviation, S , is included because the markers were generally distributed symmetrically about their average, \bar{X}_m . Values of S for the diffusion annealed couples indicate that $\sim 2/3$ of the markers in any given couple were within $\pm 1/7 \bar{X}_m$ (couple 7) to $\pm 1/20 \bar{X}_m$ (couple 15). For most of the diffusion annealed couples, the entire range (scatter) of marker positions within a given couple is very roughly $1/2$ of its average marker shift, i.e., scatter $\sim \pm \frac{1}{4} \bar{X}_m$. This is less than reported scatter of $\sim \pm \frac{1}{2} \bar{X}_m$ in bulky Ag/Au couples which also employed oxide particles as markers.^{42,45} But the significance of this comparison is questionable because of the much deeper interdiffusion in the bulky couples and other differences such as diffusion temperature, grain size, etc.

Marker shifting for the set of $88 \mu\text{m}$ -thick couples diffused free of mechanical constraint is seen in Fig. 29 to be parabolic according to $X_m = k t^{\frac{1}{2}}$. Porosity-entrapment of some of the more-advanced markers has occurred in the most-diffused couple (couple 5) in Fig. 29. Both the maximum and the average marker shifts are less than predicted by the lesser-diffused couples of the series which were not observed to suffer such entrapment. Because of the uncertainty inherent with markers entrapped in pores, marker shifting data from this couple were not employed in computing the marker shifting expressions.

The average markers shifts, \bar{X}_m , from Fig. 29 and those from other semi-infinite couples are plotted in Fig. 30. From Fig. 30, it is

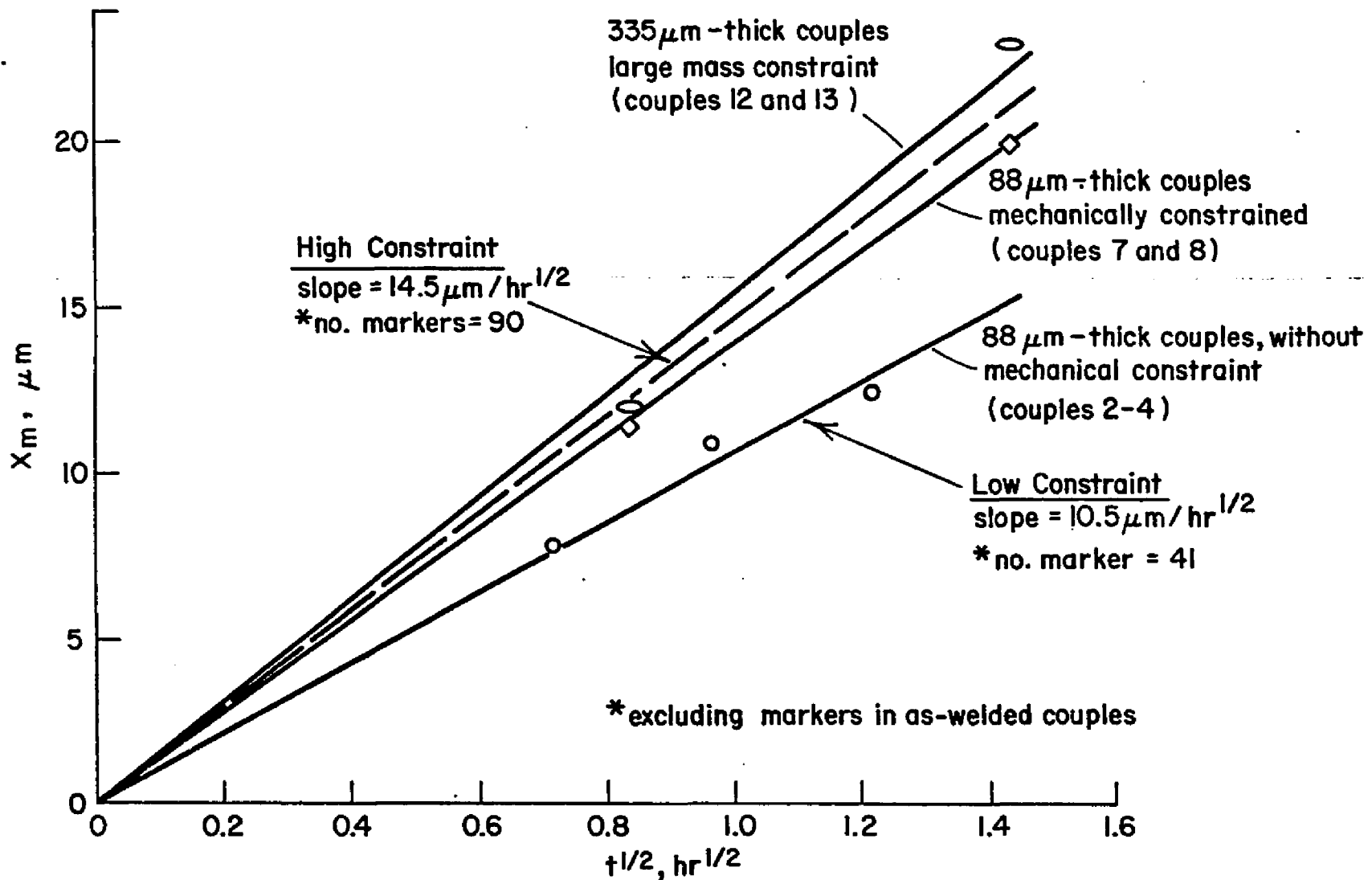


Fig. 30. Equivalent marker shifting enhancement due to mechanical constraint or large mass constraint. All couples: diffused at 750°C, semi-infinite.

seen that marker shifting in couples with large mass constraint (335 μm thick) was practically the same as that in much thinner couples (88 μm thick) which were mechanically constrained. Since these two sets of high-constraint couples exhibit similar marker shifting behavior, their average shifts are represented by the dashed line. It is seen that marker shifting in the high-constraint couples was enhanced relative to the low-constraint couples.

A summary of marker shifting results, including the curves of Fig. 30, is given in Fig. 31. It is seen that marker shifting for semi-infinite couples diffused at 750°C for $t \lesssim 2 \text{ hr}^*$ is given by

$$\text{Low-constraint couples: } X_m = 10.5 t^{\frac{1}{2}} \quad \mu\text{m-hr} \quad \dots 6(a)$$

$$\text{High-constraint couples: } X_m = 14.5 t^{\frac{1}{2}} \quad \mu\text{m-hr} \quad \dots 6(b)$$

Marker shifting enhancement caused by high constraint (mass or mechanical) is given by the difference between the above values,

$$\Delta X_m = 4 t^{\frac{1}{2}} \quad \dots 6(c)$$

The relative marker shifting enhancement, given by the ratio of Eqn. 6(c) over 6(a), is 38%.

The two 335 μm -thick couples (14 and 15), one of which is mechanically constrained, were diffused for $\sim 16 \text{ hr}$. The small difference of 3 μm , or 7%, between the \bar{X}_m values of these two couples is not significant (see Fig. 31). Furthermore, since two markers were found in pores of the couple free of mechanical constraint (couple 14), it is likely that a minor amount of entrapment may have contributed to this small difference. Thus, superposing mechanical constraint onto

*Homogenization of the 88 μm -thick couples begins shortly after 2 hr.

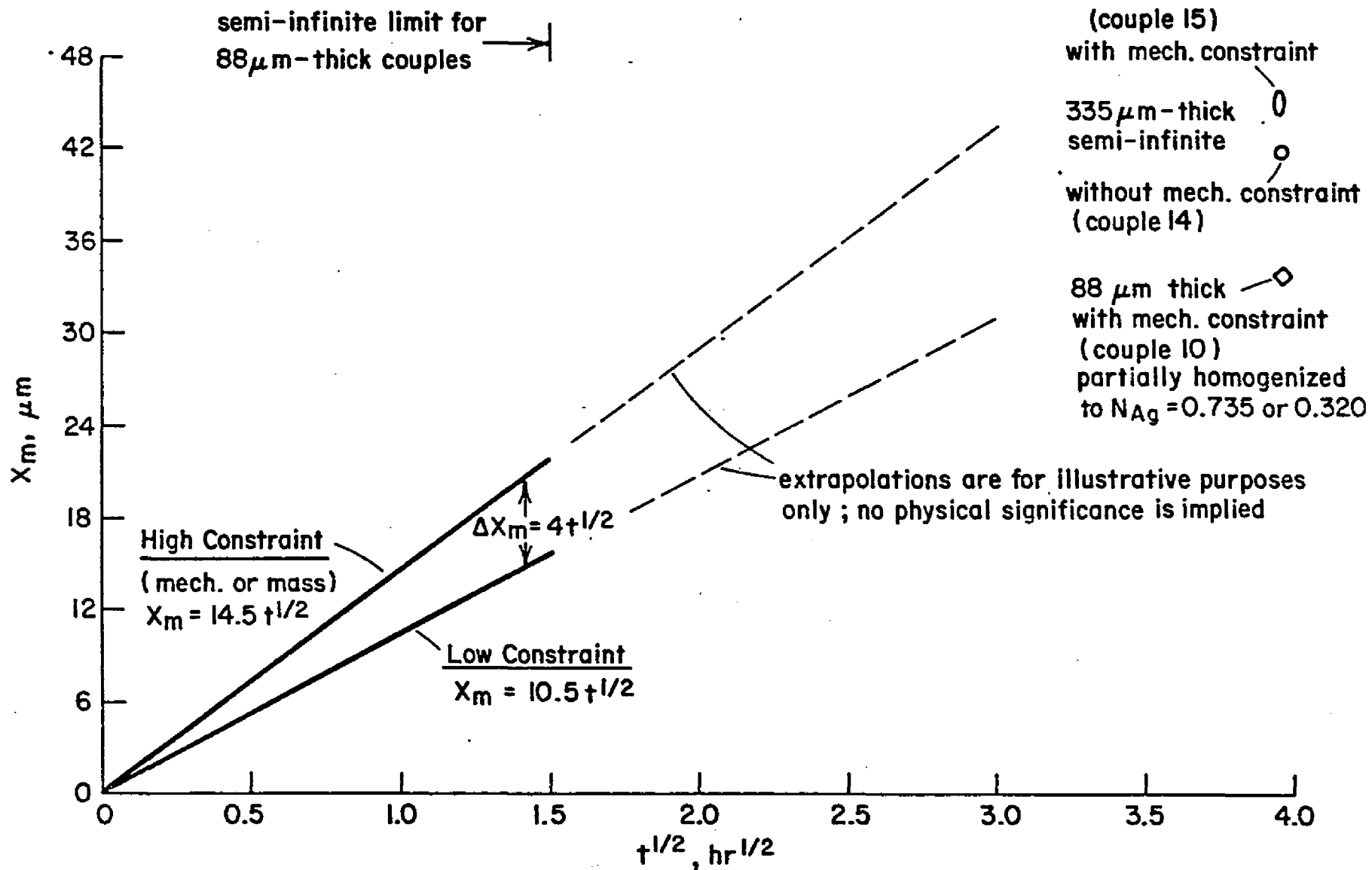


Fig. 31. Summary of marker shifting in Ag/Au couples diffused at 750°C.

a couple already having a large mass constraint has little or no effect on marker shifting in substantially-diffused couples. If one uses the (dashed) extrapolations in Fig. 31 as a guide,* one sees that \bar{X}_m for either of these two high-constraint couples is less than predicted by the shorter-time (≈ 2 hr), high-constraint curves. In fact, the longer-time, high-constraint couples have marker shifts more comparable to those extrapolated from the short-time, low-constraint couples. This indicates that the rate of marker shifting enhancement given by Eqn. 6(c) was not sustained beyond the early diffusion period. A possible reason for this will be offered later.

The marker position of the partially-homogenized, mechanically-constrained 88 μm -thick couple 10 shows that marker velocity decreased during homogenization, as one would expect from the ever-decreasing rate of interdiffusion during homogenization.

While marker shifting in bulky couples is well-known to be parabolic,^{2,3,6,28,53} no meaningful comparisons to the marker shifts observed here were found in the literature. Nor is the enhancement effect reported elsewhere. Markers were usually distributed between the original join and the porosity zone, and were often found within the porosity zone. Locating markers was often complicated by their close proximity to pores. In the more porous couples, conventional metallographic polishing would often artificially enlarge pores until nearby markers were dislodged. This problem was avoided in many

*Because of the lack of intermediate marker data, the extrapolations in Fig. 31 are obviously not justified. They are included solely to illustrate the relative marker positions.

couples by employing very minimal polishing times to prevent porosity enlargement, as illustrated in Fig. 32. Polishing time was much less critical in couples having little porosity, as seen in Fig. 33(a). Couple 5, mentioned above as suffering from porosity-entrapment of markers, featured more interdiffusion and more porosity than those couples in Fig. 32 and 33(a). In couple 5, a large number of the more-advanced markers which could not be located by light microscopy (despite various metallographic preparations) were finally found by the electron microprobe to be entrapped pores. A marker immediately adjacent to the porosity in couple 5 is shown in Fig. 33(b). It will be seen later that porosity-entrapment of markers is related to the growth and shifting of porosity.

Analyses of Marker Shifting and Couple Bending

The following analyses of marker shifting and couple bending employ phenomena introduced earlier, namely, the accommodation of mass flow by dislocation climb (mass flow/dislocation climb) and diffusion-induced stresses related to nonequilibrium vacancy concentrations. The first analysis is limited to the role of mass flow/dislocation climb in both marker shifting and couple bending. Its results fail to describe adequately the observed bending behavior. The second, more successful, approach is a stress analysis based on nonequilibrium vacancy concentrations generated during diffusion; the stress analysis is related directly to couple bending only.

Introduction to the Hypothetical Models of Mass Flow/Dislocation

Climb:

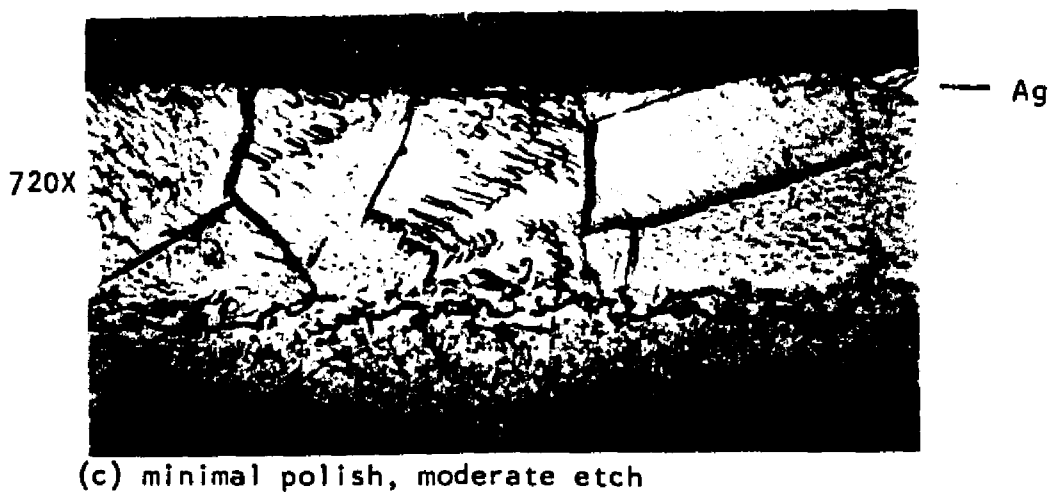
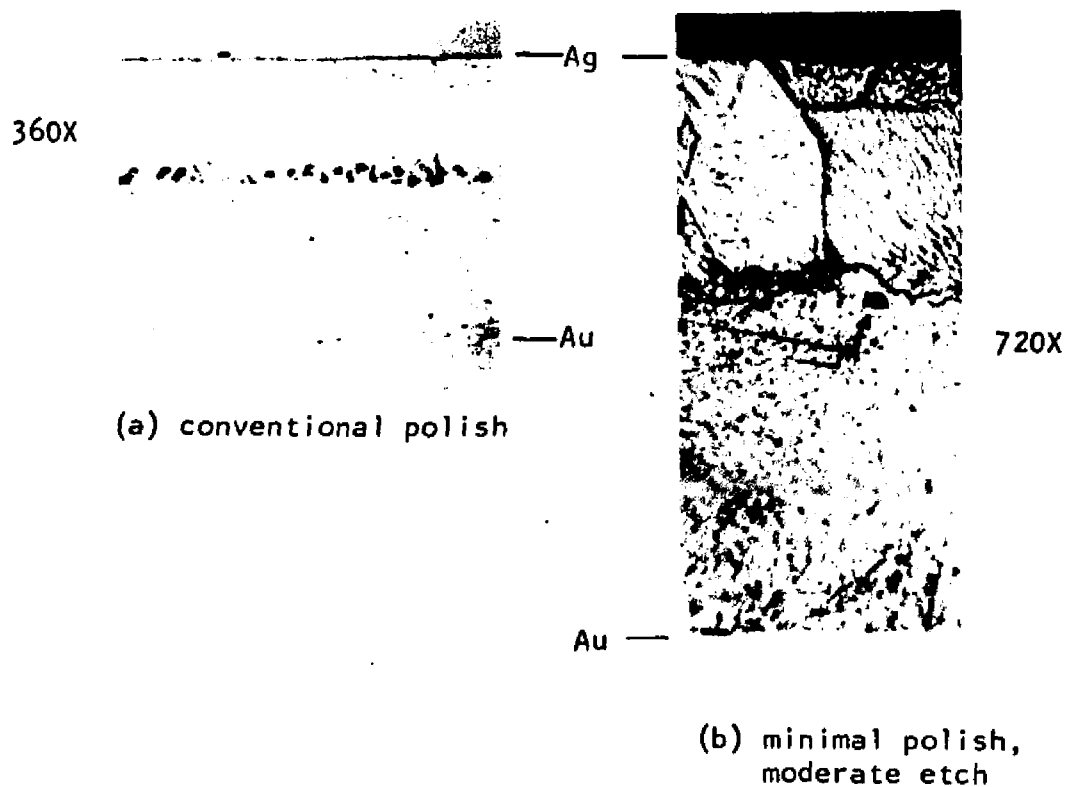


Fig. 32. Markers in the couple $88 \mu\text{m}/ 750^{\circ}\text{C}/ 0.52 \text{ hr}$. Some markers are dislodged or difficult to locate in the enlarged porosity of the conventional-polish surface in (a), but minimal polishing and moderate etching reveals marker particles, *m*, in (b) and (c). A seepage stain artifact, *s*, is shown in (c).

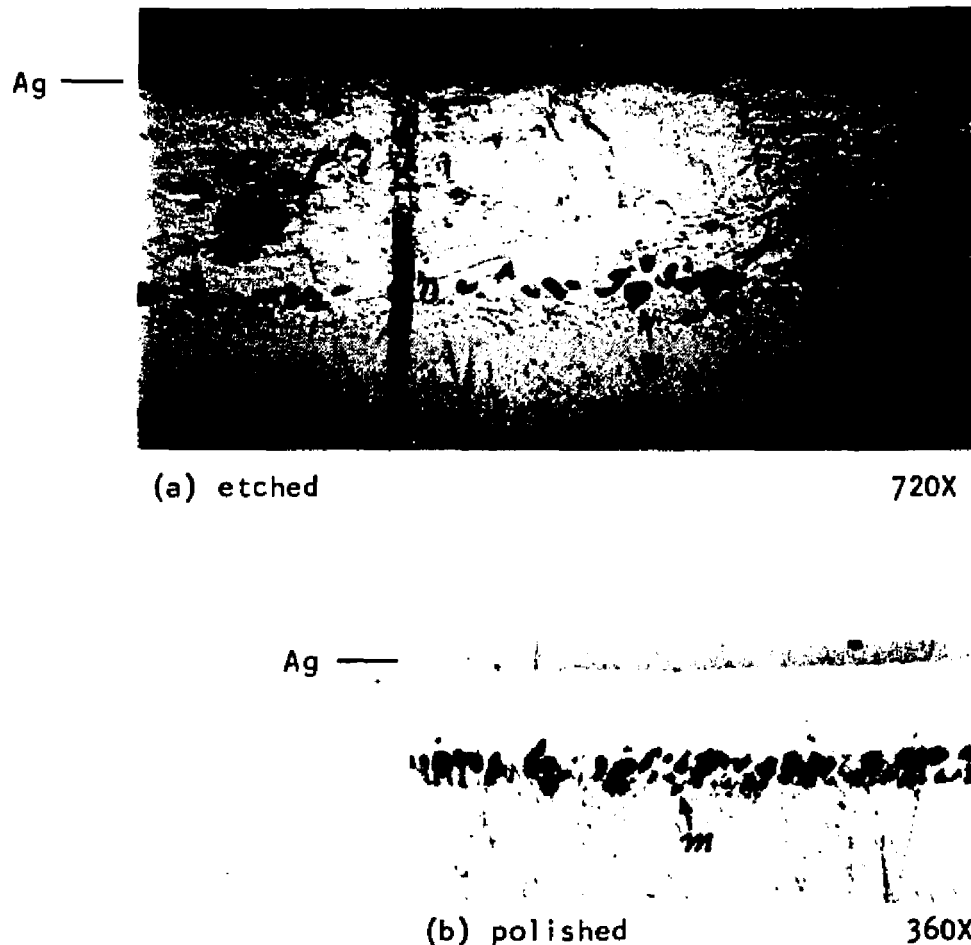


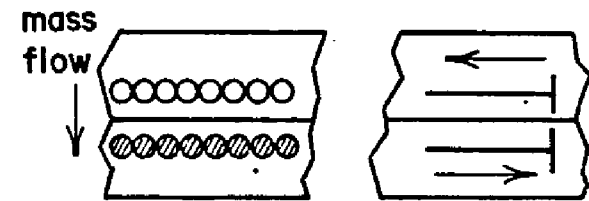
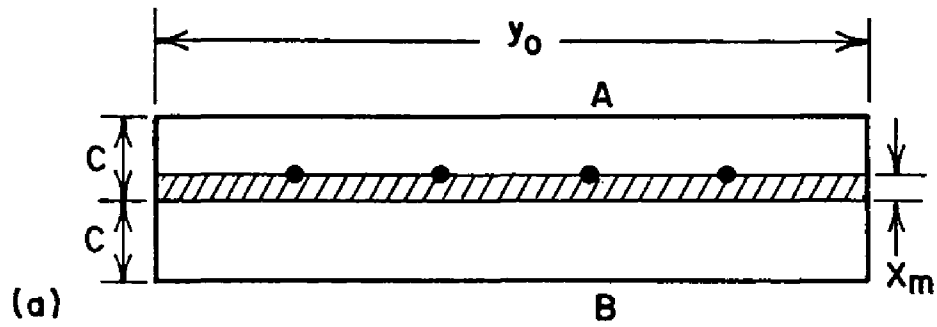
Fig. 33. Markers in couples having different amounts of porosity.

(a) Markers, *m*, are readily detected in the low-porosity couple 88 μm , mech. constraint/ 750°C/ 0.70 hr. A ghost trail from the electron microprobe beam is left of center. An elliptical SiC grinding particle is embedded in the matrix to the right of the markers.

(b) Several markers more advanced than the one indicated were entrapped in the pores of this couple 88 μm / 750°C/ 1.98 hr. Focussing on the marker results in poor focus of the pores, the pores being depressions and the oxide markers being in elevated relief.

Da Silva and Mehl,³ Darken,³⁰ and Barnes⁶ suggested that marker shifting in bulky couples should be a direct measure of the amount of mass flow which occurred during diffusion. As pointed out by Bardeen and Herring,⁷ the existence of marker shifting, plus the general lack of dimensional changes parallel to the diffusion flow in bulky couples having little porosity, indicate that mass flow occurs by the creation or destruction of atoms along planes which are preferentially aligned perpendicular to the diffusion flow. This was believed accomplished by dislocation climb under the osmotic forces created by vacancy supersaturation (or undersaturation) of 1%.^{7,63} If these arguments are extended to a hypothetical case where all mass flow is accommodated solely by dislocation climb perpendicular to the diffusion flow, it is seen in Fig. 34(a) that marker shifting should be a direct and complete measure of mass flow.* Incorporated in the marker shifting model (Fig. 34(a)) is an expansion of one side of the couple as dislocations operate as vacancy sources to accommodate a net gain of mass, and a contraction of the opposite side where dislocations operate as vacancy sinks to accommodate a net loss of mass. In accordance with others,^{3,6-8,10,12} it is assumed that mass relaxation is essentially uninhibited in the direction of diffusion flow during these expansion and contraction processes. Contrary to the above considerations, dislocation climb is not necessarily restricted to being perpendicular to the diffusion flow. Climb parallel to the diffusion flow is

*The climb depicted in Fig. 34 is oversimplified. It is more likely that the climb occurs by regenerative dislocation sources, such as the dislocation rings described by Bardeen and Herring.^{7,63}



$$D_A > D_B$$

○○○ net mass loss

●●● net mass gain

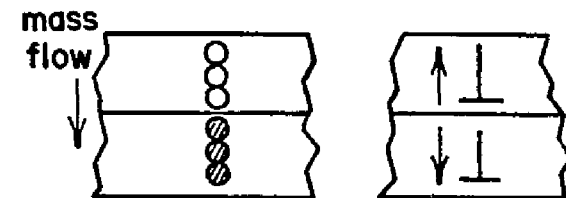
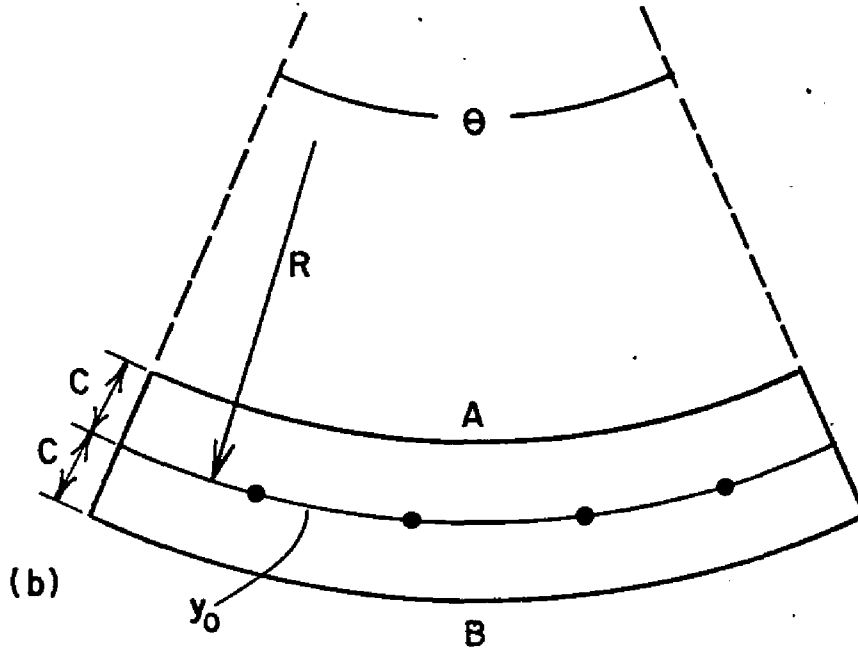


Fig. 34. Hypothetical models of marker shifting (a) or couple bending (b), both via mass flow / dislocation climb.

also possible. Liu and Powell²⁷ suggested that this mode of climb, while accommodating mass flow, could contribute to couple bending without causing marker shifting. This is shown in Fig. 34(b). Realistically, one would expect that dislocations would be oriented in the matrix such that climb would occur both parallel and perpendicular to the diffusion flow. In this case, marker shifting and bending would co-exist in a given couple. (Such behavior was observed in our low-mass constraint, 88 μm -thick couples, although not necessarily for the reason just described). Since the amount of mass flow is fixed by diffusion kinetics,* the dislocation climb models (Fig. 34) require that an increase in marker shifting can occur only at the expense of decreased couple bending, and vice versa. This constitutes a trade-off situation between marker shifting and couple bending. Based on this, we wish to determine the relative amounts of mass flow partitioned into components responsible for either marker shifting or couple bending. This task is simplified if the A/B couples are assumed to have constant partial molal volumes of A and B throughout, no porosity, and constant cross section areas perpendicular to the diffusion flow. These are reasonable assumptions for the Ag/Au couples. Volume changes during Ag-Au alloying are very small (less than 0.7%),^{15,33-35} and the presence of porosity and small changes in cross section due to minor bulge and dent deformation were subsequently judged

*The amount of net mass which is transferred across the original join (mass flow) is fixed by the time-wise integration of the net flux. The net flux is given by the vector sum of the fluxes of the diffusing species, $\underline{J}_A + \underline{J}_B$, in this case.

to have insignificant affects on the results of the analysis. The above concepts of mass flow/dislocation climb will be employed next to describe, each in its turn, the individual cases of (1) pure marker shifting, (2) pure couple bending, and finally, (3) simultaneous marker shifting and couple bending.

The Hypothetical Model of Marker Shifting via Mass Flow/Dislocation Climb:

From Fig. 34(a) the volume of mass flow which occurs within a couple is given by the marker shift, X_m , multiplied by the area normal to the diffusion flow. For unit depth of the couple normal to the plane of the paper, the amount of mass flow is directly proportioned to the area

$$A_m = X_m Y_0 \quad \dots 7$$

This area will serve as a convenient measure of the amount of mass flow which is related to marker shifting, and will be compared subsequently with a counterpart area related to couple bending.

The Hypothetical Model of Couple Bending via Mass Flow/Dislocation Climb:

The area related to the amount of mass flow which is responsible for bending, A_b , is calculated from an "isolated free body" of the B-rich portion of the bent couple in Fig. 34(b).^{*} The expansion and bending of the B-rich portion is accompanied by the simultaneous

^{*}Simultaneously solving the following two expressions shows that the entire area of the bent couple in Fig. 34(b) is, as required by conservation of mass, equal to the area of its nonbent, as-welded parent.

$$2CY_0 = \frac{\theta}{2\pi} \left\{ \pi \left[(R+C)^2 - (R-C)^2 \right] \right\}, \quad \theta = Y_0/R$$

shrinkage and bending of the A-rich portion. Since the amount of mass flow responsible for these events is the same for both portions, only one of them is required to describe the bending situation. Also, examining the nonporous B-rich portion avoids errors due to porosity swelling. Proceeding, the area of B-rich portion at isothermal diffusion time t_1 , bending radius R_1 , and bending angle θ_1 , is

$$A_{b1}^B = \frac{\theta_1}{2\pi} \left\{ \pi \left[(R_1 + c)^2 - R_1^2 \right] \right\} \quad \dots 8(a)$$

, which reduces to

$$A_b^B = \frac{\theta_1}{2} (2R_1c + c^2) \quad \dots 8(b)$$

Similarly, the B-rich area at t_2 ($t_2 > t_1$, $R_2 < R_1$, $\theta_2 < \theta_1$) is

$$A_{b2}^B = \frac{\theta_2}{2} (2R_2c + c^2) \quad \dots 9$$

The area of mass flow associated with bending between times t_1 and t_2 is

$$A_b^B = A_{b2}^B - A_{b1}^B \quad \dots 10$$

Substituting Eqns. 8 and 9 into Eqn. 10 results in

$$A_b^B = \frac{\theta_2}{2} (2R_2c + c^2) - \frac{\theta_1}{2} (2R_1c + c^2) \quad \dots 11$$

Employing the geometrical relationships $\theta_1 = \frac{y_0}{R_1}$ and $\theta_2 = \frac{y_0}{R_2}$ in Eqn. 11 yields,

$$A_b^B = \frac{y_0 c^2}{2} \frac{(R_1 - R_2)}{R_1 R_2} \quad \dots 12$$

Setting $R_2 - R_1 = \Delta R$ and $R_1 = R$, and dropping the superscript, B, results in

$$\frac{\Delta A_b}{\Delta R} = -\frac{y_0 c^2}{2} \frac{1}{R(R+\Delta R)} \quad \dots 13$$

Employing $\frac{dA}{dR} \equiv \lim_{R \rightarrow 0} \left[\frac{\Delta A_b}{\Delta R} \right]$, Eqn. 13 becomes

$$\frac{dA}{dR} = -\frac{y_0 c^2}{2R^2} \quad \dots 14$$

Integrating Eqn. 14 according to

$$\int_{A_0}^A dA = -\frac{c y_0^2}{2} \int_{R_0}^R \frac{dR}{R^2}$$

yields

$$A - A_0 = \frac{y_0 c^2}{2} \left(\frac{1}{R} - \frac{1}{R_0} \right) \quad \dots 15$$

, where A_0, A = area of the B-rich portion of the couple before and after diffusion-induced bending, respectively.

c, y_0 = initial thickness and width, respectively, of each couple half.

R_0, R = radius of curvature of the couple before and after diffusion, respectively.

Since $R_0 = \infty$ and letting $A - A_0 = A_b$, Eqn. 15 reduces to

$$A_b = \frac{y_0 c^2}{2R} \quad \dots 16$$

, where A_b = area representing the amount of mass flow across the original join which is associated with couple bending, R , during diffusion time t .

For the sake of introductory simplicity, marker shifting and couple bending were treated above as independent phenomena. Because both

were found experimentally to co-exist in the 88 μm -thick couples, the following model considers simultaneous marker shifting and couple bending.

The Hypothetical Model of Simultaneous Marker Shifting and Couple Bending via Mass Flow/Diallocation Climb:

A couple displaying simultaneous marker shifting and couple bending is shown in Fig. 35. Using a method similar to the preceding case of bending, but simplified for brevity, the area representative of mass flow across the original join in

$$A_{m,b} = A^B - A_O^B \quad \dots 17$$

, where A^B = area of the B-rich portion of the couple after marker shifting and couple bending has occurred (the marker-swept area is included).

$$A_O^B = Cy_O, \text{ the area of the B portion before diffusion.}$$

From Fig. 35,

$$A^B = \frac{\theta}{2\pi} \left\{ \pi \left[(R + C)^2 - (R - X_m)^2 \right] \right\} \quad \dots 18$$

Employing $\theta = \frac{y_O}{R}$ in Eqn. 18 and substituting the result into Eqn. 17 yields,

$$A_{m,b} = y_O X_m \left(1 - \frac{X_m}{2R} \right) + \frac{y_O C^2}{2R} \quad \dots 19$$

The marker-swept area bounded by y_O and y_m in Fig. 35 is calculated independently to be

$$A_m^i = y_O X_m \left(1 - \frac{X_m}{2R} \right) \quad \dots 20$$

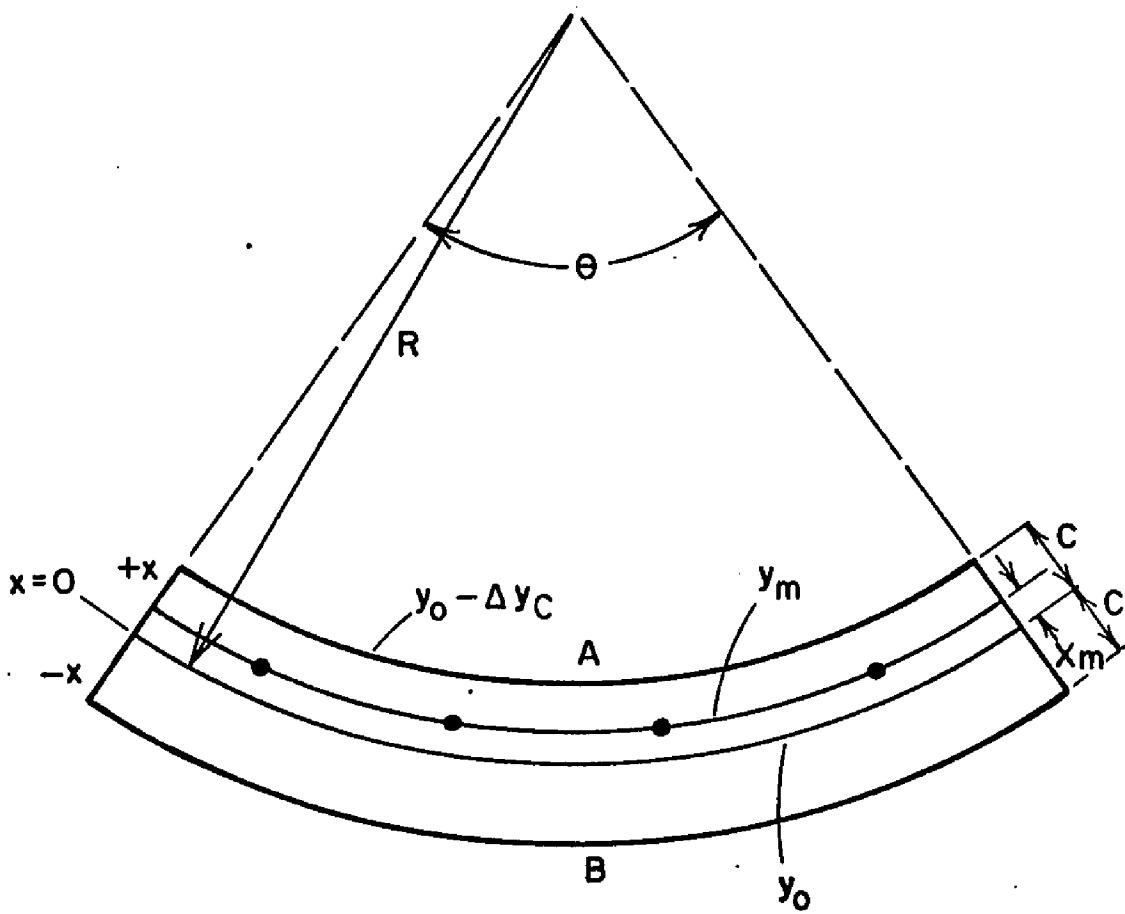


Fig. 35. Simultaneous marker shifting and couple bending.

Eqn. 20, which represents the area associated with marker shifting, is identical to the first term in the RHS of Eqn. 19. The factor $\frac{x_m}{2R}$ in either equation arises from the marker plane advancing into a region of ever-decreasing width, y , in the shrinking portion of the bending couple. The second term in the RHS of Eqn. 19 is identical to the bending-related area given by Eqn. 16. Thus, Eqn. 19 is comprised of a marker shifting term dependent on the bending radius, plus a couple bending term.

As $R \rightarrow \infty$, Eqn. 19 reduces to $y_0 x_m$, which is Eqn. 7 of the nonbent couple. Therefore, if bending is not accounted for when measuring the mass flow effects in a Kirkendall experiment, the result will be in error by the difference between Eqn. 19, which represents the actual mass flow, and Eqn. 7, which represents the mass flow in a presumably-nonbent couple. This error is expressed by using $A_{m,b}$ (Eqn. 19) as the correct measure of mass flow and A_m (Eqn. 7) as the usual, but possibly incorrect, measure. The relative error introduced by ignoring the mass flow associated with bending is then given by

$$A_{er} = \frac{A_{m,b} - A_m}{A_{m,b}} = \frac{y_0 x_m \left(1 - \frac{x_m}{2R}\right) + \frac{y_0 c^2}{2R} - y_0 x_m}{y_0 x_m \left(1 - \frac{x_m}{2R}\right) + \frac{y_0 c^2}{2R}}$$

which, for $2Rx_m \gg c^2 - x_m^2$,* reduces to

*This inequality holds true for all couples of this experiment and is expected to remain valid throughout semi-infinite diffusion in any bulky couple.

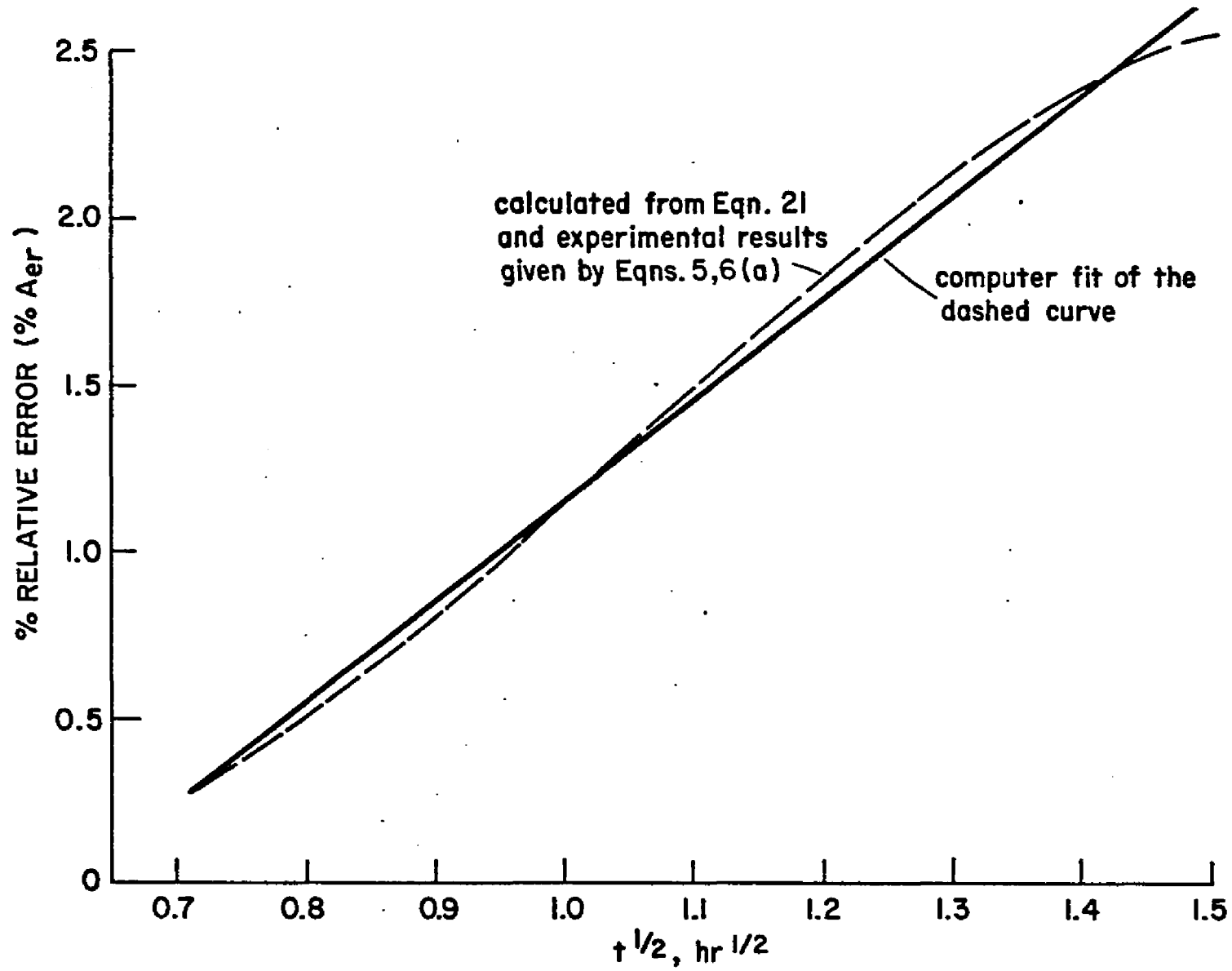


Fig. 36. Relative error in measuring mass flow when couple bending is ignored.

$$A_{er} \sim \frac{c^2 - x_m^2}{2RX_m} \quad \dots 21$$

A_{er} can be expressed in terms of diffusion time, $A_{er} = A(t)$, by employing marker shifting and couple bending results from the 88 μm -thick couples diffused at 750^oC, namely Eqns. 5 and 6(a). So doing yields the dashed curve in Fig. 36, which closely fits the (solid) parabolic curve given by

$$A_{er} \sim -0.0186 + 0.03 t^{\frac{1}{2}} \quad \dots 22$$

, where A_{er} is dimensionless and t is in hr.

From Fig. 36, it is seen that the relative error caused by ignoring bending increases as diffusion penetration increases, reaching a maximum of only $\sim 2\%$ at the semi-infinite diffusion limit.* As indicated earlier, this error likewise causes an error in X_m . One consequence of this error made in measuring the mass flow is that diffusion quantities calculated from it will accordingly be in error. For example, such an error could appear in Darken's⁵⁰ relationship between marker shifting and intrinsic diffusion coefficients given by

$$\frac{X_m}{2t} = (D_A - D_B) \frac{\partial N_A}{\partial x} \quad \dots 3$$

The term of interest, $D_A - D_B$, will appear erroneously-low if bending by mass flow/dislocation climb diminishes the value of X_m . However, the small ($\sim 2\%$) error in X_m caused by bending is not significant when

* A_{er} for thicker (170 and 335 μm) couples could not be likewise calculated because the very slight bending (very large R) of these couples could not be adequately measured by the technique employed here. However, results from the subsequent stress analysis indicate that any contribution to couple bending by dislocation climb would be less the thicker the couples. Therefore, the error, A_{er} , is expected to be larger in the 88 μm -thick couples analyzed here than it would be in thicker couples.

compared with experimental uncertainties of several percent encountered when measuring marker positions or diffusion coefficients, or those introduced by spurious marker displacements resulting from localized plastic deformation and, possibly, porosity-entrapment of markers.

If bending actually did occur by mass flow/dislocation climb (and this possibility has yet to be established), changes in the rate of marker shifting would be manifested by equivalent offsetting changes in couple bending, and vice versa. To see if this mass flow trade-off actually occurred, the area associated with simultaneous marker shifting and couple bending as given by Eqn. 19 is equated to its counterpart area associated with pure marker shifting, Eqn. 7. The result is the calculated marker shift enhancement

$$\Delta X_m = \frac{c^2 - x_m^2}{2R} \quad \dots 23$$

Solving Eqn. 23 by using the experimental results of marker shifting and couple bending, Eqns. 5 and 6(c), the calculated marker shift enhancement is found to increase parabolically with time, as seen at the bottom of Fig. 37. Since bending due to thermal expansion is also a contributing factor here, its effect is also indicated.* Its relative contribution to calculated marker shifting enhancement is minor for all but the shorter times, and is, therefore, ignored. The experimentally-observed enhancement of marker shifting is included in Fig. 37 for comparative purposes. It is obvious from Fig. 37 that marker shifting enhancement calculated from the model is quite insuffi-

*The actual calculation of the thermal expansion bending radius is given in Appendix A. Its equivalent contribution to ΔX_m was obtained by using Eqn. 23.

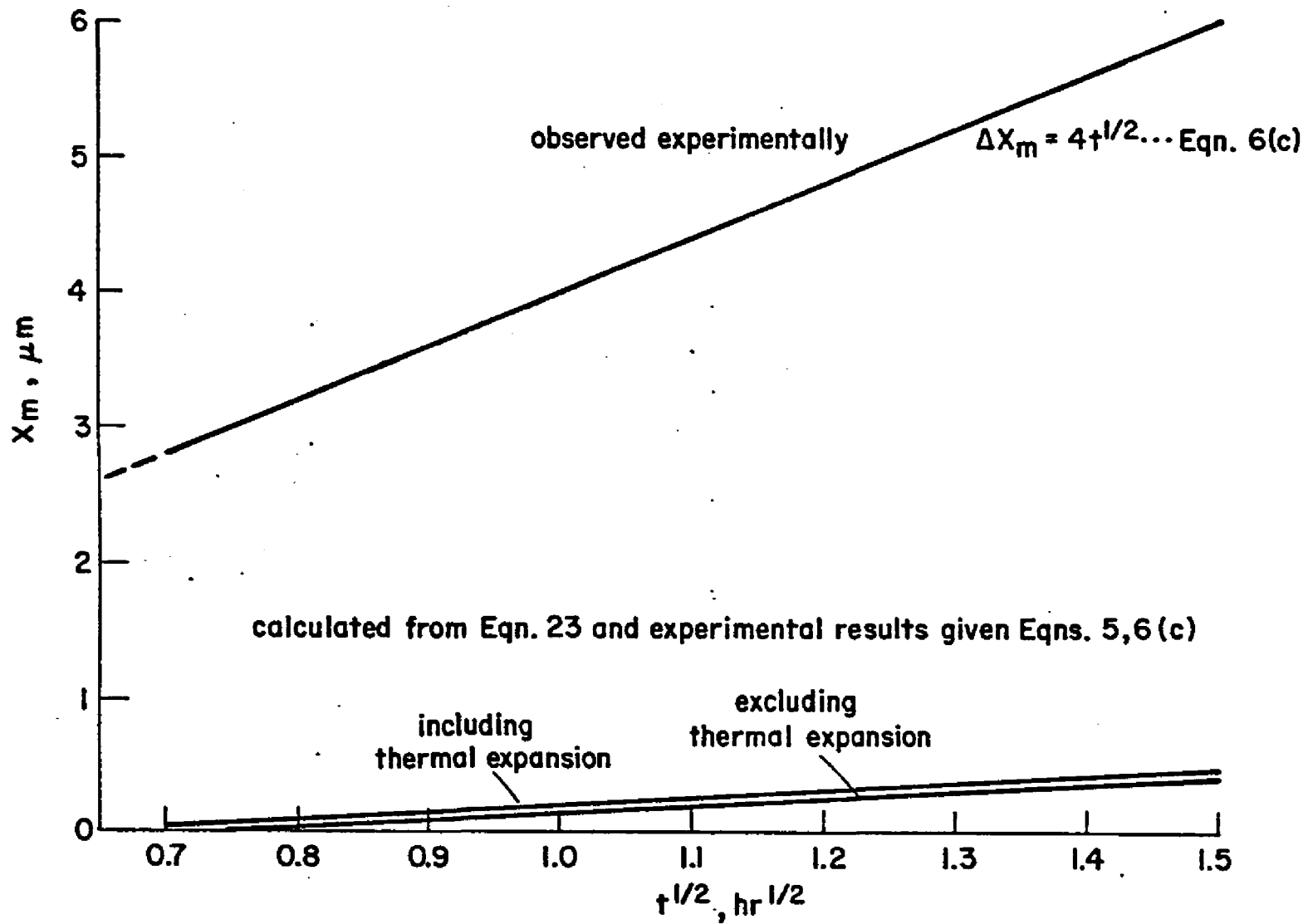


Fig.37. Comparing the observed and calculated values of enhanced marker shifting.

cient to account for the experimentally-observed enhancement in the nonbending, constrained couples, the calculated values of ΔX_m being more than an order of magnitude too small. (Likewise, solving Eqn. 23 for R by employing the experimental results of ΔX_m and X_m yields values of R which are more than an order of magnitude too large.) However, both the experimental and calculated marker shifting enhancements in Fig. 37 do increase parabolically with time. These results indicate that while the mass flow/dislocation model may be valid in part, it falls far short of adequately describing the simultaneous marker shifting and couple bending observed in thin-sheet Ag/Au couples.

There are additional, and very significant, shortcomings of the mass flow/dislocation climb model with regard to bending. Firstly, since mass flow is restricted to the interdiffusion zone, it fails to account for bending of the outer, nondiffused portions of the semi-infinite couples. This consideration does not pertain to bent couples observed by others^{6,16,27} because their diffusion anneals indicate that partial homogenization eliminated the nondiffused material. Secondly, the model cannot explain why couples of moderate mass constraint ($\sim 170 \mu\text{m}$) did not bend measurably when diffused at 750°C but did bend significantly when comparable amounts of interdiffusion were obtained at 850°C . Since interdiffusion and the resultant mass flow were comparable at either temperature, bending would have been comparable if mass flow/dislocation climb was primarily responsible for bending. Thirdly, mass flow arguments do not explain the unbending observed during advanced homogenization of couples which had been

severely bent earlier in diffusion. Answers to the above considerations are given by the stress analysis presented below.

Simplified Bending Stress Analysis*

An expression is derived to describe the strain rate at the terminal surfaces of bending couples. It will then be shown that the deviation of the vacancy concentration from the equilibrium value appropriate to each point of the diffusion zone produces throughout the entire couple a stress distribution which would cause the couple to bend in the observed manner. These stresses can attain magnitudes which are sufficient to deform plastically the thin (88 μm thick) couples.

The analysis is begun by geometrically describing the couple in Fig. 35 according to

$$y_0 = R\theta \quad \dots 24(a)$$

and

$$y_0 - \Delta y_c = (R - c)\theta \quad \dots 24(b)$$

Eliminating θ from the above expressions yields

$$\frac{R - c}{R} = \frac{y_0 - \Delta y_c}{y_0} = 1 - \epsilon_c \quad \dots 24(c)$$

, where $\epsilon_c =$ strain at the terminal surface of the couple $= \Delta y_c / y_0$.

From Eqn. 24(c),

$$\epsilon_c = \frac{c}{R} \quad \dots 25$$

*The stress analysis was originated by Professor G. W. Powell, The Ohio State University, 1971.

Differentiating with respect to (diffusion) time and rearranging terms yields

$$\dot{\epsilon}_C = -C \frac{\dot{R}}{R^2} \quad \dots 26$$

Having related strain to the rate of couple bending via Eqn. 26, we consider next the generation of such strains by the stresses generated from the elimination of nonequilibrium vacancy concentrations which form during diffusion.

First, an expression of the nonequilibrium vacancy concentration is derived from diffusion kinetics. In so doing, it is assumed that the distribution of Ag (or Au) in the couple is given by the Grube equation

$$N_{Ag} = \frac{1}{2} [1 + \text{erf}(q)] \quad \dots 29$$

, where N = mole fraction,

$$\text{erf}(q) = \frac{2}{\pi^{1/2}} \int_0^q \exp(-q^2) dq$$

$$q = x/(4Dt)^{1/2}$$

For the net flux given by

$$J_{Ag} + J_{Au} + J_v = 0 \quad \dots 30$$

, Fick's second law for vacancies may be written as

$$\frac{\partial N_v}{\partial t} = -\frac{\partial}{\partial x}(J_v) = \frac{\partial}{\partial x}(J_{Ag} + J_{Au}) \quad \dots 31(a)$$

$$\frac{\partial N_v}{\partial t} = \frac{\partial}{\partial x} \left[-D_{Ag} \frac{\partial N_{Ag}}{\partial x} - D_{Au} \frac{\partial N_{Au}}{\partial x} \right] \quad \dots 31(b)$$

Assuming D independent of composition and letting $\frac{\partial N_{Ag}}{\partial x} = -\frac{\partial N_{Au}}{\partial x}$,

$$\frac{\partial N_v}{\partial t} = - (D_{Ag} - D_{Au}) \frac{\partial^2 N_{Ag}}{\partial x^2} \quad \dots 32$$

From Eqn. 29

$$\frac{\partial^2 N_{Ag}}{\partial x^2} = - \frac{2x \exp(-x^2/4Dt)}{\pi^{1/2} (4Dt)^{3/2}} \quad \dots 33$$

It will be assumed that the deviation of the vacancy concentration from the equilibrium value, ΔN_v , is proportional to $-\partial^2 N_{Ag}/\partial x^2$.^{*} Therefore,

$$\Delta N_v = K \left[\frac{2x \exp(-x^2/4Dt)}{\pi^{1/2} (4Dt)^{3/2}} \right] \quad \dots 34(a)$$

or

$$\Delta N_v = \frac{K_0 x \exp(-x^2/4Dt)}{(4Dt)^{3/2}} \quad \dots 34(b)$$

Now, three-dimensional lattice straining in the diffusion zone results from the contraction or dilatation associated with the elimination of nonequilibrium concentration of vacancies, ΔN_v . These strains are assumed free to relax in a direction parallel to the diffusion flow, whereas such relaxation in a direction normal to the flow is restrained by the mass inertia of the couple. In order to maintain a non-bent couple in the presence of these unrelaxed strains, it is necessary to impose an oppositely-directed restraining stress at the diffusion zone. The magnitude of this restraining stress is dependent on ΔN_v in the following manner.

^{*}This can be rationalized by observing that $\partial^2 N_{Ag}/\partial x^2$ is a measure of the rate at which vacancies are being created or destroyed, as seen in Eqn. 32. This phenomenological viewpoint is illustrated in Shewmon. 102

Imagine a row of atoms, normal to the direction of diffusion flow, along which the vacancy concentration is changed from N_V to $N_V + \Delta N_V$ by diffusion. Before diffusion, this string of n_0 lattice sites consists of $N_V n_0$ vacancies and $(1 - N_V)n_0$ atoms. Subsequent diffusion alters the number of lattice sites from n_0 to n by either creating or destroying vacancies along the row (ΔN_V). The number of atoms is then given by $[1 - (N_V + \Delta N_V)] n$. Equating the number of atoms in the row gives $[1 - (N_V + \Delta N_V)] n = (1 - N_V)n_0$, or

$$n = \frac{(1 - N_V)n_0}{1 - N_V - \Delta N_V}$$

By calculating the engineering strain along the lattice sites, which are assumed separated by a constant distance of δ , we obtain the strain normal to the diffusion flow,

$$\epsilon_y = \frac{n\delta - n_0\delta}{n_0\delta} = \frac{N_V}{1 - N_V - \Delta N_V}$$

For $N_V, \Delta N_V \ll 1$

$$\epsilon_y \sim \Delta N_V^*$$

... 35

*The above expression is obtained by assuming that (1) all lattice sites, whether occupied by atoms or vacancies, are separated by a constant distance, and (2) the creation (or destruction) of a vacancy from the equilibrium value results in the creation (or destruction) of a lattice site along a plane perpendicular to diffusion flow. While it is beyond the scope of this text to refine the above approximation of strain due to nonequilibrium vacancy concentration, such a refinement might begin by considering, in an approximate manner, (1) inter-lattice spacing distortion due to localized accommodation around a vacancy or interstitial, and (2) creating or destroying a vacancy without necessarily creating or destroying a lattice site. This latter feature, (2), permits supersaturation or undersaturation of vacancies by replacing an atom with a vacancy or vice versa without altering the number of lattice sites, such as in the very beginning of Kirken-

(continued---)

Therefore, the restraining stress which must be applied to the regions of the diffusion zone to counteract the strain along y due to a change in the vacancy concentration is given by

$$\sigma_y = E \epsilon_y = E \Delta N_v \quad \dots 36$$

Thus, from Eqns. 34(b) and 36,

$$\sigma_y = \frac{EK_0 \times \exp(-x^2/4Dt)}{(4Dt)^{3/2}} \quad \dots 37$$

(---continued)

diffusion when the vacancy concentration is still near its equilibrium value. For the sake of a simplified argument, only the strain in the side of the couple gaining excess vacancies (the Ag-rich side, in this case) will be dealt with here. A similar approach with variations in detail should apply to the vacancy-deficient (Au-rich) side.

Let n_l = number of lattice sites along a row perpendicular to the diffusion direction.

$$\text{Then } n_l^o = n_a^o + n_v^o$$

$$\text{and } n_l^f = n_a^f + n_v^f$$

, where the superscripts o and f refer to before and after diffusion, respectively, and the subscripts a and v refer to atoms and vacancies, respectively. It is known that atoms surrounding a vacancy tend to relax elastically into the vacancy site, i.e., the effective lattice space occupied by a vacancy is less than that of a matrix atom. If the interatomic spacing is δ , then let the space occupied by an inserted vacancy equal $\alpha \delta$, where $\alpha < 1$. (The value of α for Au-Ag might be calculated from the value of the volume contraction due to vacancies; see Fraikor and Hirth, 103) Then the length, l , of the lattice before and after diffusion is given by

$$l^o = \delta n_a^o + \alpha \delta n_v^o$$

$$l^f = \delta n_a^f + \alpha \delta n_v^f.$$

The engineering strain introduced by changing the vacancy concentration along the lattice row during diffusion is

$$\epsilon_y = \frac{l^f - l^o}{l^o} = \frac{(\delta n_a^f + \alpha \delta n_v^f) - (\delta n_a^o + \alpha \delta n_v^o)}{\delta n_a^o + \alpha \delta n_v^o}$$

(continued---)

σ_y yields a net stress of zero across the diffusion zone but it does produce a mechanical moment. Therefore, a counteracting moment must be exerted on the diffusion couple. Thus**

$$\sigma'' = \frac{\sigma x}{c} \quad \dots 38$$

, where c = halfthickness of the diffusion couple and the stress direction is normal to x . For the moment of forces distributed over the couple equal to zero,

$$\int_{-c}^{+c} \frac{\sigma x^2 dx}{c} + \int_{-c}^{+c} \frac{EK_0 x^2 \exp(-x^2/4Dt) dx}{(4Dt)^{3/2}} = 0 \quad \dots 39$$

or

(---continued)

$$\epsilon_y = \frac{(n_a^f - n_a^0) + \alpha (n_v^f - n_v^0)}{n_a^0 + \alpha n_v^0} = \frac{\Delta n_a + \alpha \Delta n_v}{n_a^0 + \alpha n_v^0}$$

If only a fraction, f , of the annihilated atom sites are occupied by vacancies (the others $(1-f)$ having contributed directly to the destruction of lattice sites), then $\Delta n_v = -f \Delta n_a$.

Then

$$\epsilon_y = \frac{\Delta n_v (-1/f) + \alpha \Delta n_v}{n_a^0 + \alpha n_v^0} = \frac{\Delta n_v (\alpha - 1/f)}{n_a^0 + \alpha n_v^0}$$

Since $n_a^0 \sim n_v^0 \gg \Delta n_v$, and letting $\alpha' = \alpha - 1/f$

$$\epsilon_y \sim \alpha' \Delta n_v$$

This expression is similar to that given by Eqn. 35, except for the term α' . If α' = constant, it can be grouped with other constants, EK_0 , in the subsequent stress analysis. However, the value of the term f in the expression of α' is related to the efficiency of operating vacancy sinks and its value, constant or not, is not known.

**This treatment is analogous to a thermal stress analysis given by Timoshenko and Goodier.¹⁰⁴

$$\sigma'' = \frac{-3EK_0}{2C^3(4Dt)^{3/2}} \int_{-C}^{+C} x^2 [\exp(-x^2/4Dt)] dx \quad \dots 40$$

Solving yields

$$\sigma'' = \frac{-3EK_0 \times \exp(-C^2/4Dt)}{2C^3} \sum_{n=1}^{\infty} \frac{2^n (C^2/4Dt)^{\frac{2n+1}{2}}}{3 \cdot 5 \dots (2n+1)} \quad \dots 41$$

Therefore, the stress across the diffusion couple is given by the sum of σ_y (Eqn. 37) and σ'' (Eqn. 41), which is

$$\sigma = EK_0 \left[\frac{x \exp(-x^2/4Dt)}{(4Dt)^{3/2}} - \frac{3x \exp(-C^2/4Dt)}{2C^3} \sum_{n=1}^{\infty} \frac{2^n (C^2/4Dt)^{\frac{2n+1}{2}}}{3 \cdot 5 \dots (2n+1)} \right] \quad \dots 42$$

Eqn. 42 is rearranged in terms of the diffusion penetration factor, $C^2/4Dt$, to yield the stress parameter

$$\sigma \cdot \frac{1}{EK_0} = \frac{x}{C^3} \left\{ [\exp(-x^2/4Dt)] (C^2/4Dt)^{3/2} - \frac{3}{2} [\exp(-C^2/4Dt)] \sum_{n=1}^{\infty} \frac{2^n (C^2/4Dt)^{\frac{2n+1}{2}}}{(2n+1)!} \right\} \quad \dots 43$$

For a given D , C , and t (chemical diffusion coefficient, $= 1.54 \times 10^{-10}$ cm^2/sec ,³⁸ couple halfthickness, and diffusion time, respectively), the distribution of stress across a diffusion couple, $\sigma(x)$, is obtained from Eqn. 43.* Computer solutions of Eqn. 43 were obtained for a wide variety of couples representing different couple thicknesses and diffusion times. Times were established by assigning various values to $C^2/4Dt$, C being constant for a particular couple thickness.

*With the RHS dimensioned in cm-sec , the LHS (the stress parameter) is given in cm^{-2} . Note that σ/E is dimensionless.

Appendix C describes the computations. Stress distributions of three 88 μm -thick couples diffused at 750°C for times given by $C^2/4Dt = 4, 9,$ and 18 are plotted in Fig. 38. These stress distributions were selected because the onset of measurable bending occurs at $C^2/4Dt \sim 18$ ($t \sim 0.5\text{hr}$) and the semi-infinite diffusion time limit is reached at $C^2/4Dt \sim 4$ ($t \sim 2.2\text{hr}$).*

By inspection of Fig. 38, the maximum diffusion zone stress, σ_{max} , is seen to decrease and shift further from the original join ($x=0$) as diffusion time increases. Such behavior can be rationalized by noting that the concentration gradient which gives rise to chemical stresses becomes smaller and occupies more of the diffusion couple as diffusion proceeds.**

*These particular values are, of course, unique to the 88 μm -thick couples.

** σ_{max} can be obtained by differentiating Eqn. 42 such that $\partial\sigma/\partial x = 0$. So doing yields

$$\frac{\partial\sigma}{\partial x} = EK_0 \left\{ \frac{1}{(4Dt)^{3/2}} \left[\exp(-X_{\sigma_{\text{max}}}^2/4Dt) - \frac{2X_{\sigma_{\text{max}}}^2 \exp(-X_{\sigma_{\text{max}}}^2/4Dt)}{(4Dt)^{5/2}} \right. \right. \\ \left. \left. - \frac{3 \exp(-C^2/4Dt)}{2C^3} \sum_{n=1}^{\infty} \frac{2^n (C^2/4Dt)^{\frac{2n+1}{2}}}{3 \cdot 5 \cdots (2n+1)} \right] \right\} = 0.$$

Multiplying by $X_{\sigma_{\text{max}}}$ and rearranging terms yields

$$\frac{X_{\sigma_{\text{max}}} \exp(-X_{\sigma_{\text{max}}}^2/4Dt)}{(4Dt)^{3/2}} - \frac{3X_{\sigma_{\text{max}}} \exp(-C^2/4Dt)}{2C^3} \sum_{n=1}^{\infty} \frac{2^n (C^2/4Dt)^{\frac{2n+1}{2}}}{3 \cdot 5 \cdots (2n+1)} \\ = \frac{2X_{\sigma_{\text{max}}}^2 \exp(-X_{\sigma_{\text{max}}}^2/4Dt)}{(4Dt)^{5/2}}$$

By comparing with Eqn. 42, it is seen that

(continued---)

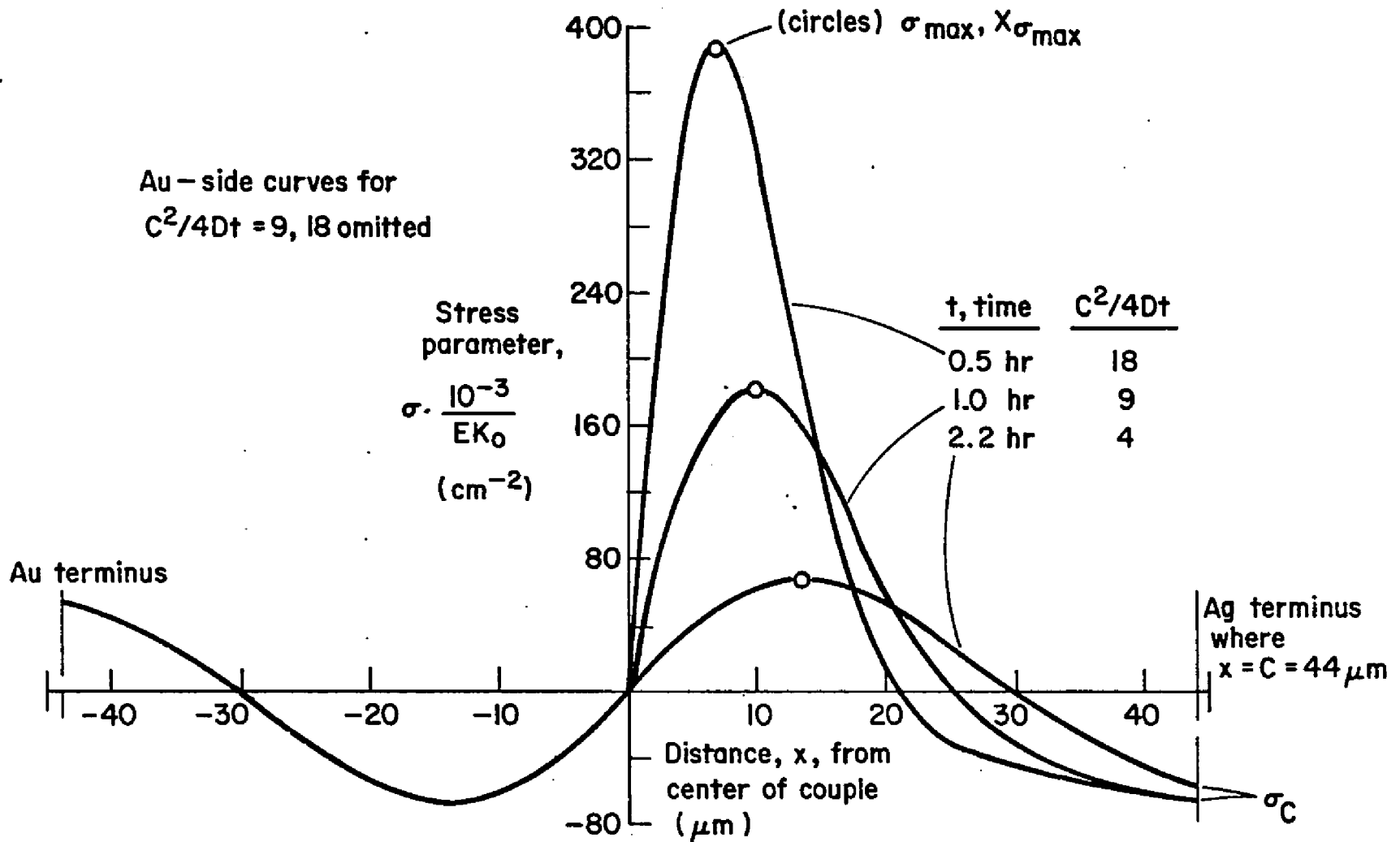


Fig. 38. The stress distribution across $88 \mu m$ -thick couples diffused at $750^\circ C$.

The stresses at the terminal ends of the couples, given by the calculated stress parameter σ_c , are responsible for plastic deformation bending of the outermost, nondiffused material of pure Ag or pure Au. The magnitude of σ_c is estimated next by comparing the bending strain rates to known steady-state creep strain rates ($\dot{\epsilon}$) of Au.* The expectation that creep kinetics might describe couple bending follows from the fact that bending occurs gradually at elevated temperatures, and the deformation effects observed for the couples (destruction of former grains, subgrain formation, grain boundary migration, and grain boundary sliding) are characteristic of creep deformation.¹⁰⁵ Appropriate creep data for Au are given by Sherby and Burke,¹⁰⁶ where their steady-state creep strain rate is given in the form of $\dot{\epsilon}L^2/D$, with L = grain diameter and D = diffusion coefficient. Modifying our bending strain rate expression, Eqn. 26, to conform to their format is done by multiplying both sides of Eqn. 26 by the constant L^2/D .

This yields

$$\dot{\epsilon}_c L^2/D = \frac{CL^2}{D} \left(-\frac{\dot{R}}{R^2} \right) \quad \dots 44$$

(---continued)

$$\sigma_{\max} = \frac{2EK_0 X_{\sigma_{\max}}^3 \exp(-X_{\sigma_{\max}}^2/4Dt)}{(4Dt)^{5/2}}$$

* It is assumed that couple bending is occurring in the steady-state range because $\dot{\epsilon}$ for the semi-infinite bending couples varies from 0.01 to 0.2 and Burton and Greenwood (Metal Sci. Jnl., 4, 1970, p.215) found that primary creep is always absent for $\dot{\epsilon} \gtrsim 1 \times 10^{-4}$ for pure Cu tested under a wide variety of low-stress high-temperature conditions. (Cu lies directly above Ag and Au in group 1B of the periodic table and has the same crystal structure, FCC, as Ag and Au; these similar features indicate that the creep behavior of Cu, Ag, and Au would likely be similar.¹⁰⁵)

For our purpose, $L = C = 0.044$ mm and D is calculated from the general Arrhenius expression of the self-diffusion coefficient of Au¹⁰⁷ to be 4.036×10^{-5} mm²/hr. Values of $-\frac{\dot{R}}{R^2}$ during bending of semi-infinite, 88 μ m-thick couples are obtained from our experimental results given by Eqn. 5. Employing these in Eqn. 44 yields for the bending couples $0.3 \approx \dot{\epsilon}_C L^2/D \approx 0.5$. From the Au creep curve of Sherby and Burke,¹⁰⁶ this corresponds to creep stresses which vary between 140 psi at $t = 0.5$ hr and 170 psi at $t = 2.2$ hr. This is clearly in the low-stress range. Thus, plastic deformation at the terminal ends of the couples is indicative of high-temperature, low-stress creep.

The calculated values of σ_C , shown in Fig. 39 reveal that the creep stress at $x = C$ is highest early in diffusion and decreases by about 15% as diffusion progresses to the semi-infinite limit. However, the preceding analysis which related couple bending to known creep behavior indicated the inverse situation of the stress increasing moderately (from 140 to 170 psi, or 20%) during the same time period. The σ_C calculations indicate that this increase in stress as diffusion progresses is physically unrealistic. It is concluded from this that while all values of bending stress at the couple terminal ends are in the range of low-stress creep, the kinetic details of bending by creep deformation are not described adequately by the limited amount of bending data obtained in this research.*

*Should a significant amount of accurate couple bending data be generated in a future experiment, especially for the very early stage of bending, additional creep stress information might be obtained from the steady-state creep relationship $\dot{\epsilon} = a\sigma^m$, where a and m are empiri-

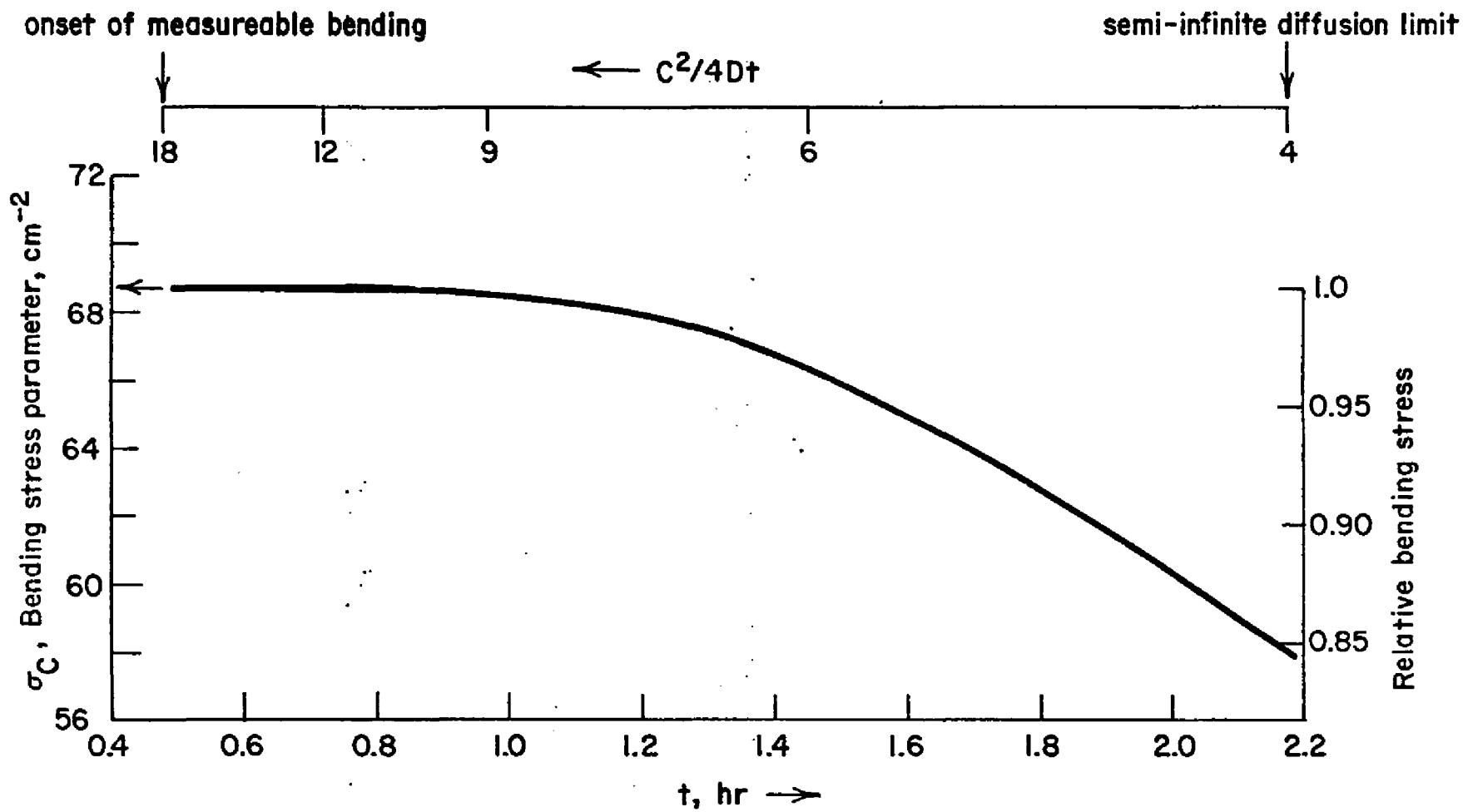


Fig. 39. Variation of stress with time at the end of $88\ \mu\text{m}$ -thick couples.

The maximum stress in the diffusion zone ($\bar{\sigma}_{\max}$) can be estimated for a given diffusion time. For a diffusion anneal of 0.5 hr, $c^2/4Dt = 18$ (the onset of measureable bending), stress calculations* show that $\frac{\bar{\sigma}_c}{\bar{\sigma}_{\max}} \sim 0.18$.** Since $\bar{\sigma}_c \sim 140$ psi, $\bar{\sigma}_{\max} \sim 780$ psi. In actual practice, the value of $\bar{\sigma}_{\max}$ will be limited by an engineering-type yield stress of the diffusion zone material. Therefore, calculated values of $\bar{\sigma}_{\max}$, such as given above, could be ficticiously high and may, in fact, be lower. Modifying the calculated stress distribution to account for the limit on $\bar{\sigma}_{\max}$ requires appropriate engineering stress data. Since such data is lacking, the stress distribution is left as is.

Results of the bending stress analysis can be used to explain the experimentally-observed bending. Most notable is the evidence that the primary factor controlling bending during the early period of diffusion is the stress distribution which arises as a result of non-equilibrium vacancy concentrations. This is indicated by the capability of the early-time (0.5 hr) stress distribution to induce creep deformation in the outer, nondiffused portion of the 88 μm -thick couple.

(---continued)

cal constants for metals and alloys, and m in a given system assumes integer values dependent on the stress level.¹⁰⁸⁻¹¹² Combining this creep expression with the bending expression, Eqn. 26, yields for creep at the couple ends ($x = C$)

$$\dot{R}/R^2 = \alpha \bar{\sigma}_c^m, \text{ where } \alpha = -a/C, \text{ an empirical constant}$$

In the early stage of diffusion and bending where $\bar{\sigma}_c$ is constant (see Fig. 39), the expression reduces to a reciprocal relationship between bending radius and diffusion time given by $R = k/t$. It was attempted to employ the bending data (\dot{R} , R^2) and calculated stresses ($\bar{\sigma}_c$) from this research in the above relationships, but the results indicated that the bending data were too few to yield meaningful information from this particular approach.

*Since the ratio $\bar{\sigma}_c/\bar{\sigma}_{\max}$ is continuously changing with time, the value calculated here is restricted to the particular diffusion time selected.

During this early period, the stresses in the diffusion zone are high (e.g., Fig. 38) and they inhibit the climb of dislocations parallel to the diffusion flow.⁸ This inhibits bending via the mass flow/dislocation climb mechanism. Therefore, the bending of the couple results simply from unconstrained plastic flow. However, for longer times, the stresses in the diffusion zone are much lower (Fig. 38); hence conditions are more favorable for dislocation-climb bending to operate. Even in this case, bending requires plastic flow of the regions of the couple outside the diffusion zone. Thus, the primary mode of bending is believed to be plastic flow of the couple by means of diffusion-induced stress, with only a minor bending contribution from the mass flow/dislocation climb mechanism.

It is believed that the mass-constrained couples (170 and 335 μm) did not bend measurably throughout 750°C diffusion because of insufficient bending stresses at the outer, nondiffused portions of these thicker couples. This is shown in Fig. 40, where stress distributions are plotted for three identically-diffused (~ 1.5 hr at 750°C) couples of different thicknesses, 88, 170, or 335 μm . The outermost bending stress, σ_c , is largest in the 88 μm -thick couple and decreases markedly with increasing couple thickness. This effect of mass constraint on σ_c is maintained when the couples described in Fig. 40 are further diffused to their respective semi-infinite limits. This is shown in Fig. 41.* The effect of couple thickness (mass constraint) on the

*Fig. 41 also shows that the family of stress distribution curves given by " $C^2/4Dt = \text{variable constant}$ " exhibits common roots given by the normalized positions $x_{\sigma_{\text{max}}}/C$ and $x_{\sigma=0}/C$.

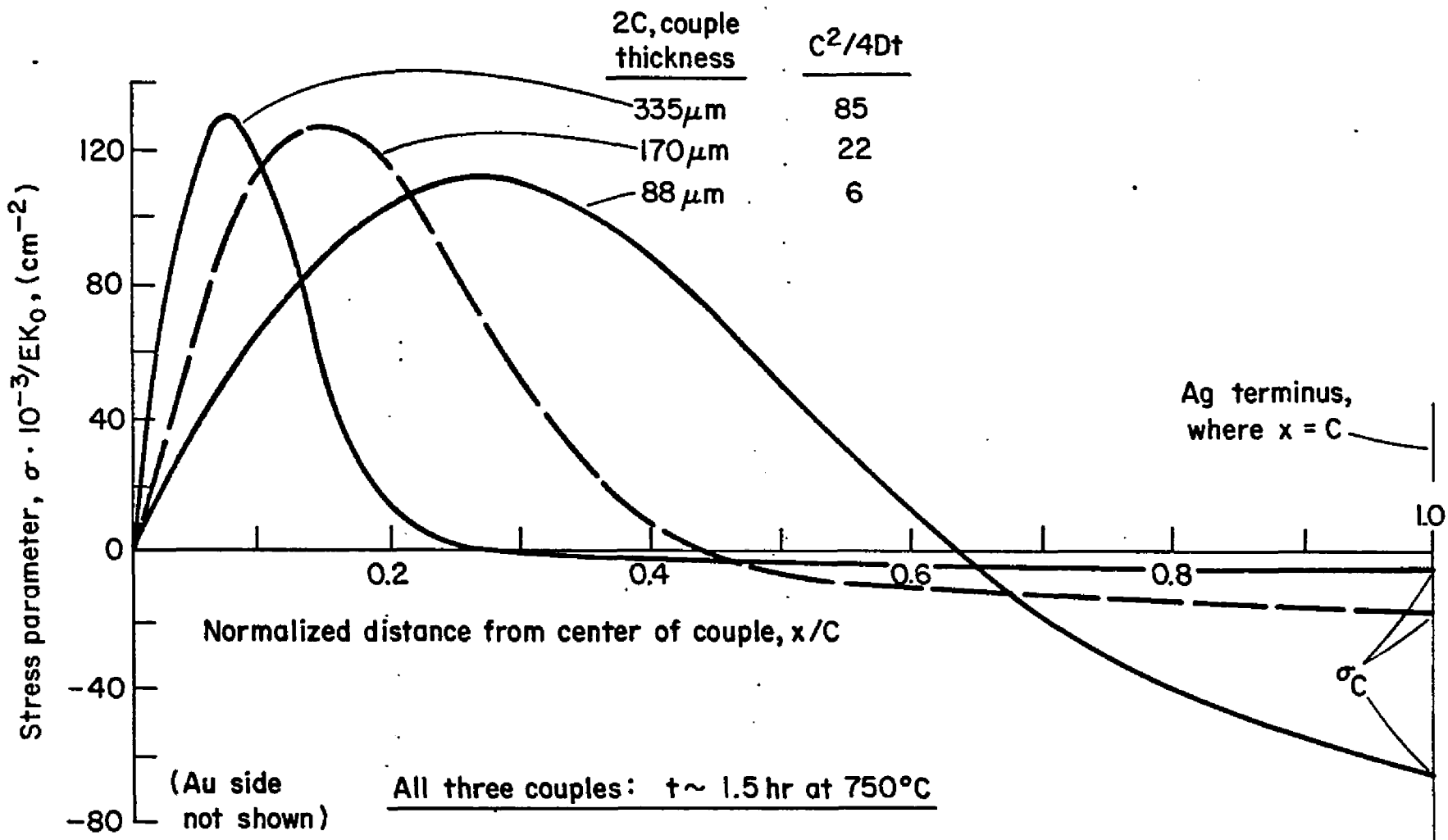


Fig. 40. Effect of couple thickness (mass constraint) on the stress distribution across identically-diffused couples.

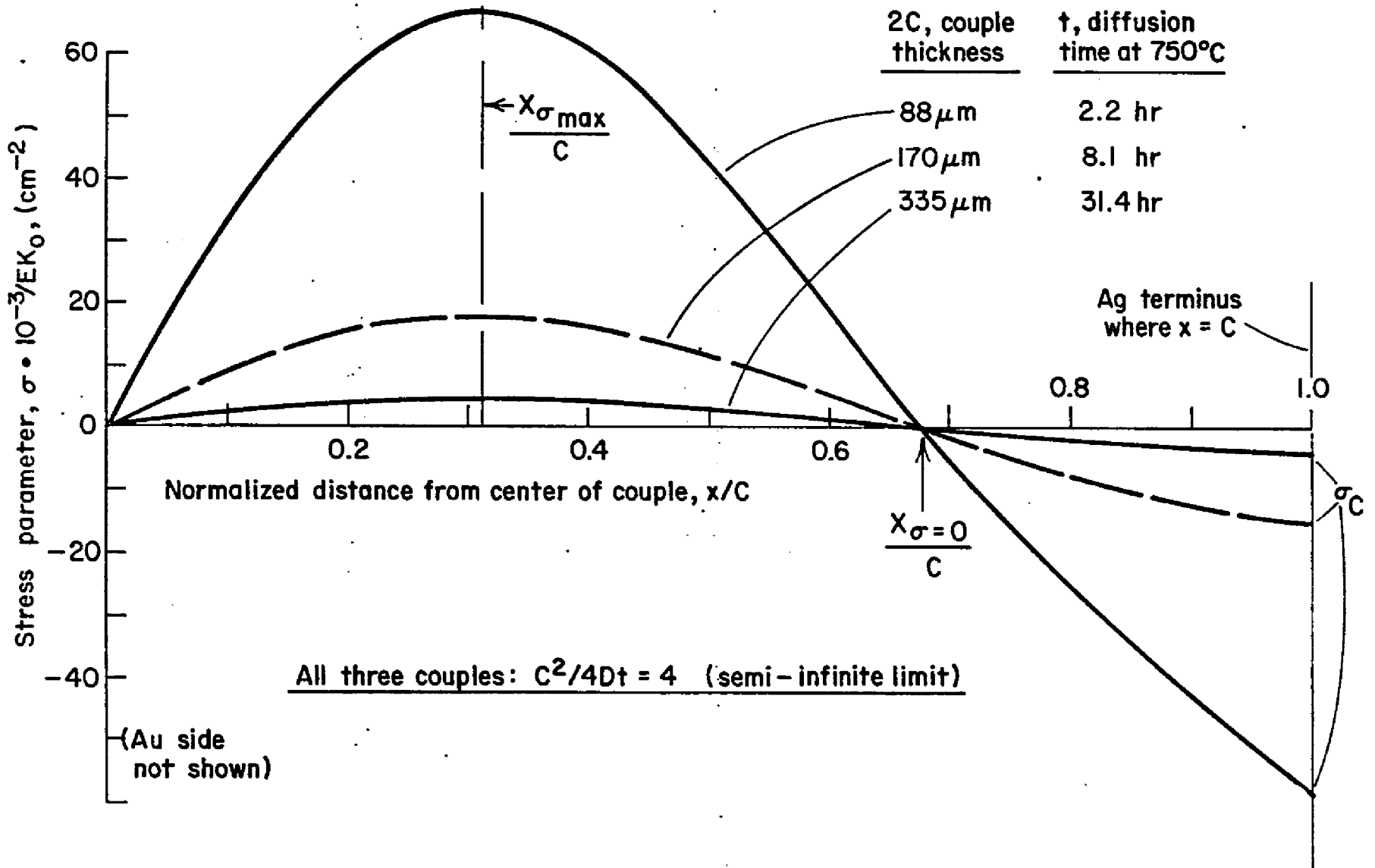


Fig. 4l. Effect of couple thickness (mass constraint) on the stress distribution of couples having the same fraction of interdiffusion.

bending stress is summarized in Fig. 42, where it is seen that

$\sigma_c \propto \frac{1}{c^2}$ * for semi-infinite couples having the same fraction of their thickness occupied by the interdiffusion zone, i.e., for couples having the same value of $c^2/4Dt$. It is evident from Fig. 42 that the extent of interdiffusion is much less influential on bending stress than is couple thickness. ($c^2/4Dt \sim 18$ corresponds to the diffusion zone occupying $\sim \frac{1}{2}$ of the couple thickness, whereas diffusion extends to the semi-infinite limit when $c^2/4Dt \sim 4$). To illustrate the effect of thickness, the creep strain rate during bending of the 88 μm -thick couples indicated in Fig. 42 is calculated from Eqns. 5 and 26 to be $\dot{\epsilon}_c \sim 1.7 \times 10^{-6} \text{ sec}^{-1}$ when $\sigma_c \sim 140 \text{ psi}$ and $c^2/4Dt = 18$. Employing the relationship $\sigma_c \propto \frac{1}{c^2}$ and the Au creep data used earlier,¹⁰⁶ the strain rate for the corresponding ($c^2/4Dt = 18$) 335 μm -thick couples in Fig. 42 is $\dot{\epsilon}_c \sim 2.7 \times 10^{-10} \text{ sec}^{-1}$. This is approximately four orders of magnitude smaller than the strain rate of the 88 μm -thick couple, thereby explaining the absence of detectable bending of the 335 μm -thick couples.

The increased propensity for the moderately thick couples ($\sim 170 \mu\text{m}$) to bend at the higher diffusion temperature of 850°C is probably caused by the decreased resistance to creep flow at higher temperatures.

The unbending of previously-bent couples indicates that the bending stresses at the outer portions of the couple change their sign in the advanced stages of homogenization, i.e., from compression to ten-

* This relationship can be obtained from the stress distribution expression (Eqn. 43) by setting $x = c$ and $c^2/4Dt = \text{variable constant}$, which reduces the expression to $\sigma_c = \frac{v'}{c^2}$, where $v' = \text{a constant given by } v' = (c^2/4Dt)$.

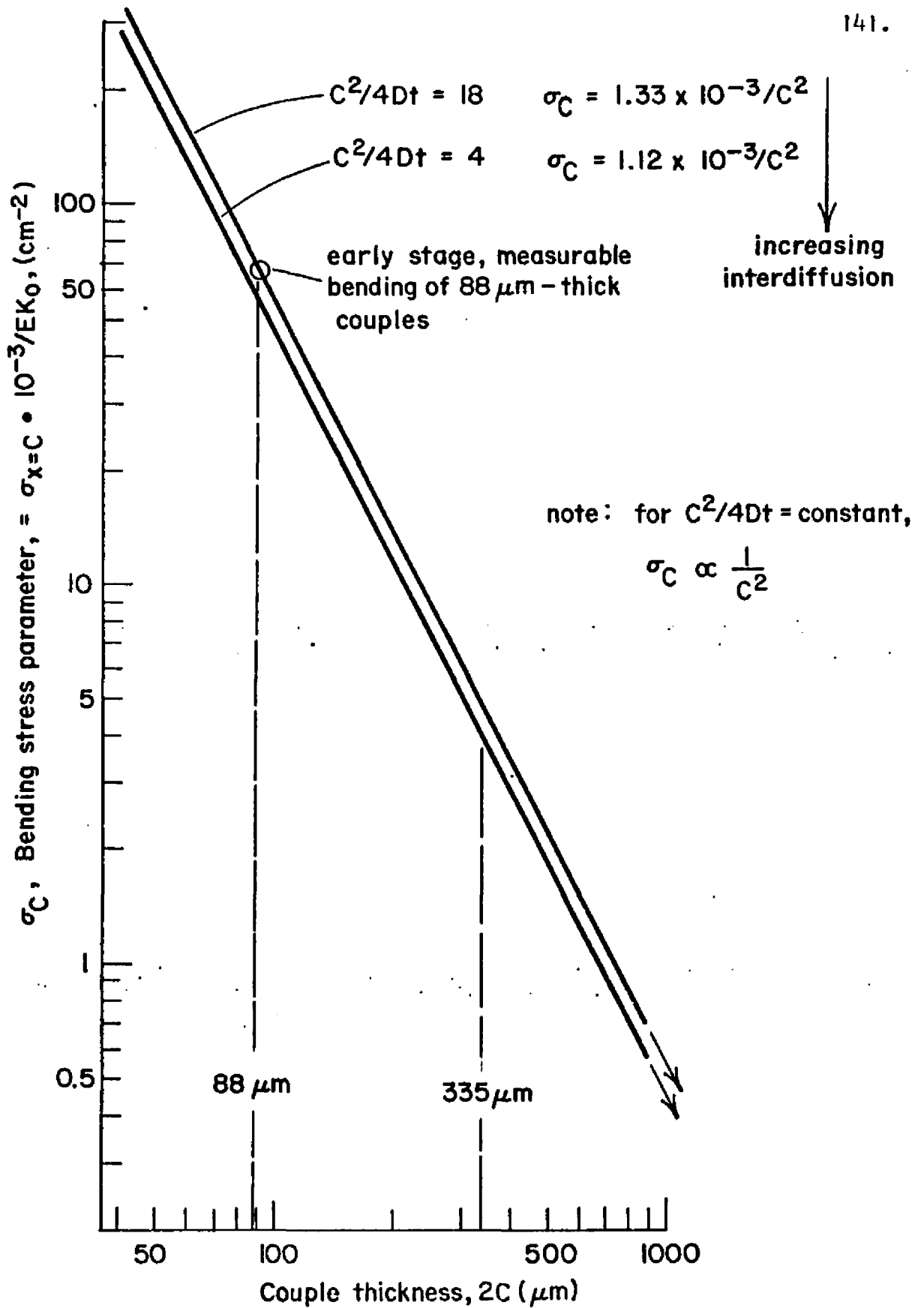


Fig. 42. Bending stress vs couple thickness and $C^2/4Dt$.

sion in the Ag-rich side and vice versa for the Au-rich side. This can be visualized from Fig. 38 by imagining a stress curve for $C^2/4Dt \ll 4$ which extends across the Ag-rich couple half without intersecting the abscissa, thereby imparting a stress at the Ag-rich end of the same sense (tension) as the maximum stress in the diffusion zone. The stress distribution for this case was not computed here. The computation would be quite lengthy and would involve the homogenizing solution to Fick's second law given by Crank.¹¹³

The occurrence of the stress reversal and unbending during advanced homogenization corresponds to the loss of the bulge and dent surface deformation in the very same couples (see Fig. 25(c)). This indicates that the reversed stresses could have contributed to the loss of bulge and dent. If so, the sense of bulge and dent deformation corresponds to the sense of the diffusion-induced stresses throughout all stages of diffusion. However, this correspondence during advanced homogenization is made uncertain by the possibility that sintering could also contribute to the disappearance of the bulge and dent. Furthermore, it is still not known how much mass flow, in itself, contributes directly to either bulge and dent or surface rippling. Therefore, the nature of surface deformation remains uncertain.

It is believed that the diffusion-induced stresses can also explain the internal cracking behavior reported earlier. The 88 μm -thick couples cracked less readily than their nil-bent, mass-constrained counterparts because the stress expended during bending lowered the stress available for cracking. Deeper welding retarded or prevented cracking by decreasing the concentration gradient, and this, in turn,

decreased the stresses generated during diffusion annealing. Also, the deeper welding probably resulted in a more mechanically-stable welding interface which resisted cracking stresses better. The increased propensity to crack at higher diffusion temperatures may have been promoted by the increased rate of stress generation at the higher temperatures; and perhaps by increased grain boundary sliding.

Porosity

Although a detailed study of porosity was not a primary goal of this research some metallographic observations of porosity and measurements of porosity shifting were made in the course of the investigation and are reported below.

Constraining Effects on Porosity;

It was found that the quantity of apparent porosity depended markedly on metallographic preparation. Therefore, measurements of the absolute amount of porosity in the couples could not be made with any reasonable amount of certainty. However, some sets of couples were mounted and prepared in the same metallographic mount, thereby permitting comparisons of the relative amounts of porosity in those particular couples. Such comparisons are given next to illustrate the observed effects of mass and mechanical constraint on the amount of porosity.

In all couples diffused free of mechanical constraint, the amount of porosity increased continuously with increasing interdiffusion. This was observed in each of the four series of couples: 88 μm / 750°C, 132 μm / 750°C, 335 μm / 750°C, and 163 μm / 850°C. Fig. 43 shows a few of the couples from the 88 μm / 750°C series. Note that the porosity

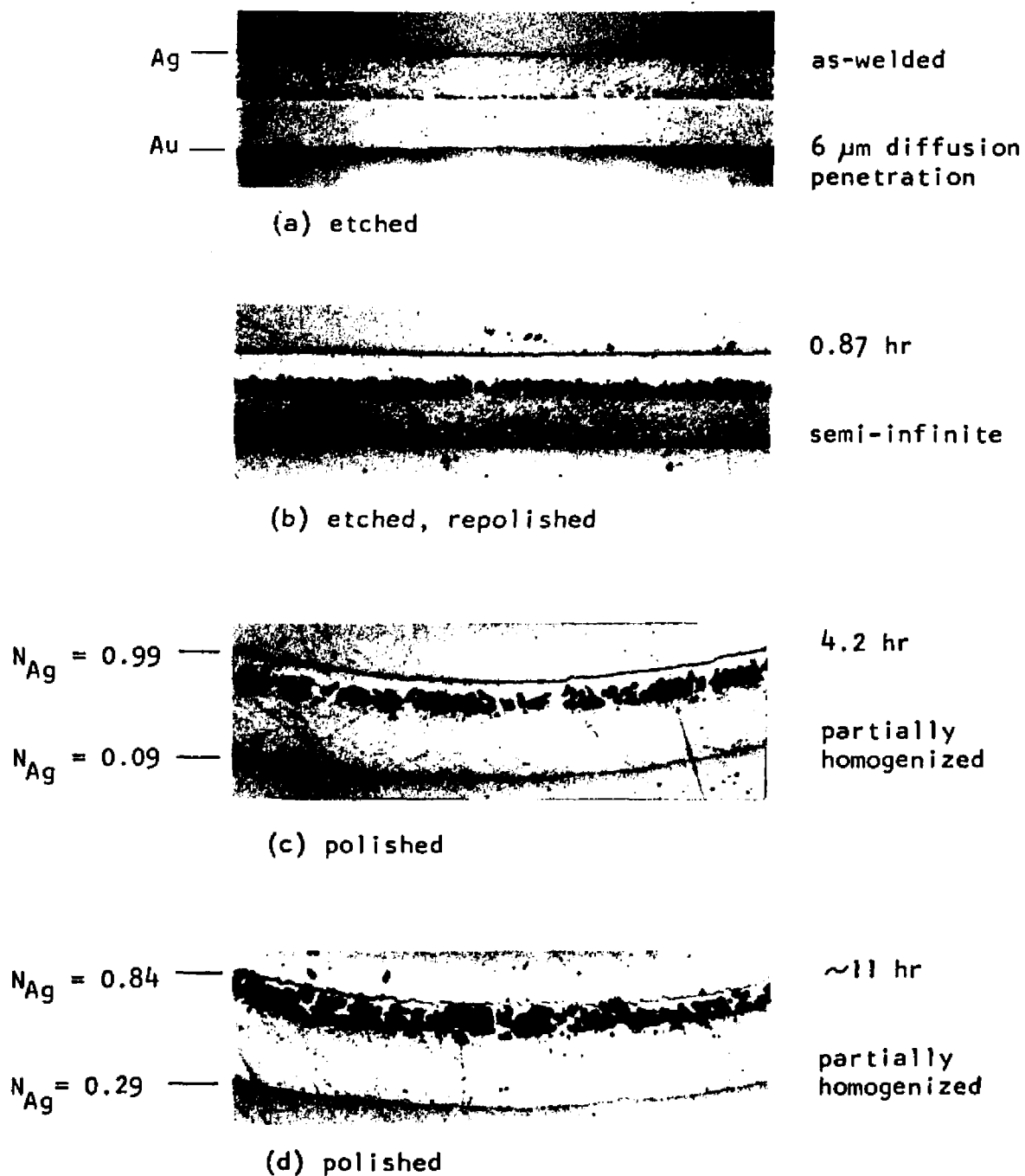


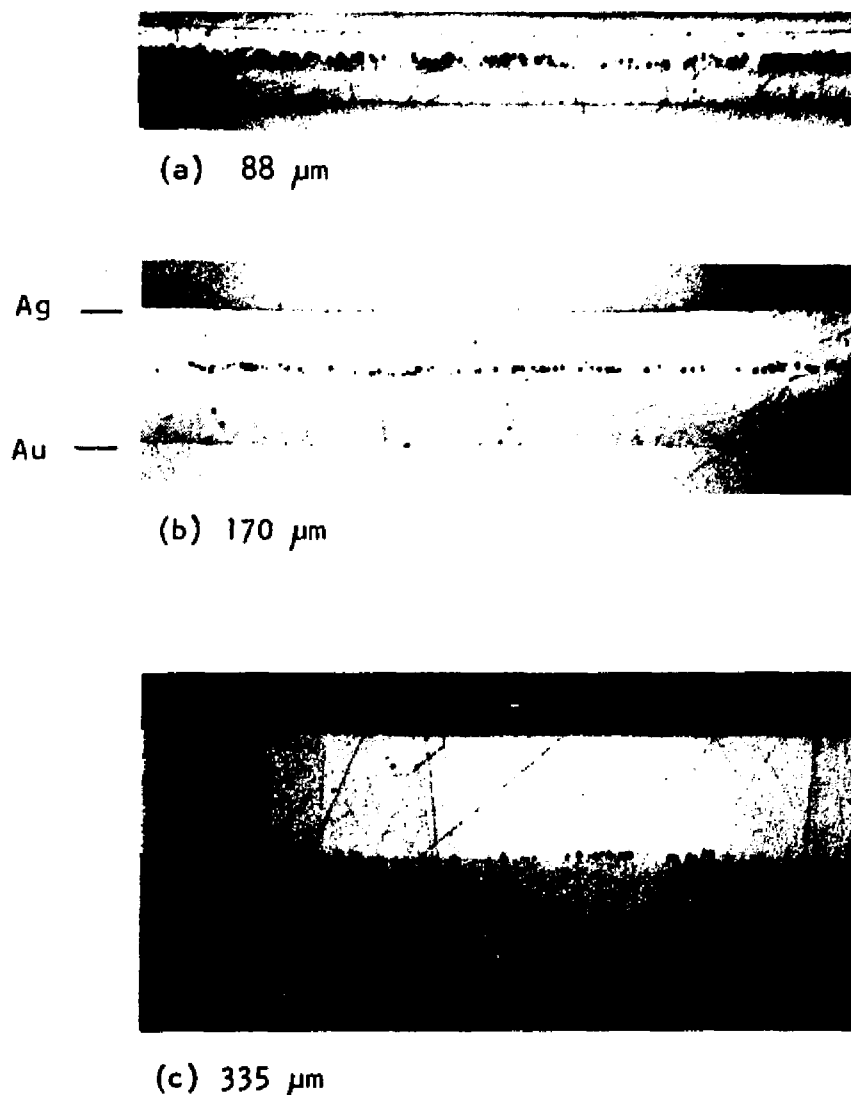
Fig. 43. Growth and shifting of porosity. Couples: 88 μm / 750°C/ times shown. All 150X. Porosity in (a) and (b) is slightly enlarged by etching.

has reached the Ag-rich terminus in the partially-homogenized couple in Fig. 43(d).

The amount of interdiffusion alone did not dictate porosity volume. For couples free of mechanical constraint, the amount of porosity decreased as couple thickness increased from 88 to 170 to 335 μm , as shown in Fig. 44. This effect of couple thickness disappeared when couples were subjected to mechanical constraint, viz, when three semi-infinite couples, 88, 170, and 335 μm -thick, were identically diffused under mechanical constraint, all three couples displayed similar amounts of porosity. This is demonstrated in Fig. 45 for two of the couples. All couples diffused under mechanical constraint had much less porosity than their nonmechanically-constrained counterparts, as typified by the two pairs of couples seen in Fig. 46, one pair being the semi-infinite, 335 μm -thick couples 14 and 15, the other pair being the partially-homogenized 88 μm -thick couples 9 and 10. Furthermore, continued diffusion of the mechanically-constrained couples beyond the very early stage of diffusion did not increase significantly the amount of porosity, as can be seen by comparing the 335 μm -thick couples diffused for ~ 2 or ~ 16 hr, Figs. 46(b) and 45(b).

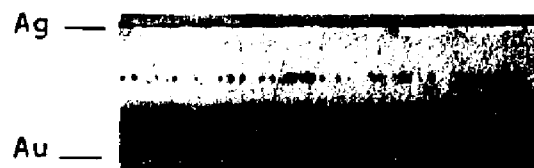
During porosity growth, the couples free of mechanical constraint underwent a slight swelling in thickness (parallel to the diffusion flow), very roughly at a rate of 2 $\mu\text{m}/\text{hr}$ during the first 4 hrs at 750°C and $\sim 1\mu\text{m}/\text{hr}$ thereafter.* This swelling results from volume

*The thickness measurements employed to detect swelling were approximate because of (1) the $\pm 1.25 \mu\text{m}$ precision limit of the vernier micrometers, and (2) the surface perturbations which developed during diffusion (grain boundary sliding, overall surface roughening).



All: as-polished, 90X

Fig. 44. Effect of couple thickness (mass constraint) on the amount of porosity in identically-diffused couples. All couples: thickness ($=2C$) shown/ 750°C 1.48 hr, semi-infinite. The amount of porosity decreases with increasing couple thickness.

(a) 170 μm

Both: as-polished, 75X

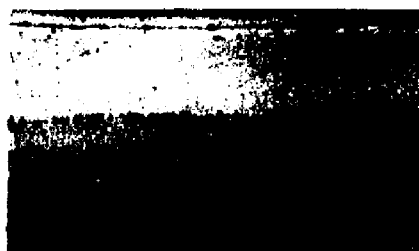
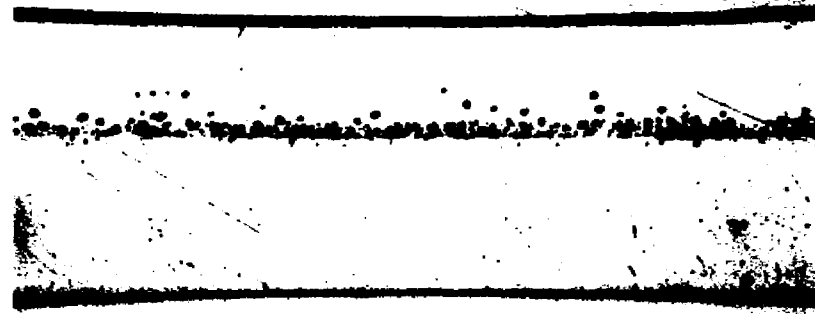
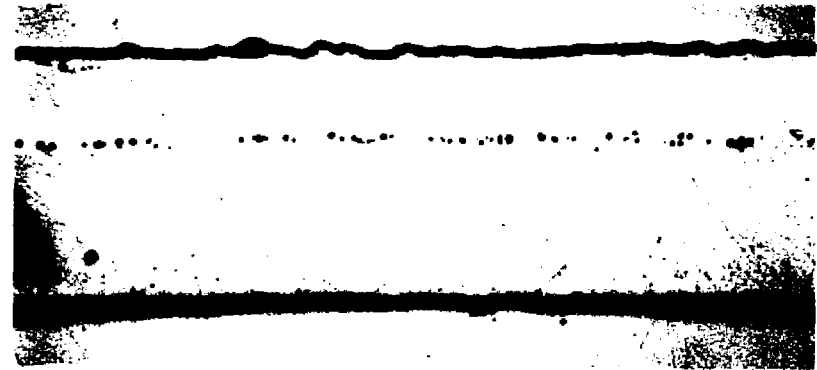
(b) 335 μm

Fig. 45. Effect of mechanical constraint on the amount of porosity in identically-diffused couples having different thicknesses. Both couples: thickness (=2C) shown/ 750°C/ 2.03 hr, semi-infinite. Porosity density is similar in both couples seen here, and is also similar in the thinnest (88 μm) couple of this series which is not shown here.



(a)

335 μm / 750°C/ \sim 16 hr, semi-infinite

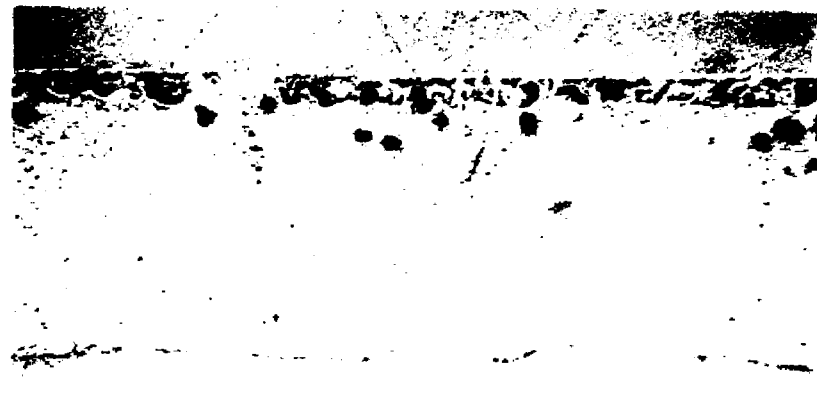


(b)



(c)

88 μm / 750°C/ \sim 11 hr, partially homogenized to $N_{\text{Ag}} \sim 0.84$ or 0.29



(d)

Fig. 46. Decreased porosity growth by mechanical constraint. The mechanically-constrained couples to the right contain much less porosity than their nonmechanically-constrained counterparts to the left. All couples: as-polished. (a), (b): 90X. (c), (d): 360X.

increases which accompany porosity formation.^{3,6,54} Conversely, the mechanically-constrained couples maintained their thicknesses throughout diffusion, or, in the case of the 335 μm -thick couple diffused for ~ 16 hr, decreased very slightly (a few μm) in thickness. The restriction to swelling and the decrease in thickness can be attributed to a slight amount of compressive creep deformation imposed by the restraining pistons. This mechanical compression also is believed responsible for the constant (or nearly constant) amount of porosity found in the mechanically-constrained couples which had differences in thickness or diffusion time. This explanation concurs in principle with the observation by others that porosity growth in bulky Kirkendall couples is readily retarded or prevented by either mechanical compression parallel to the diffusion flow⁷¹ or hydrostatic pressure.^{44,54,71*}

As noted above, porosity continues to grow and expand throughout the entire diffusion process in the (thinnest) 88 μm -thick couples, at least until the pores reach the Ag-rich surface during homogenization. Porosity growth in the thin-sheet couples is inhibited by mass- or mechanical constraint. Mechanical constraint similarly inhibits porosity growth in bulky couples.⁷¹ Unlike the 88 μm -thick couples, however, pores in bulky couples which expand during early and intermediate diffusion stages^{5,6,29,54} subsequently begin to shrink by sintering during the advanced stages of diffusion,^{5,29,54} sometimes disappearing.⁵⁴

*Porosity is prevented from forming by $\sim 1,500$ psi (hydrostatic) in Cu/Ni⁷¹ and Ag/Au,⁴⁴ whereas diffusing under vacuum results in extremely large amounts of internal porosity in Ag/Au.⁵⁴ Porosity-prevention pressures do not alter diffusion coefficients in Cu/Ni⁷¹ or Ag/Au.⁴⁴ Even pressures as high as 5,000 psi have very little effect on diffusion kinetics in Ag/Au.⁴⁰

Porosity shrinkage is promoted by hydrostatic pressure.^{54,71} Comparing these results for thin-sheet and bulky couples reveals an interesting parallel between mechanical constraint and mass constraint; either tends to inhibit porosity growth, presumably by offering resistance to porosity swelling. The mass constraint effect noted here contradicts the common assumption that mass relaxation in a direction parallel to the diffusion flow is negligible.^{3,6-8,10,12} It follows that the corollary assumption that three-dimensional diffusion-induced stresses will reduce to two-dimensional stresses by uninhibited relaxation in the diffusion direction does not appear to be valid, particularly for thicker couples. The following observation may explain why this feature of mass relaxation was not manifested in past experiments. The effect of mass constraint in decreasing porosity in the thin-sheet couples, which were roughly 0.09 mm to 0.35 mm thick, is contrary to that found for bulky couples of Cu/Ni⁶ and Cu/brass.^{3,5} In these bulky couples, the amount of porosity was unaffected by doubling the couple thickness, e.g., from 6.2 mm to 12.5 mm for Cu/brass,³ and from 8.1 mm to 16.2 mm for Cu/Ni.⁶ This discrepancy between thin-sheet and bulky couples may be due to the bulky couples offering more-than-sufficient mass constraint to relaxation processes such that critically-low values of mass constraint (couple thickness) were never attained experimentally.

A Possible Relationship Between Porosity, Marker Shifting, and Bending:

It has been shown for thin-sheet couples in the early stage of diffusion that the amount of porosity, marker shifting, and bending

were each influenced by mass- or mechanical constraint parallel to the diffusion direction. The constraints retarded porosity growth and bending while increasing marker shifting.* It was reasoned that the reduction in porosity can be attributed to the resistance to porosity swelling offered by either mass- or mechanical constraints. The same constraints retard bending. With bending and porosity formation disfavored in high-constraint couples, the stresses in these couples undergo relatively little relief by the processes of stress-induced bending or stress-induced porosity formation. It is suggested that these unrelieved stresses might enhance marker shifting by promoting dislocation climb perpendicular to the diffusion direction,** or by inducing increased plastic deformation, recrystallization, and grain growth, thereby increasing spurious marker motion.^{3,53,56} This could account for the enhanced marker shifting in the high-constraint couples, which exhibited nil bending and reduced amounts of porosity relative to the heavily-bent, high-porosity, low-constraint couples. Because the diffusion-induced stresses decrease with increasing diffusion time, the marker shifting enhancement caused by these processes are also

*This inverse relationship between porosity and marker shifting suggests that porosity might have directly affected marker motion in the particular couples under consideration. However, the marker positions were measured from the nonporous Au surface, thereby avoiding the direct influence of porosity swelling on marker measurements. Also, no porosity-entrapment of markers was observed in the particular couples under consideration. Thus, marker shifting enhancement was neither an artefact of porosity swelling nor of porosity-entrapment of markers.

**While these stresses do not directly affect climb perpendicular to diffusion, they promote such climb indirectly by acting to disfavor climb parallel to diffusion.

expected to decrease. This concurs with the results for couples 14 and 15 (Fig. 31), which show that marker shifting enhancement was not sustained beyond the early stage of diffusion. Thus, it appears likely that marker motion, bending, and porosity in thin-sheet couples are all related synergistically via the diffusion-induced stresses which noticeably influences each of them during the early stages of diffusion.* This apparent result is not based on a comfortable amount of experimental information and should, therefore, be considered tentative. Confirmation is required by a more extensive study of porosity, bending, and marker shifting in thin-sheet couples. Such an experiment is suggested in Appendix D.

The stress-related synergisms indicated above would certainly complicate any analyses of the Kirkendall effect or its consequences in thin-sheet couples. Complications due to porosity and bending would likely be avoided by diffusing nonbending bulky couples under hydrostatic pressures which prevent porosity growth. However, this would still leave the detriment of spurious marker shifting from plastic deformation, recrystallization, and grain growth.

Porosity Shifting and Porosity-Entrapment of Markers:

As shown in Fig. 43, the porosity zone shifted toward the Ag side as diffusion time increased. Accordingly, the shifting of the center of the porosity zone was measured for a series of seven, semi-infinite, 88 μm -thick couples diffused free of mechanical constraint at 750°C.

*Of course, other phenomena such as plastic flow and grain boundary sliding can also relieve diffusion-induced stresses, but their contribution to stress relief would be difficult to account for.

Shifting was also observed in other couples, mechanically constrained or not, but these couples were too few to yield a meaningful number of data points for additional shifting curves. Average porosity shifts from the original join, \bar{X}_p , were obtained by measuring from the Au terminus to the density center of the porosity zone, much the same as in the case of marker shifting. Appendix B describes the method in greater detail. Unlike markers, it could not be assumed that porosity was centered at the original join at zero diffusion time. Each porosity datum point was subject to a nonsystematic probable measuring error of $1.6 \mu\text{m}$. This is about 3 times larger than the counterpart $0.5 \mu\text{m}$ error in marker measurements because of the greater uncertainty in judging the central position of the porosity zone.

A plot of porosity data describes a parabolic ($\propto t^{\frac{1}{2}}$) curve, Fig. 47. The data were computer-fitted to the parabolic rate expression, $X_p = b + k_p t^{\frac{1}{2}}$, where it was found that $b = 3.9 \mu\text{m}$ and $k_p = 7.6 \mu\text{m}/\text{hr}^{\frac{1}{2}}$. Although the results indicate that the porosity shifting curve does not extrapolate directly back to the original join, this indication is not conclusive because of the probable measuring error and the lack of data for very short ($< 0.5 \text{ hr}$) diffusion times. Only one porosity shifting curve was located in the literature for comparative purposes (Heumann and Kottmann).¹¹⁴ They show only two data points (7 and 10 hr at 900°C for a Ag/Au couple) lying reasonably near a parabolic curve extrapolated to $X_p = 0$, $t = 0$. Had they extrapolated a parabolic curve solely from their data, it would have yielded the unreasonable result $X_p = 60 \mu\text{m}$, $t = 0$. Conversely, their extrapolation to the original join

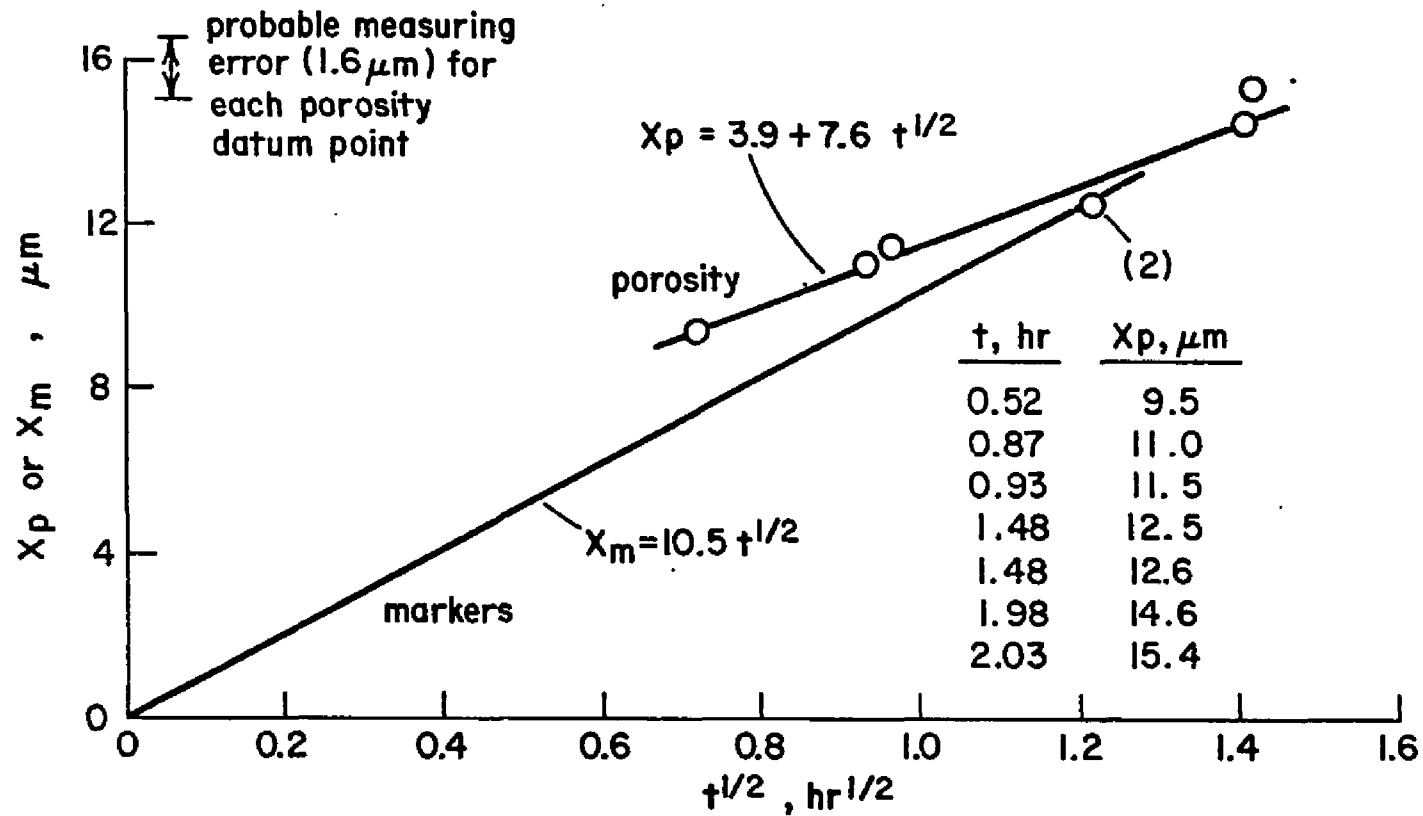


Fig. 47. Shifting of porosity and markers in semi-infinite, $88\ \mu\text{m}$ -thick couples diffused free of mechanical constraint at 750°C .

was a tacit assumption because it is not known whether or not Kirkendall porosity actually originates at the original join. Hence, their data neither refutes nor supports the result shown in Fig. 47 that porosity shifting does not extrapolate directly back to the origin.

It is seen from Fig. 47 that porosity lies in advance of the markers during very early diffusion times, but markers, migrating faster than porosity, eventually intercept the porosity zone after ~ 2 hr ($t^{\frac{1}{2}} \sim 1.4$ hr $^{\frac{1}{2}}$). This graphical interception concurs with the earlier observation that markers were entrapped in the porosity zone in couple 5. The absence of similar entrapment in mass- and/or mechanically-constrained couples diffused for ~ 2 hr was most likely due to the substantially smaller amounts of porosity in these couples. For longer (> 2 hr) diffusion times at 750°C, mechanical constraint continued to maintain minimal amounts of porosity, thereby accounting for the absence of entrapment in couples 10 and 15. However, porosity growth did occur in the mass constrained couples, resulting in porosity-entrapment of markers at the longer diffusion times. This was evidenced by entrapment during 750°C diffusion in couple 14 (335 $\mu\text{m}/ \sim 16$ hr) and in the bulky couples 8 mm/ ~ 5 and 16 hr.

The finding of markers in and near pores has also been reported occasionally for bulky couples,^{3,5,42,57} but such observations were, with one exception,⁵⁷ mentioned only casually. This lack of serious concern over porosity-entrapment of markers in the past was probably due simply to the entrapped markers being very seldom discovered during microscopic examination, and also because of the absence of concomitant observations of porosity shifting and growth.

When the porosity-entrapment factor is added to the spurious effect on marker motion by plastic deformation, recrystallization, and grain growth, the prospect of markers measuring only mass flow becomes very discouraging, especially in light of the large amount of marker scatter observed in this research and by others.^{42,45} But even these shortcomings in marker measurements do not appear to alter the conclusions reached earlier concerning the mass flow/dislocation climb model. This is because the marker shifting results failed by more than an order of magnitude to account for bending by mass flow/dislocation climb, and also because of the other features (bending of non-diffused material, unbending, temperature sensitivity) which could not be explained by the mass flow/dislocation climb model.

Porosity Networks:

During the earlier homogenization stages of diffusion, porosity was found to exist along the entire length of many of the grain boundaries which extended from the porosity zone to the free surface of the Ag-rich terminus, as shown in Fig. 48(a,b). Most often these porous boundaries were approximately normal to the free surface. Although grain boundaries are known to be short circuit diffusion paths^{81,115} and preferential sites for individual pores,^{9,76} the extension of porosity along the entire length of the grain boundaries of the couple in Fig. 48 is not typical of solid-solid Kirkendall couples. It is, therefore, possible that diffusion-induced tensile stresses in the Ag-rich region promoted the cracking open of the boundaries in a manner similar to the grain boundary cracking observed in the dezincified (tensile) regions of brass sheets.⁹ During metallographic plating, the

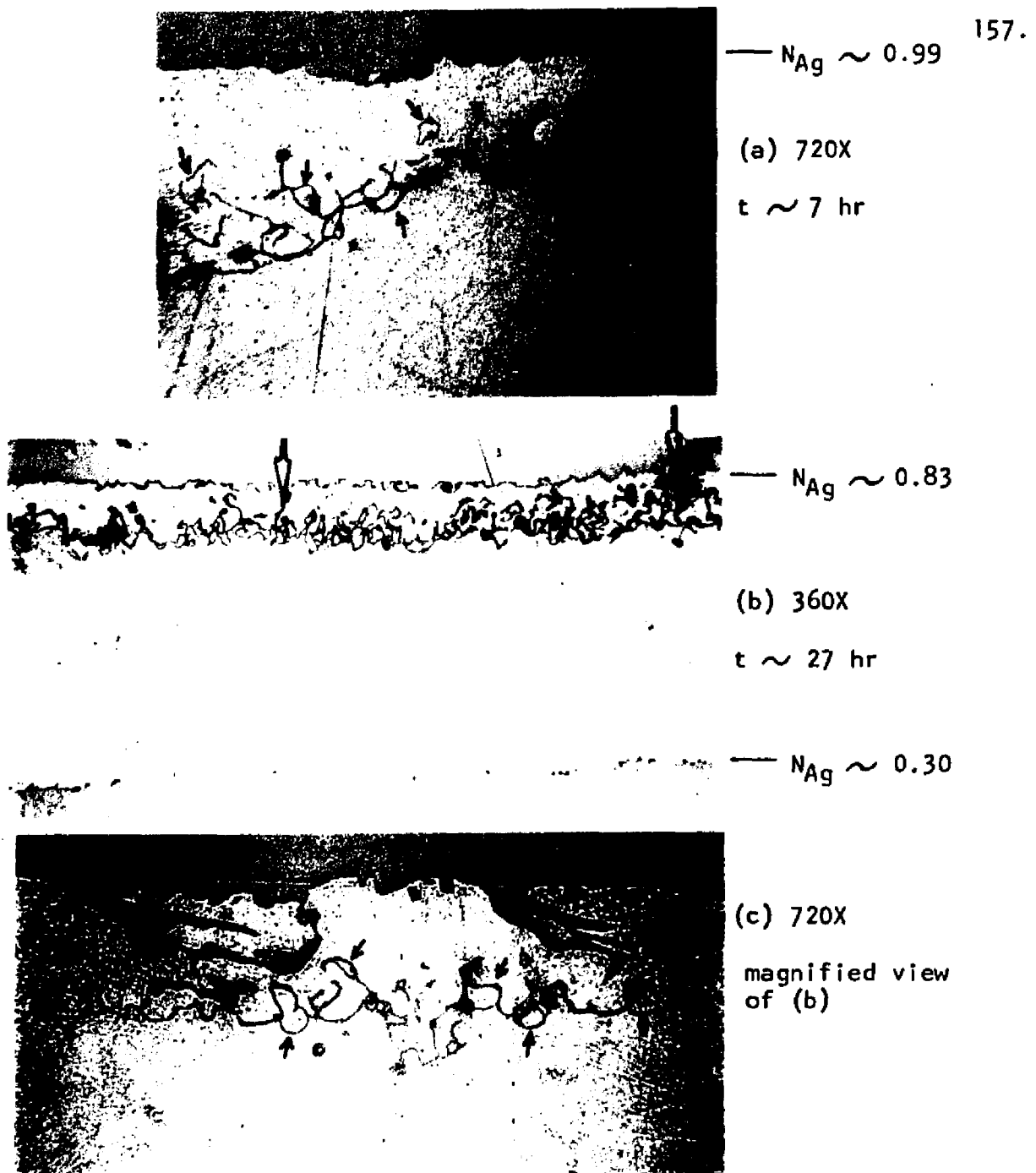


Fig. 48. Porosity networks in partially-homogenized couples. Couples $132 \mu\text{m} / 750^\circ\text{C} /$ times shown. Nickel-filled porosity is grey; unfilled porosity is black. (a), (b): large arrows indicate porous grain boundaries which extend from the porosity zone to the Ag-rich free surface. (a), (c): small arrows indicate the network nature of the porosity zone.

nickel often deposited along these porous boundaries and into the porosity zone, thereby delineating the continuous network nature of the porosity zone, Fig. 48. This interconnected network of porosity is also seen in Fig. 49 for a couple just beginning homogenization, with the difference that most of the porosity is not filled with nickel because most of the grain boundaries leading to the surface were not sufficiently porous to allow deep penetration of the electrodeposited nickel. However, the electron microprobe revealed that nickel had penetrated portions of the porosity zone. This case is shown in Fig. 49(c), where the large, well-defined network at the center of the figure is nickel-filled. Those portions of the network not filled with nickel (e.g., Fig. 49(a,b)) were observed during light microscopy to be quite porous, especially after mild etching. Thin networks of porosity also appeared in the early stages of semi-infinite diffusion, as seen in a 335 μm -thick couple with a 62 μm interdiffusion zone, Fig. 50. Similar porosity networks were present in the thinnest (88 μm -thick) couples, as seen in Fig. 51 for a couple diffused to its semi-infinite limit. Decreasing the diffusion times in the 88 μm -thick couples yielded porosity networks which were less porous and less well-defined; this is seen in Fig. 52. During the early stage of interdiffusion, the porosity network is either connected to or immediately adjacent to the multigrain boundary (formed during welding) which migrates in the same direction as the porosity zone. This is seen in Fig. 50 and 52. For interdiffusion zones greater than about 85 μm , the multigrain boundary appears to disappear or lose its identity. The onset of this can be seen in the center portion of Fig. 50(c), and

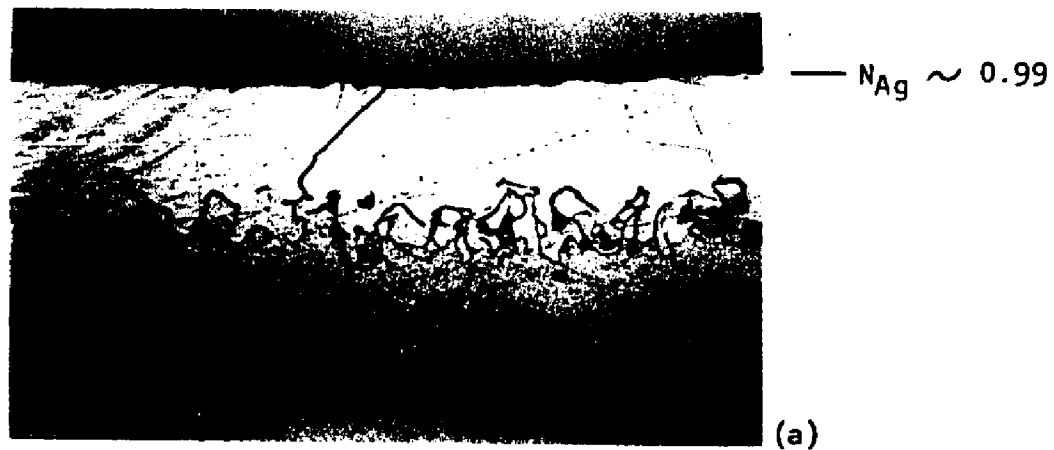


Fig. 49. Porosity network in a couple in the very early stage of homogenization. Couple: $170 \mu\text{m} / 750^{\circ}\text{C} / \sim 17 \text{ hr}$. All; mild etch, 360X.

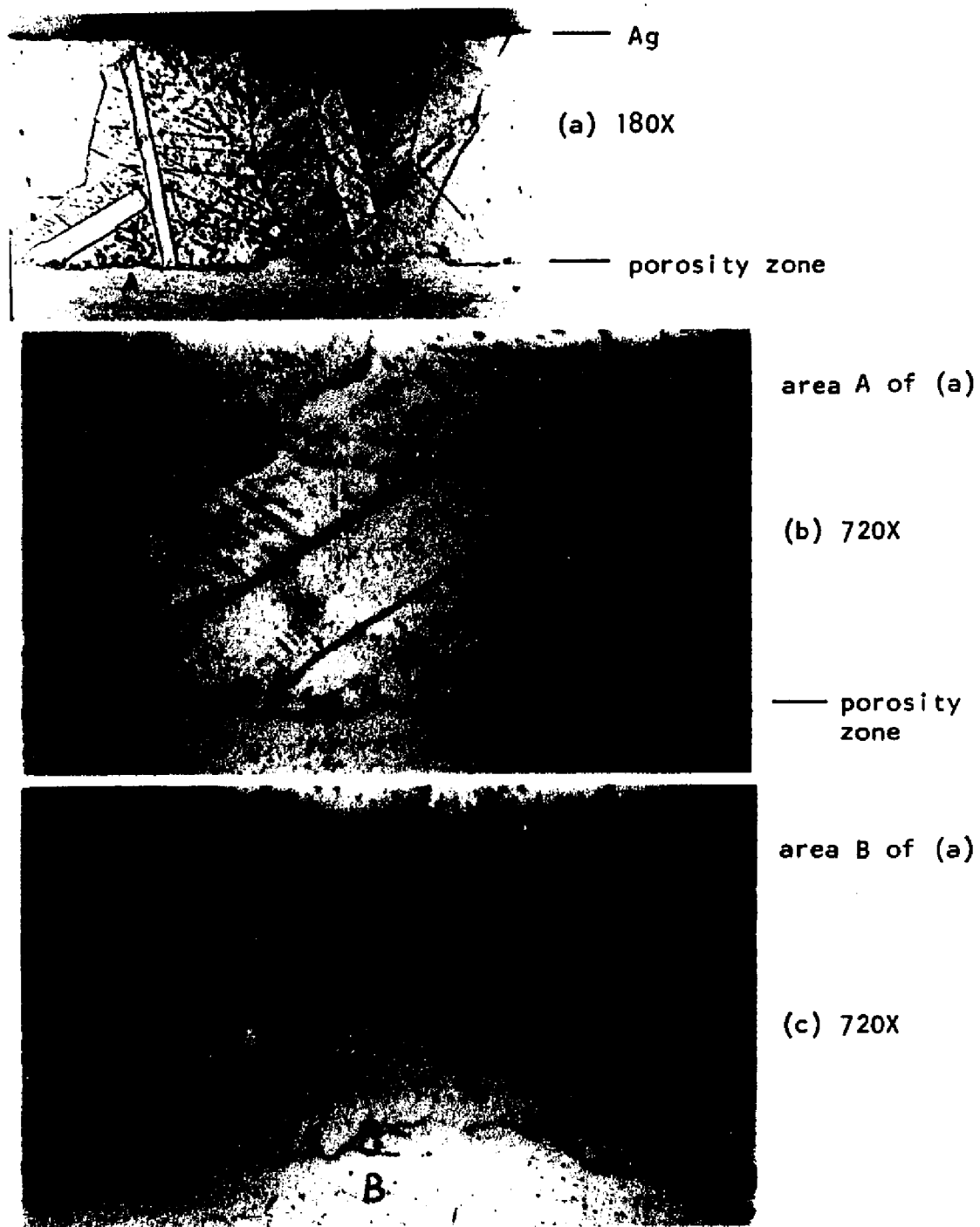


Fig. 50. Porosity network in the semi-infinite couple $335 \mu\text{m}/750^\circ\text{C}/1.48 \text{ hr}$. All: moderately etched.

(---continued)

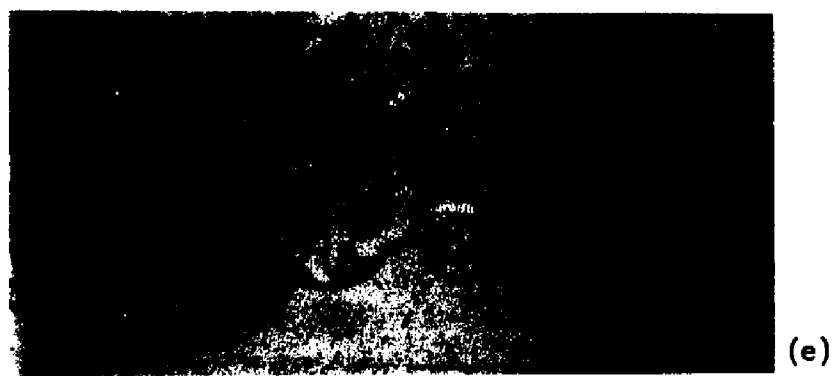
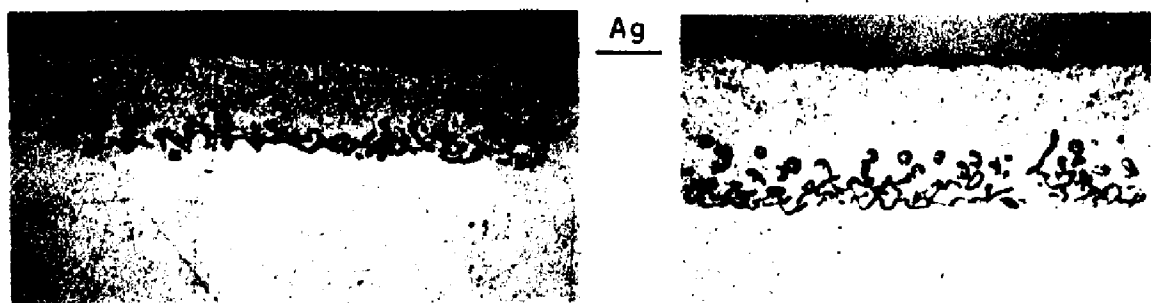


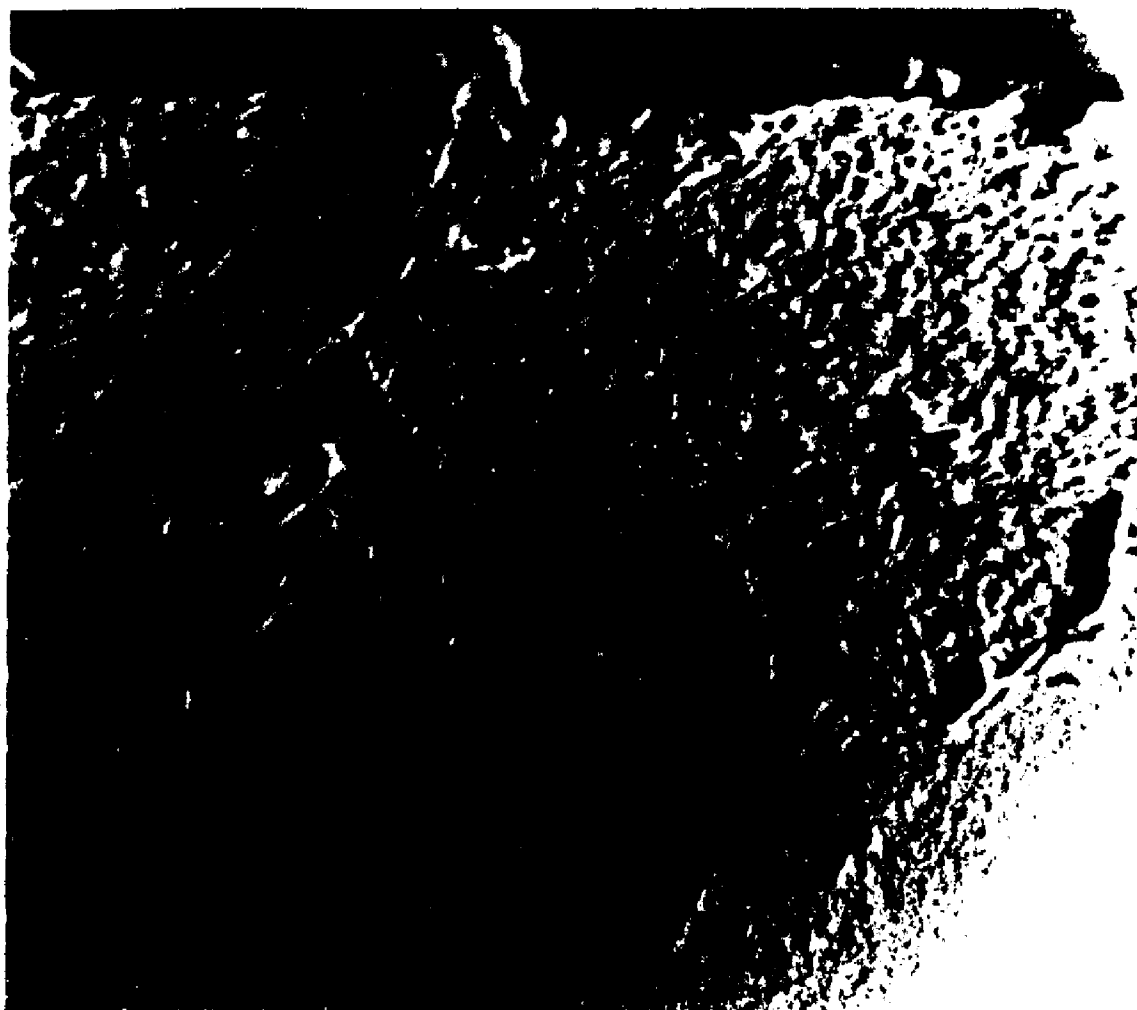
Fig. 50 --- continued. All: 720X. Porosity-bounded material dislodged during polishing created the hole (arrow) shown in (d).



(a) 360X

light micrographs

(b) 720X



(c) scanning electron micrograph

~2,500X

Fig. 51. Porosity network in a couple diffused to about its semi-infinite limit. Couple: $88 \mu\text{m}$ / 750°C / 2.37 hr. All: mild etch.

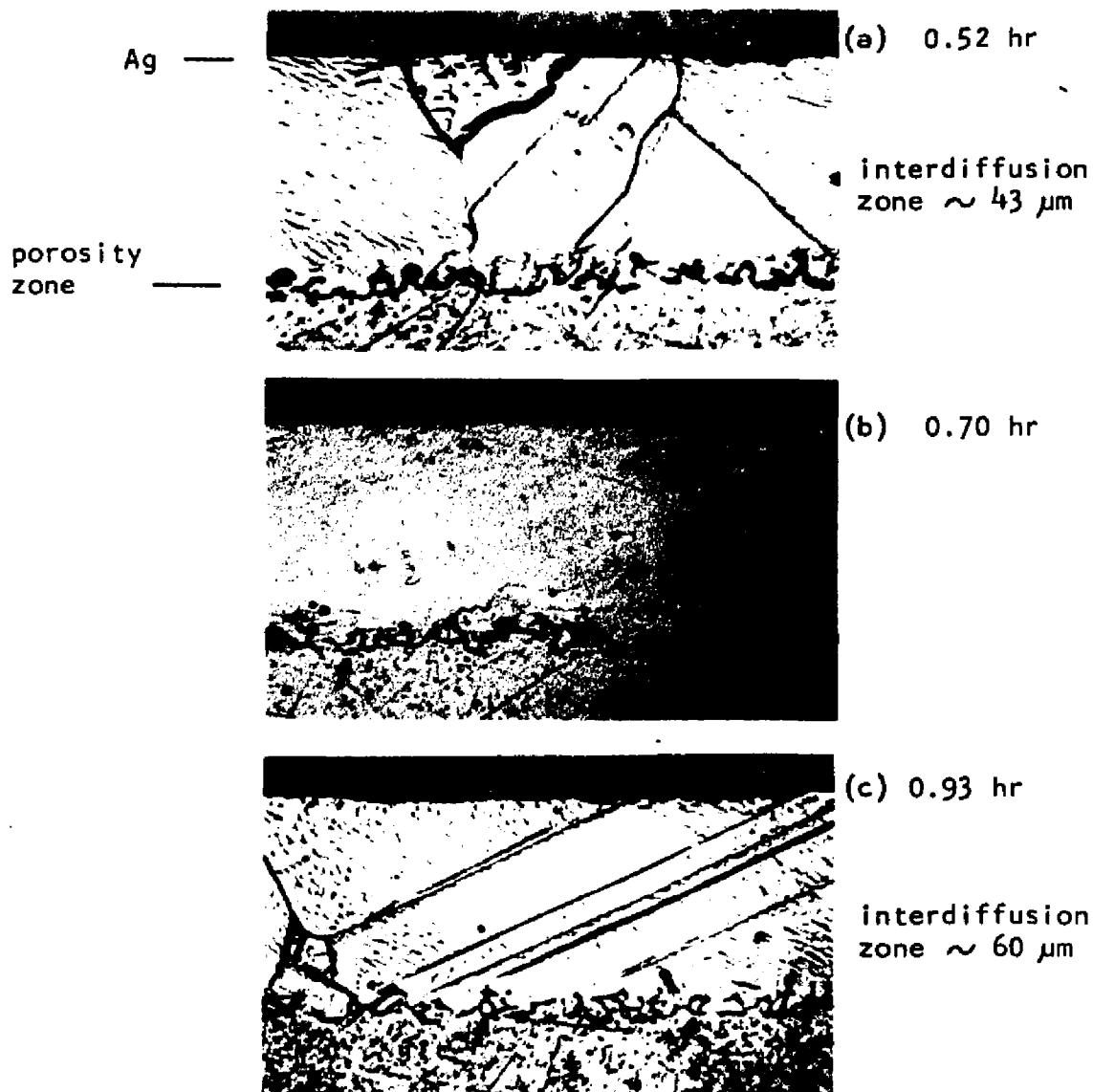


Fig. 52. Porosity networks in the semi-infinite couples $88 \mu\text{m}/750^\circ\text{C}$ / times shown. All etched, 720X.

Fig. 49 reveals the case for more extensive diffusion. In contrast to this, the advancing multigrain boundary in bulky couples is commonly observed throughout extensive diffusion anneals, e.g., ref. 54.

Preservation by nickel filling eliminates the possibility that the porosity network resulted artificially from hole-type pores being filled in by smear metal during metallographic polishing. For those networks not filled with nickel, etching experiments using high magnification light microscopy and scanning electron microscopy revealed that the etching response of the porosity-bounded island material was crystallographic in nature, and not the rapid, irregular attack expected of severely-distorted smear metal.

There is reason to believe that the thin networks of porosity are actually former subboundaries along which porosity formed preferentially during diffusion, and the porosity-bounded islands of material are subgrains or former subgrains.* In support of this, it is well-known that substructure develops in the diffusion zones of solid/solid Kirkendall couples.^{3,6,12-15,27,28} Substructure was found, via TEM, in the Au-rich side of couples employed in this investigation; it is reasonable to expect that counterpart deformation processes also formed substructure in the Ag-rich (porosity) side of the couples. Moreover, the subgrains of about one to several microns in diameter seen in TEM of the Au-rich side are comparable in size and shape to the suspect subgrains seen in the light micrographs of the Ag-rich side.

*The term "subgrain" is employed here rather loosely because the original crystallographic identity of the subgrain may become lost as recrystallization annealing occurs during diffusion.

Subboundaries (both tilt and twist types) are short-circuit diffusion paths in Ag,^{82,90,91} and would likely serve as effective vacancy sinks.^{110,116,117} Large vacancy fluxes along the subboundaries could lead to heterogeneous porosity formation there, resulting in a porous network along subgrain boundaries.

Except for weld-line porosity, porosity formation was not found at other sites, such as impurity particles^{9,10,71,72,76} or stress-induced fissures,^{8,17} which are suspected or calculated to exist throughout the porosity zone, but whose roles as porosity sites remain largely uncertain.* Porosity in as-welded couples formed along the welding interface in couples of this research, in Cu/Ni couples,^{5,71} and also in couples of like metals, namely Ni/Ni^{5,53} and Cu/Cu⁵ (hence, it appears that vacancy fluxes from Kirkendall diffusion are not required for the formation of porosity at metal joins). Barnes and Mazey⁷¹ suggested that these interface pores could serve as heterogeneous nucleation sites for porosity. However, there are no observations or evidence of such pores growing or migrating, nor do they explain why the number of voids increases as diffusion increases.⁵⁴ Thus, if interface pores are involved in the development of porosity in thin-sheet couples, their role may be limited to serving as vacancy sinks at the very outset of diffusion, whereupon subboundaries generated in the interdiffusion zone may subsequently become dominant vacancy

*Porosity will form at large, foreign particles (e.g., inclusion stringers) in the porosity zone,⁷⁶ but such particles are certainly not required for porosity formation because porosity forms readily in couples made of very pure metals, as shown by this work and by others.^{3,6,28,72} Nor do the infrequently-observed internal cracks^{9,30,31} appear to be related to porosity formation.

sinks which grow at the expense of shrinking interface pores. This is speculation; too little has been observed of porosity in the very earliest stages of diffusion to be reasonably certain of the nature of porosity formation. Even so, the above rationalization is compatible with experimental observations.

Although the "network" form of porosity was found in a wide variety of thin-sheet couples (88 to 335 μm -thick, various diffusion times), individual hole-type pores instead of "networks" were typical of many of the thin-sheet couples and the two substantially-diffused bulky couples. The reason for this inconsistent presence of porosity "networks" is not known. Not enough systematic information was revealed by the couples to indicate whether or not factors such as grain size, couple thickness, diffusion time, etc., were influencing or controlling the formation of porosity networks. It is suspected that much of the uncertainty concerned with porosity networks is due to the great difficulty in revealing the porosity metallographically. For example, the network configuration of porosity was very difficult to retain during metallographic polishing, except, of course, for those cases where nickel filling preserved the network. Otherwise, a slight "excess" of polishing would begin to dislodge the porosity-bounded subgrains leaving holes as shown in Fig. 50(d). Additional excess polishing of only a minute or so tended to enlarge and obscure the shape of the newly-created holes until the porosity zone consisted of large, poorly-resolved holes or pits. This latter form of hole-type porosity is seen in most of the micrographs of this report and is typical of the porosity usually displayed in Kirkendall diffusion couples.

Thin porosity networks common to the thin-sheet couples have not been reported for typical bulky Kirkendall couples comprised of welded, large-grained components. Too little is known about the formation of porosity networks to explain this difference, but the explanation might be related to differences in the proximities of surface sinks, welding parameters, or diffusion annealing temperatures. Concerning the surface sink possibility, the terminal surface of a thin-sheet couple may act as a sink for excess vacancies which are created in the relatively-nearby interdiffusion zone, especially by means of short-circuit vacancy diffusion along grain boundaries which link the porosity network to the surface. Such vacancy annihilation at the surface would decrease the rate at which porosity-bounded subgrains are consumed by internal vacancy condensation, thereby tending to preserve the network form of porosity. Considering the welding parameters, the welds of thin-sheet couples featured very shallow interdiffusion zones of a few μm which were obtained under moderate thermal expansion stresses. On the other hand, bulky couples are usually welded to depths roughly a hundred μm while under large, external compression loads.^{5,6,30,38,44} In bulky couples, the high compression will retard or prevent the formation of porosity,^{54,71} and the deep interdiffusion will greatly diminish the concentration gradient within the couples, thereby decreasing the magnitude of the diffusion-induced tensile stresses which are generated in the porosity zone during subsequent diffusion annealing. Conversely, porosity formation in the shallow-welded, thin-sheet couples is, almost from the outset of interdiffusion, free of external compression, and the much steeper concentration

gradients present when diffusion annealing begins would produce relatively large, diffusion-induced tensile stresses in the porosity zone. Thus, during the earlier stages of porosity formation, the state of stress in the two types of couples (bulky versus thin-sheet) is considerably different. While it is not clear in what manner the state of stress alters the form or shape of porosity, it has been observed,^{54,71} and calculated^{8,10} that stress does influence porosity formation. Supporting this, it was found in this research that mass constraint (couple thickness) reduces porosity formation. Also, the higher initial stresses in the thin-sheet couples are expected to generate more subboundaries than in the bulky couples. If so, this could favor the formation of porosity along subboundaries in thin-sheet couples. It therefore seems likely that the different forms of porosity (holes versus networks) in the two types of couples might be due, to some extent, to differences in their states of stress. Addressing the effect of diffusion annealing temperatures, the 750°C employed for the thin-sheet couples is $\sim 0.75 \bar{T}_{\text{melt}}$, which is less than the 0.85 - 0.95 \bar{T}_{melt} generally employed in diffusion studies of bulky couples. This would result in relatively more grain boundary and subboundary diffusion (short-circuiting) of vacancies in the thin-sheet couples, thereby promoting porosity development along subboundary networks.

Porosity Shape:

The hole-type pores found in the thin-sheet couples (and most bulky couples) were not always rounded in shape. When several polished couples were substantially etched, many pores were polyhedral in shape, appearing to be bounded by low-index crystallographic planes, as

in Fig. 53. These are similar to polyhedral pores found by others^{5,6, 28,44,114,118} in a variety of Kirkendall couples. Barnes⁶ attributed polyhedral pores to surface energy minimization. The same explanation was used by subsequent investigators,^{28,44} and also by others to explain polyhedral shapes which developed during extensive annealing of rounded metal particles,⁷³ and polyhedral gas bubbles created by annealing argon-bombarded Ni foils.⁷⁴ Note that several pores in Fig. 53 appear to be subgrains surrounded by porosity; some of these are indicated by arrows. Fig. 53 also shows the preferential formation of porosity at grain boundaries, as is common to bulky couples. The dual porosity features of polyhedral shape and porosity-bounded subgrain material also appeared in an 88 μm -thick couple diffused well into the homogenization state. This is seen in Fig. 54 where most of the porosity is preserved by nickel filling. The crystallographic faceting of the indicated pore (A) in Fig. 54 has been rounded at its upper corner, probably by sintering. Similar crystallographic faceting was characteristic of several other pores in the couple seen in Fig. 54. The crystallographic shapes being preserved by nickel filling dispels the possibility that they were formed by etching attack. (Barnes⁶ also eliminated etching as a cause by using microradiography to image polyhedral pores in very thin Cu/Ni couples.) Polyhedral pores were also found in some thicker, semi-infinite couples diffused at 750°C, e.g., a 335 μm -thick couple diffused for ~ 16 hr and 8 mm-thick (bulky) couples diffused for ~ 5 or ~ 16 hr. They were never found for (750°C) diffusion times < 2 hr, but neither were they characteristic of all the couples diffused > 2 hr. Couples containing

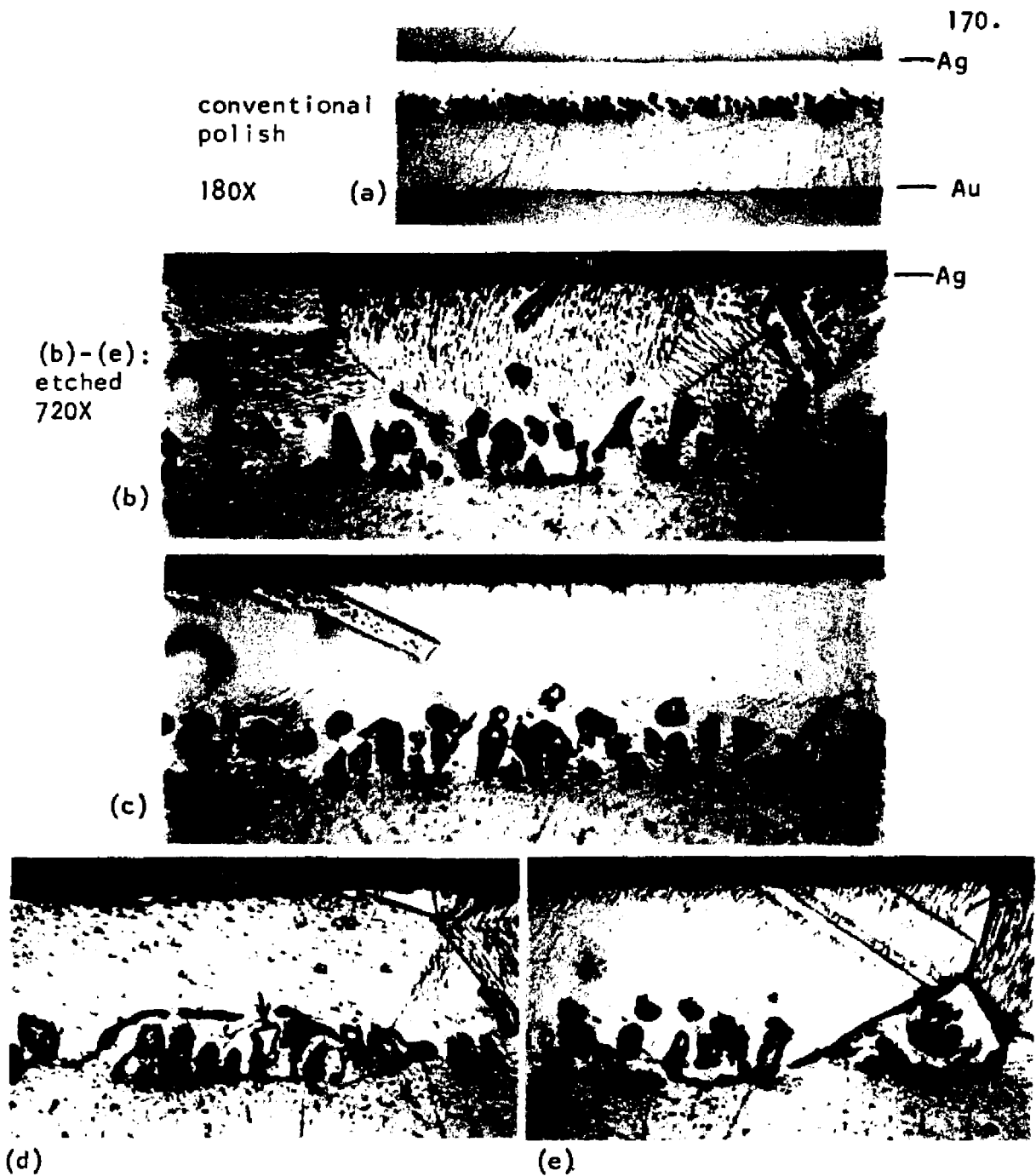


Fig. 53. Polyhedral pores in the semi-infinite couple $88 \mu\text{m} / 750^\circ\text{C} / 1.98 \text{ hr}$. Several pores, such as those arrowed in (c) and (d), appear to be islands of couple material surrounded by porosity. Preferential pore formation is seen along some of the grain boundaries.

Ag-rich terminus, where
 $N_{Ag} = 0.735$



Fig. 54. Porosity network open to the couple terminal surface. Partially-homogenized couple $88 \mu\text{m} / 750^\circ\text{C} / \sim 16 \text{ hr}$. Most of the porosity network is filled with metallographic nickel. Many islands of couple material are surrounded by porosity, such as the one at A. These islands might be former subgrains with porous boundaries. Note the crystallographic shape of some of the pores, e.g. at A.

polyhedral pores also had nonpolyhedral (rounded) pores in adjacent regions along the porosity zone, and this mixing of pore shapes often occurred within a single Ag-rich grain. The observation that polyhedral pores appeared only occasionally in the Ag/Au couples of this investigation appears to be consistent with the experience of others. Rounded, hole-type pores have been the only shapes reported for Ag/Au couples by some investigators,^{3,119} whereas polyhedral pores have been shown for similar Ag/Au couples.^{5,44,114} Similarly for other Kirkendall binary couples, reports of randomly-shaped pores in Cu/Al,³ Cu/Ni,^{3,120,121} and Cu/Zn^{3,9} couples are not consistent with observations by others that similar couples (Cu/Al,¹¹⁸ Cu/Ni,^{5,6} Cu/Zn,⁵ and Au/Pt²⁸) exhibit polyhedral pores. These apparent discrepancies in pore shapes may be due, to some extent or another, to the difficult-to-control affect of metallographic preparation on porosity shape, as experienced in this research. Also, since pores in substantially-diffused coupled undergo sintering,^{5,54} sinter rounding of the corners of polyhedral pores (e.g. Fig. 53) is expected to obscure polyhedral shapes, perhaps more in some couples than in others. The metallography and sintering factors are merely guesses at explaining discrepancies in observed pore shapes, and will likely remain so until much more is known of the nature of porosity and pore shapes.

All of the above-reported inconsistencies in the form and shape of porosity indicate that the nature and details of porosity are not at all well understood. Past analyses employing kinetic and thermodynamic treatments of Kirkendall porosity have assumed porosity to consist of individual, spherical holes of uniform size.^{8-10,12,72,76}

The foregoing observations indicate that such assumptions are not generally valid.

CONCLUSIONS

1. A study of polycrystalline, thin-sheet Ag/Au couples, 88 to 335 μm -thick in the diffusion direction, revealed several interesting features of thin-sheet Kirkendall couples, the most notable being a better understanding of bending deformation caused by diffusion-induced stresses.
2. In 88 μm -thick couples diffused at 750°C, the onset of measureable bending occurs when the interdiffusion zone extends about halfway across the couples.
3. Couple bending is caused primarily by diffusion-induced stresses perpendicular to the diffusion flow which are generated throughout a couple by nonequilibrium vacancy concentrations in the interdiffusion zone. (The vacancy gradients arise from unequal diffusion rates of Ag and Au, $D_{\text{Ag}} > D_{\text{Au}}$, and the stresses result principally from the subsequent elimination of the vacancy gradients by the annihilation or creation of lattice sites. Atomic misfit stresses are negligibly small in this alloy system.)
4. Bending behavior is indicative of high-temperature, low-stress creep deformation.
5. Accomodation of mass flow by dislocation climb parallel to the diffusion direction may make a minor contribution to couple bending in the interdiffusion zone of a couple, but even so, the stresses control the overall bending process.
6. Bending increases with time up to the very advanced stage of

homogenization, whereupon unbending commences. This unbending corresponds to a change in the sense of (calculated) bending stresses in the outer most portions of a couple.

7. Bending can be retarded or prevented by mass constraint (couple thickness parallel to the diffusion direction) or by mechanical constraint (pistons held against both broad faces of a couple). Stress calculations show that mass constraint retards bending by reducing considerably the bending stresses in the outermost, nondiffused portions of a couple. By the time the outermost material undergoes diffusion, the ever-decreasing bending stresses are too low to induce measureable bending.

8. Higher diffusion temperatures promote bending, presumably because of less resistance to creep deformation.

9. Stresses arising from vacancy gradients in thin-sheet Ag/Au couples also cause plastic deformation phenomena. These are grain boundary sliding, destruction of original crystalline boundaries, subgrain formation, recrystallization, grain growth, internal cracking, and perhaps, surface deformation. All but grain boundary sliding are also found in (very much thicker) bulky Kirkendall couples.

10. Parabolic marker shifting ($X_m = kt^{\frac{1}{2}}$) occurs in thin-sheet Ag/Au couples. Marker scattering within any given couple is roughly $\pm \frac{1}{4}$ of its average marker shift.

11. In the early stages of diffusion, mass- or mechanical constraint increases the rate of marker shifting to about the same extent.

12. Extensive porosity can form in thin-sheet Ag/Au couples.

13. Porosity growth is continuous in the thinnest (88 μm -thick)

couples diffused free of mechanical constraint, at least until the porosity reaches the Ag-rich surface. Mass- or mechanical constraint decreases porosity by inhibiting relaxation in the diffusion direction as porosity growth attempts to expand the couple material. The effect of mass constraint in reducing porosity growth indicates that the relaxation of nondiffused couple material parallel to the diffusion direction is, contrary to a common assumption, not negligible.

14. The porosity zone migrates toward the Ag side during diffusion. The center of the porosity zone in semi-infinite, 88 μm -thick couples shifts parabolically. Measurements indicate that the center of the porosity zone does not extrapolate to the original join at $t = 0$, but this is somewhat uncertain because of measurement uncertainties and the lack of data for very short diffusion times.

15. There are indications that porosity, marker shifting, and bending may be synergistically related via the diffusion induced stresses which influences each of them. This is based on the observation that marker shifting is enhanced when porosity and bending are retarded by mass- or mechanical constraint in the direction parallel to diffusion. Because constraint (mass or mechanical) reduces porosity growth and bending, the diffusion-induced stresses in highly-constrained couples experience relatively little relief by the processes of bending and porosity formation. It is suggested that these higher stresses might enhance marker shifting by promoting climb perpendicular to diffusion flow, and by inducing increased plastic deformation, recrystallization, and grain growth, thereby increasing spurious marker motion. This stress-related marker shifting enhancement is not observed beyond

the early stage of diffusion, probably because the magnitude of diffusion-induced stresses decreases as diffusion progresses.

16. Porosity-entrapment of markers occurs in some high-porosity couples. This entrapment, plus purported spurious marker motion related to plastic deformation, casts doubt on the ability of markers to truly measure mass flow in Kirkendall couples.

17. Porosity in several of the thin-sheet couples consists of thin networks of porosity, supposedly formed by heterogeneous vacancy condensation along subboundaries which were generated during diffusion. This creates porosity-bounded islands of subgrain (or former subgrain) material which appear to shrink, sometime disappearing, as porosity grows during diffusion. The factors which control the thin-network mode of porosity formation are not known; but the nearby free surface acting as a vacancy sink in thin-sheet couples may be partly responsible. Welding parameters and diffusion temperatures might also be influencing factors.

18. Both polyhedral and somewhat-rounded pore shapes exist concomitantly in wide variety of thin-sheet and bulky Ag/Au couples, as they appear to do in other Kirkendall couples comprised of various binaries. The reason for inconsistent porosity shapes seen here and by others is not known, but may be due - in part, at least - to the failure of conventional metallographic preparation methods to unambiguously reveal the true shape and structure of porosity.

ABSTRACT

Polycrystalline, thin-sheet A/Au diffusion couples, 88 to 335 μm -thick in the diffusion direction, were studied to better understand the consequences of diffusion-induced stresses in Kirkendall couples, especially with regard to couple bending. Ag/Au couples were selected because they have practically no atomic misfit stresses but do generate large chemical stresses due to vacancy gradients. The couples, some with inert marker particles placed at their original join, were made from very pure, soft-annealed sheets which were moderately pressure-welded, then isothermally diffused, mostly at 750°C. Some of the couples were mechanically constrained from bending during diffusion by pistons held against their broad faces.

Experimental observations and simplified stress calculations indicate that the primary cause of couple bending is diffusion-induced stresses. These are generated throughout a couple when nonequilibrium vacancy concentrations in the interdiffusion zone are eliminated by destroying or creating lattice sites on either side of the couple. Couple bending is representative of high-temperature, low-stress creep deformation. Mass constraint (couple thickness parallel to the diffusion direction) retards or prevents bending by decreasing the (calculated) bending stress at the outermost, nondiffused portions of the couple. This explains why bending is not observed in the more-familiar, bulky Kirkendall couples which are much thicker in the diffusion

direction than are thin-sheet couples. In addition to causing bending, the diffusion-induced stresses also cause grain boundary sliding, destruction of original crystalline boundaries, subgrain formation, recrystallization, grain growth, and internal cracking.

Marker shifting, porosity growth, and porosity shifting also occur in thin-sheet couples. Porosity growth behavior indicates that, contrary to common belief, elastic relaxation of couple material in the direction parallel to diffusion is restrained by the mass in that direction. The rate of marker shifting in the early stage of diffusion increases when bending and porosity formation are reduced by either mass- or mechanical constraint parallel to diffusion. This suggests that bending porosity formation, and marker shifting are synergistically related by the diffusion-induced stresses which influence each of them. Thin networks of porosity are found in some of the couples, supposedly formed by heterogeneous vacancy condensation along subboundaries which were generated during diffusion. Some of the oxide marker particles become entrapped in pores during diffusion of the more-porous couples.

APPENDIX A

Thermal Expansion Bending of Thin-Sheet Couples

Upon heating, thin-sheet couples of Ag/Au undergo thermal expansion bending, much like bi-metallic thermostat strips. The direction of this bending is opposite to that encountered during interdiffusion of the strip elements, as shown in Fig. 55. The magnitude of this thermal expansion bending is calculated for the diffusion temperature of 750°C.

Calculation of the thermal expansion bending is based on the following simplifying assumptions:

1. Thermal expansion of semi-infinite diffused couple closely approximates that of an undiffused couple. This is reasonable if (1) the concentration gradient is considered linear, and (2) the expansion coefficient for all compositions changes linearly with concentration (a Vegard-type linear behavior).

2. The thermal expansion coefficient, α , is considered constant in the temperature range 25° - 750°C [strictly, $\alpha = \alpha(T)$].

Bending Calculation

Referring to Fig. 55, it is seen that the tendency for either half of the couple (Au or Ag) to expand by Δy upon heating is given by:

$$\Delta y_i = y_0 \alpha_i (T - T_0) \quad \dots 45$$

, where $i = \text{Au or Ag}$

$$y_0 = \text{couple width at } T_0$$

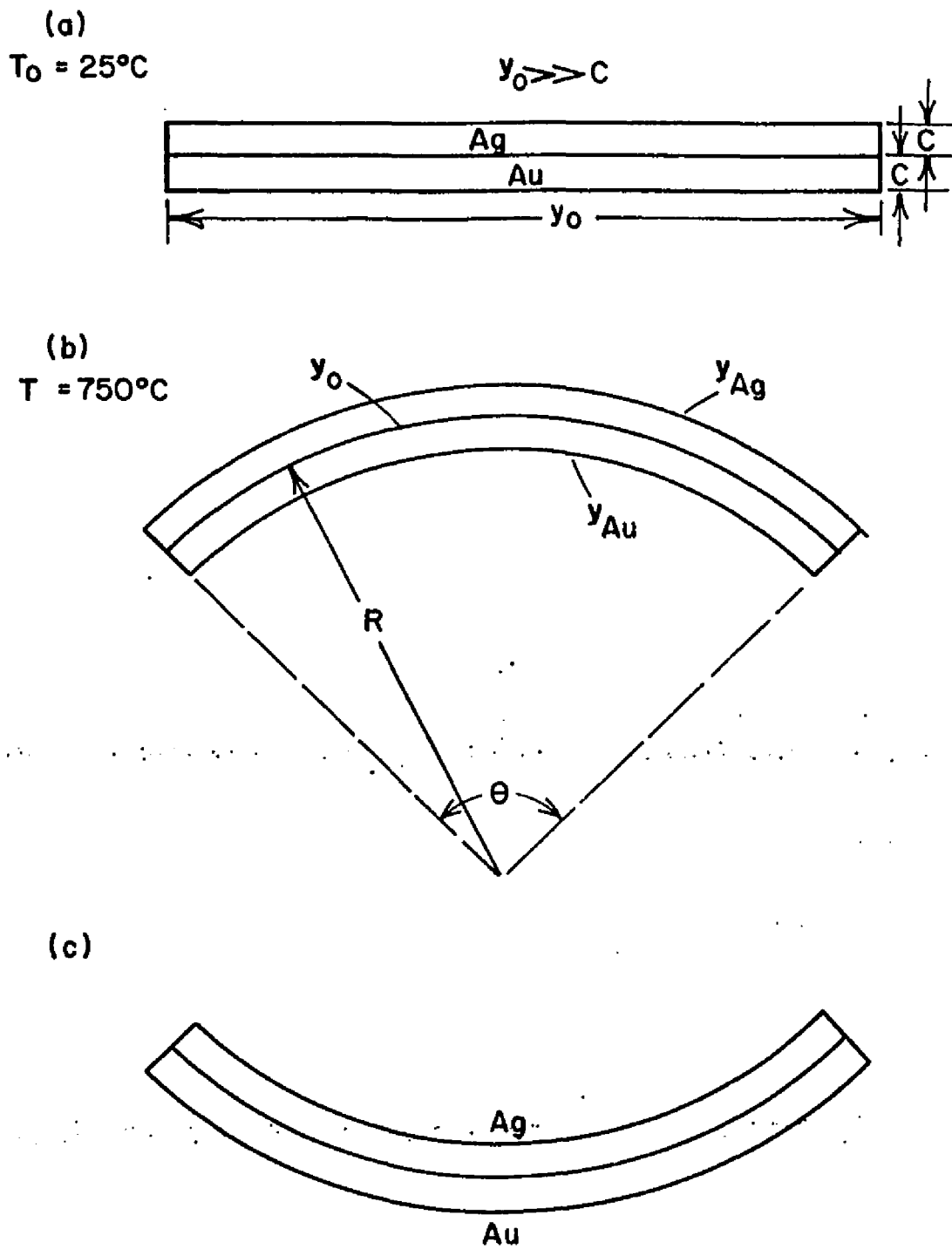


Fig. 55. Bending of thin-sheet Ag/Au couples.

(a) couple prior to heating

(b) bending induced by thermal expansion

(c) bending induced by interdiffusion

α_i = coefficient of thermal expansion, degree⁻¹

T_0, T = ambient, diffusion temperature, respectively

The arc lengths at either the pure Au or pure Ag terminal ends at the elevated temperature, T , will be

$$y_i = y_0 [1 + \alpha_i (T - T_0)] \quad \dots 46$$

The arc length ratio of Ag to Au is then

$$\frac{y_{Ag}}{y_{Au}} = \frac{1 + \alpha_{Ag} (T - T_0)}{1 + \alpha_{Au} (T - T_0)} \quad \dots 47$$

From Fig. 55,

$$y_{Ag} = (R+C)\theta \quad \dots 48(a)$$

and

$$y_{Au} = (R-C)\theta \quad \dots 48(b)$$

Eliminating θ yields

$$\frac{y_{Ag}}{y_{Au}} = \frac{R+C}{R-C} \quad \dots 49$$

Combining Eqns. 47 and 49 gives

$$\frac{R+C}{R-C} = \frac{1 + \alpha_{Ag} (T - T_0)}{1 + \alpha_{Au} (T - T_0)} \quad \dots 50$$

Values of α_i are calculated from lattice parameters according to

$$\alpha_i = \frac{a_i^T - a_i^{T_0}}{a_i^{T_0} (T - T_0)}$$

, where $a_i^{T_0}, a_i^T$ = lattice parameters at 25° and 720°C³³, respectively.

*Since $y, R \gg C$, couple expansion in the x direction is negligible and C is assumed constant.

$$\text{Then, } \alpha_{\text{Ag}} = \frac{4.1480 - 4.0862}{4.0862(720 - 25)} = 2.8 \times 10^{-5} (\text{°C})^{-1}$$

$$\text{Similarly, } \alpha_{\text{Au}} = 1.65 \times 10^{-5} (\text{°C})^{-1}$$

Employing these values of α , in addition to

$$C = 44 \mu\text{m (couple halfthickness)}$$

$$T_0 = 25^\circ\text{C}$$

$$T = 750^\circ\text{C (diffusion temperature)}$$

, yields from Eqn. 50,

$$R = 2.35 \text{ cm}$$

, which is the calculated radius of curvature due to thermal expansion bending of 88 μm -thick couples.

APPENDIX B

Measuring Shifting of Markers and Porosity

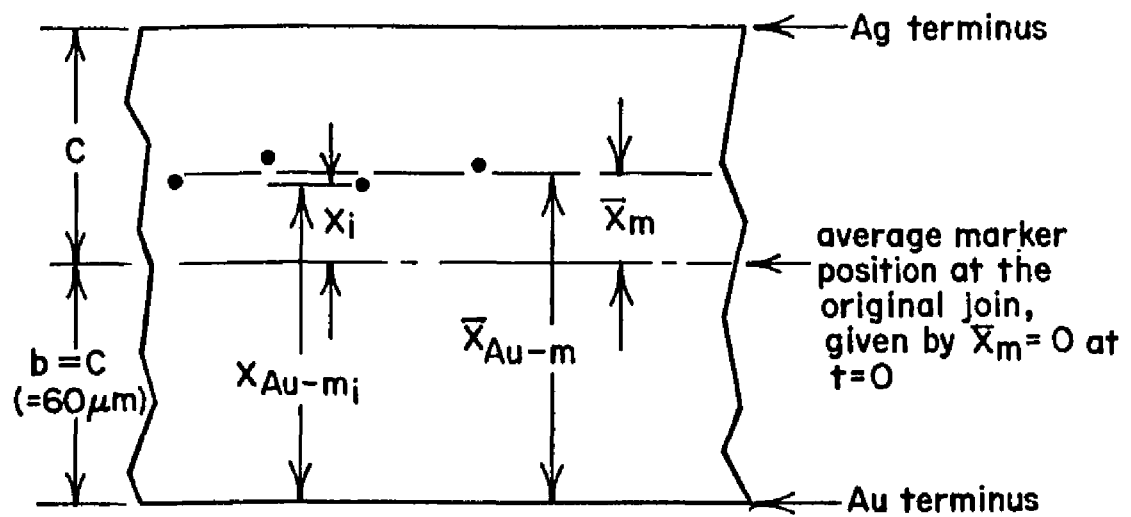
A. Marker Shifting

1. The distances from n individual markers to the Au terminus were measured in diffusion annealed couples; these are represented by X_{Au-m_i} , $i = 1, 2, 3 \dots n$, in Fig. 56(a).
2. The averages, \bar{X}_{Au-m} , from each couple in a series of like couples were plotted against $t^{\frac{1}{2}}$ ^{*}, as shown in Fig. 56(b)^{**}.
3. The $\bar{X}_{Au-m}(t)$ data were computer fitted to a parabolic rate curve ($X_m = b + k_m t^{\frac{1}{2}}$), and the intercept value, b , established the location of $\bar{X}_m = 0$ at $t = 0$, where \bar{X}_m = average marker shift from the original join. Note that position of the markers before diffusion was established directly without employing the absolute value of the couple halfthickness, C ^{***}.

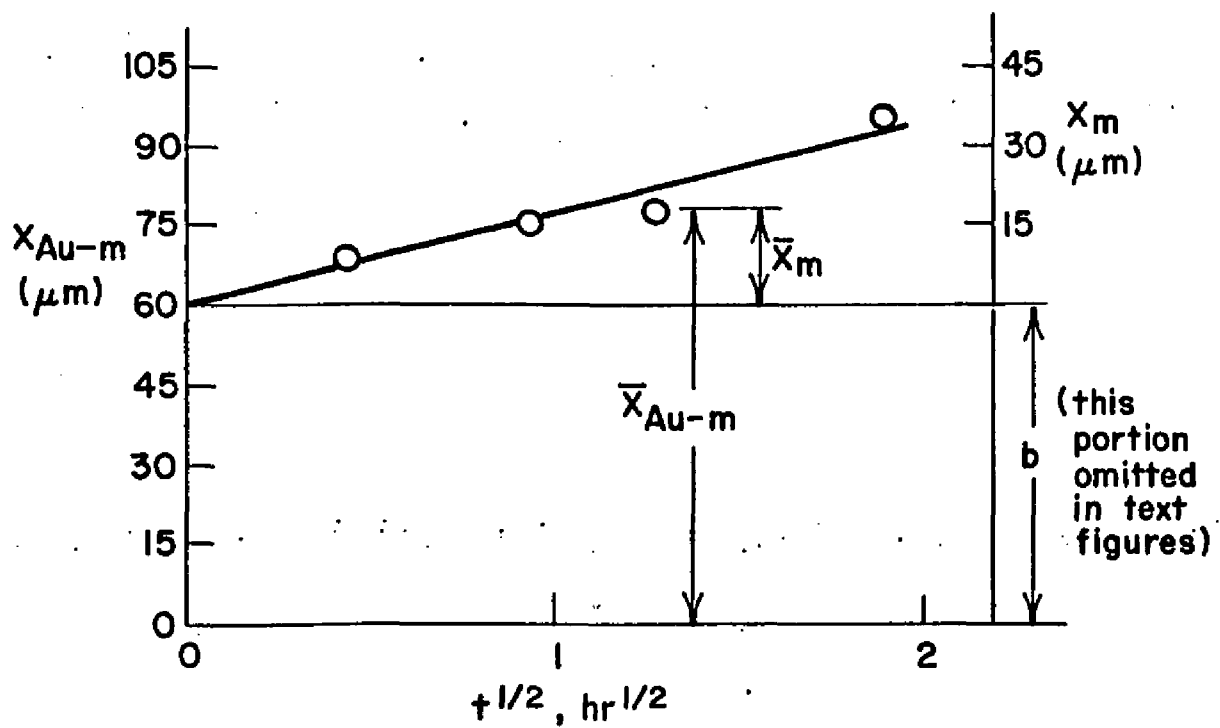
*The total diffusion time at 750°C, t , includes the nonisothermal diffusion contribution which occurred during welding and diffusion annealing.

**Marker positions within a series of like couples can be compared directly only if the sheet thicknesses of the Au half of the couples ($=C$) were identical before welding: This criterion was met for each series of marked couples by fabricating their welded disks from immediately-adjacent material along the stock sheet. This fabrication method of obtaining equal thickness was necessary because the vernier micrometers ($\pm 1.25 \mu m$ instrument precision) employed to measure C were incapable of detecting minor, yet significant, sheet-to-sheet thickness variations.

***In this experiment, establishing the position of the original join by employing the micrometer-measured value of C yielded the same parabolic marker shifting expressions which were obtained from the method of step 3.



a) marker positions in a diffused couple



b) a plot of marker shifting for a series of four like couples

Fig. 56. Marker shifting measurements and plot for a hypothetical series of like ($120 \mu\text{m}$ thick) diffusion couples.

4. Values of X_i were obtained by subtracting b from X_{Au-m_i} , as shown in Fig. 56(a).

B. Porosity Shifting

This procedure was similar to the case of marker shifting except for the following two steps.

1. The location of the centerline of the porosity zone was judged to be the density center of $\sim 95\%$ of the apparent porosity. Five or more porosity shift measurements, each made along different segments of the porosity zone, were averaged to find \bar{X}_{Au-p} of each couple.
2. The parabolic rate curve, $X_p = b + k_p t^{\frac{1}{2}}$, which fit the $\bar{X}_{Au-p}(t)$ data, could not be extrapolated to $X_p = 0$, $t = 0$ as was done in the case of marker shifting. (This extrapolation was not justified because it was not known where or when porosity was initially formed or began shifting in the couples). Therefore, the premeasured value of the Au-half of the couple ($=C$) was employed to establish the location of the original join. Accordingly, C was subtracted from the measured values, \bar{X}_{Au-p} , in order to find \bar{X}_p , the porosity shift.

C. Measuring Errors

The major sources of error in the shifting measurements were the limits of instrument precision plus the judgement errors in locating the centers of marker particles and porosity zones.

1. Marker shifting measurement errors.

These were (1) the $0.25 \mu\text{m}$ optical resolution limit of the microscope measurements which was imposed at the marker and again at the Au terminus, and (2) the estimated $0.5 \mu\text{m}$ error in locating the mass center of each marker particle. These nonsystematic inaccuracies totaled

to a maximum error of $1 \mu\text{m}$ when measuring the position of a single marker particle. However, it was unlikely that the maximum error was actually realized because nonsystematic errors in one direction usually cancel part of the nonsystematic errors in the opposite direction. The realistic measure of reliability is given then by the probable value¹²² $[\sum(\text{errors})^2]^{\frac{1}{2}}$, which in this case was $(0.25^2 + 0.25^2 + 0.5^2)^{\frac{1}{2}} \sim \pm 0.5 \mu\text{m}$. Thus, each marker datum point was considered reliable to the nearest μm .*

2. Porosity shifting measurement errors

These were (1) the same resolution limit of $0.25 \mu\text{m}$ which pertained to marker measurements, (2) an estimated $1 \mu\text{m}$ error in judging the position of the porosity zone center, and (3) a $1.25 \mu\text{m}$ precision limit of the vernier micrometers employed to measure C , the couple halfthickness. Accordingly, the maximum error was $2.75 \mu\text{m}$, and the probable error was $\sim 1.6 \mu\text{m}$.

*Measuring marker positions in typical bulky couples is usually done with light optics and mechanical stage traverses; this yields a $\pm 4 \mu\text{m}$ precision limit.³ Similar precision is obtained by using tracer techniques on radioactive oxide markers, HfO_2 .^{42,45} The greater precision in this experiment is due to marker-to-Au terminus distances being sufficiently small to permit optical grating measurements without mechanically measuring across thin-sheet couples, thereby avoiding mechanical stage errors due to gear lash, etc.

APPENDIX C

Computer Calculations of Stress Distributions Across Diffusion Couples

<u>Content</u>	<u>Page</u>
The Stress Distribution Equation and its Computer Terms.....	189
Fortran IV Program Listing for the Computer Solution of the Stress Distribution Equation.....	190
Example of Output Data: The stress distribution across the semi- infinite couple 88 μm / 750°C/ 0.5 hr, $C^2/4Dt = 18$. The plot of these data is included in Fig. 38.....	191
Table 5. Listing of computer-calculated stress distributions...	195

Multiplying both sides of Eqn. 43 by 10^{-3} yields the desired form,

$$\sigma \cdot \frac{10^{-3}}{EK_0} = \frac{x}{c^3} \left\{ \left[\exp\left(-\frac{x^2}{4Dt}\right) \right] (c^2/4Dt)^{3/2} - \frac{3}{2} \left[\exp\left(-\frac{c^2}{4Dt}\right) \right] \sum_{n=1}^{\infty} \frac{2^n (c^2/4Dt)^{\frac{2n+1}{2}}}{(2n+1)!} \right\} 10^{-3} \quad \dots 43'$$

<u>Computer Term</u>	<u>Description</u>
COUPLE THICKNESS	2C, the couple dimension parallel to the diffusion flow direction, x
SUM	the absolutely-converged ^a value of the summation term in Eqn. 43'
NO ITERATIONS	the number of iterations, n, employed in computing the value of the SUM term (n = 300, here) ^b
C SQ/4DT	$c^2/4Dt$, the factor designating the extent of interdiffusion
X(MICRONS)	the distance across the couple in a direction parallel to the diffusion flow. x = 0 at the original join (the couple center) and x = C at either terminus (free surface) of the couple
X/C	x/C, the distance across half of the couple, normalized to couple halfthickness; $x/C \leq 1$
SIGMA	the stress parameter given by the LHS of Eqn. 43'

^aabsolute convergence is proven by applying the "ratio, R, test" to

$$\sum_{n=1}^{\infty} \frac{2^n A^{\frac{2n+1}{2}}}{(2n+1)!}, \text{ where } A = (\text{variable}) \text{ constant. } \lim_{n \rightarrow \infty} R < 1 \text{ defines}$$

$$\text{absolute convergence, where } R = \frac{f(n+1)}{f(n)}, \text{ } f(n) = \frac{2^n A^{\frac{2n+1}{2}}}{(2n+1)!}$$

$$\text{and } f(n+1) = \frac{2^{n+1} A^{\frac{2n+3}{2}}}{(2n+3)!}.$$

^bThe number of iterations required to converge the SUM term for all values of $c^2/4Dt$ employed here (up to $c^2/4Dt = 85$) was found from trial calculations to be under 200. Thus, the 300 iterations are more than sufficient to converge the SUM.

```

1: C      COMPUTES CHEM STRESS FROM ADDRESS DIFFUSION COEFF
2: C      SIGMA=SIGM2*1.E-3/KB
3: C      DT=SIGM*IDEN(15)/CDT(50)/DT(50)
4:      17 READ (105,1) (IDEN(J),J=1,15),MM,Dx,CT
5:      1 FORMAT (15A4,14,2F8.6)
6:      IF (MM) 19,13,19
7:      19 M=0
8:      4 READ (105,2) (CDT(N+J),J=1,8)
9:      2 FORMAT (8F10.1)
10:     DO 7 J=1,8
11:     IF (CDT(N+J))6,7,7
12:     6 N=N+J-1
13:     GO TO 8
14:     7 CONTINUE
15:     N=N+8
16:     GO TO 4
17:     8 DO 10 J=1,N
18:     DT(J)=CT**2/CDT(J)
19:     M=0
20:     DEN=0.0
21:     SUM=0.0
22:     DO 9 L=1,MM
23:     M=M+1
24:     DEN=DEN+ALB8(2.0*FLRAT(M)+1.0)
25:     SUM = SUM+EXP((FLRAT(M)*0.69315)+(((2.0*FLRAT(M)
26:     +1+0.0)/2.0)*ALB8(CDT(J))))-DEN)
27:     9 CONTINUE
28:     X=0.0
29:     15 NN=0
30:     PRINT 11,(IDEN(J),J=1,15),SUM,MM
31:     11 FORMAT ('11'/101/101,T20,15A4/101,T20,1SUM=1,T26,
32:     1E14.7,T50,1N3,1ITERATIONS=1,T65,14/101,T20,
33:     2'IC SQ/4DT1,T32,1X(MICRONS)',T47,1X/C',T60,1SIGMA1)
34:     14 NN=NN+1
35:     X=X+DX
36:     IF (X-CT) 16,14,10
37:     16 XX=X*10000.0
38:     XC=X/CT
39:     SIG=(X*EXP(-(X**2)/DT(J)))*((CDT(J))**1.5)-(((
40:     13.0*X*EXP(-(CDT(J))/2.0)*SUM))*(1.0CF-3/CT**3)
41:     PRINT 12,CDT(J),XX,XC,SIG
42:     12 FORMAT (T21,F6.2,T33,F6.2,T45,F6.4,T55,E14.7)
43:     IF (NN=45) 14,15,15
44:     10 CONTINUE
45:     GO TO 17
46:     18 STOP
47:     END

```

Fortran IV Program Listing for the Computer Solution of the Stress

Distribution Equation 43'

CHARLETTICKNESS = 28 MICRONS

SUM = .5512527E+08

NO. ITERATIONS = 300

C SD/4BT	X (MICRONS)	Y/C	SIGMA
18.00	.25	.0057	.2200929E+02
18.00	.50	.0114	.4394058E+02
18.00	.75	.0170	.6571625E+02
18.00	1.00	.0227	.8725960E+02
18.00	1.25	.0284	.1084954E+03
18.00	1.50	.0341	.1293500E+03
18.00	1.75	.0398	.1497521E+03
18.00	2.00	.0455	.1696329E+03
18.00	2.25	.0511	.1889266E+03
18.00	2.50	.0568	.2075705E+03
18.00	2.75	.0625	.2255041E+03
18.00	3.00	.0682	.2426784E+03
18.00	3.25	.0739	.2590366E+03
18.00	3.50	.0795	.2745352E+03
18.00	3.75	.0852	.2891313E+03
18.00	4.00	.0909	.3027896E+03
18.00	4.25	.0966	.3154773E+03
18.00	4.50	.1023	.3271685E+03
18.00	4.75	.1080	.3378408E+03
18.00	5.00	.1136	.3474785E+03
18.00	5.25	.1193	.3560693E+03
18.00	5.50	.1250	.3636079E+03
18.00	5.75	.1307	.3700925E+03
18.00	6.00	.1364	.3755271E+03
18.00	6.25	.1420	.3799192E+03
18.00	6.50	.1477	.3832822E+03
18.00	6.75	.1534	.3856326E+03
18.00	7.00	.1591	.3869924E+03
18.00	7.25	.1648	.3873865E+03
18.00	7.50	.1705	.3868433E+03
18.00	7.75	.1761	.3853953E+03
18.00	8.00	.1818	.3830784E+03
18.00	8.25	.1875	.3799292E+03
18.00	8.50	.1932	.3759883E+03
18.00	8.75	.1989	.3712983E+03
18.00	9.00	.2045	.3659031E+03
18.00	9.25	.2102	.3598486E+03
18.00	9.50	.2159	.3531809E+03
18.00	9.75	.2216	.3459422E+03
18.00	10.00	.2273	.3381980E+03
18.00	10.25	.2330	.3299790E+03
18.00	10.50	.2386	.3213396E+03
18.00	10.75	.2443	.3123269E+03
18.00	11.00	.2500	.3029885E+03
18.00	11.25	.2557	.2933713E+03

Example of Output Data

COUPLE THICKNESS = 28 MICRONS

GUNE = .5319527E+08

NO. ITERATIONS= 300

C	SO/40T	X(MICRONS)	X/C	SIGMA
18.00		11.50	.2614	.2835200E+03
18.00		11.75	.2670	.2734792E+03
18.00		12.00	.2727	.2632917E+03
18.00		12.25	.2784	.2529933E+03
18.00		12.50	.2841	.2426385E+03
18.00		12.75	.2898	.2322495E+03
18.00		13.00	.2955	.2218672E+03
18.00		13.25	.3011	.2115246E+03
18.00		13.50	.3068	.2012536E+03
18.00		13.75	.3125	.1910831E+03
18.00		14.00	.3182	.1810392E+03
18.00		14.25	.3239	.1711474E+03
18.00		14.50	.3295	.1614295E+03
18.00		14.75	.3352	.1519063E+03
18.00		15.00	.3409	.1425956E+03
18.00		15.25	.3466	.1335129E+03
18.00		15.50	.3523	.1246722E+03
18.00		15.75	.3580	.1160353E+03
18.00		16.00	.3636	.1077616E+03
18.00		16.25	.3693	.9970982E+02
18.00		16.50	.3750	.9193515E+02
18.00		16.75	.3807	.8444258E+02
18.00		17.00	.3864	.7723485E+02
18.00		17.25	.3920	.7031316E+02
18.00		17.50	.3977	.6367787E+02
18.00		17.75	.4034	.5732733E+02
18.00		18.00	.4091	.5125909E+02
18.00		18.25	.4148	.4546983E+02
18.00		18.50	.4205	.3995502E+02
18.00		18.75	.4261	.3470906E+02
18.00		19.00	.4318	.2972618E+02
18.00		19.25	.4375	.2499942E+02
18.00		19.50	.4432	.2052153E+02
18.00		19.75	.4489	.1628467E+02
18.00		20.00	.4545	.1228062E+02
18.00		20.25	.4602	.8500906E+01
18.00		20.50	.4659	.4936779E+01
18.00		20.75	.4716	.1579216E+01
18.00		21.00	.4773	-.1580631E+01
18.00		21.25	.4830	-.4552066E+01
18.00		21.50	.4886	-.7343979E+01
18.00		21.75	.4943	-.9965438E+01
18.00		22.00	.5000	-.1242532E+02
18.00		22.25	.5057	-.1473237E+02
18.00		22.50	.5114	-.1629525E+02

Example of Output Data

COUPLE THICKNESS = 88 MICRONS

SUM = .5419507E+08

NO. ITERATIONS = 300

C 50/40T	X (MICRONS)	X/C	SIGMA
18.00	22.75	.5170	-.1892229E+02
18.00	23.00	.5227	-.2082162E+02
18.00	23.25	.5284	-.2260118E+02
18.00	23.50	.5341	-.2426454E+02
18.00	23.75	.5398	-.2583102E+02
18.00	24.00	.5455	-.2729572E+02
18.00	24.25	.5511	-.2866933E+02
18.00	24.50	.5568	-.2995327E+02
18.00	24.75	.5625	-.3116964E+02
18.00	25.00	.5682	-.3230627E+02
18.00	25.25	.5739	-.3337459E+02
18.00	25.50	.5795	-.3438483E+02
18.00	25.75	.5852	-.3533585E+02
18.00	26.00	.5909	-.3623422E+02
18.00	26.25	.5966	-.3708424E+02
18.00	26.50	.6023	-.3788997E+02
18.00	26.75	.6080	-.3865508E+02
18.00	27.00	.6136	-.3938313E+02
18.00	27.25	.6193	-.4007736E+02
18.00	27.50	.6250	-.4074075E+02
18.00	27.75	.6307	-.4137613E+02
18.00	28.00	.6364	-.4198604E+02
18.00	28.25	.6420	-.4257235E+02
18.00	28.50	.6477	-.4313879E+02
18.00	28.75	.6534	-.4368584E+02
18.00	29.00	.6591	-.4421584E+02
18.00	29.25	.6648	-.4473048E+02
18.00	29.50	.6705	-.4523128E+02
18.00	29.75	.6761	-.4571967E+02
18.00	30.00	.6818	-.4619690E+02
18.00	30.25	.6875	-.4666418E+02
18.00	30.50	.6932	-.4712254E+02
18.00	30.75	.6989	-.4757289E+02
18.00	31.00	.7045	-.4801616E+02
18.00	31.25	.7102	-.4845314E+02
18.00	31.50	.7159	-.4888443E+02
18.00	31.75	.7216	-.4931073E+02
18.00	32.00	.7273	-.4973262E+02
18.00	32.25	.7330	-.5015056E+02
18.00	32.50	.7386	-.5056502E+02
18.00	32.75	.7443	-.5097641E+02
18.00	33.00	.7500	-.5138513E+02
18.00	33.25	.7557	-.5179144E+02
18.00	33.50	.7614	-.5219571E+02
18.00	33.75	.7670	-.5259808E+02

Example of Output Data

CHIEF THICKNESS = 89 MICRONS

SUM = .5319597E+02

NO. ITERATIONS = 300

C	SN/40T	X (MICRONS)	X/C	SIGMA
	18.00	34.00	.7727	-.5299889E+02
	18.00	34.25	.7784	-.5339825E+02
	18.00	34.50	.7841	-.5379639E+02
	18.00	34.75	.7898	-.5419348E+02
	18.00	35.00	.7955	-.5458941E+02
	18.00	35.25	.8011	-.5498491E+02
	18.00	35.50	.8068	-.5537950E+02
	18.00	35.75	.8125	-.5577348E+02
	18.00	36.00	.8182	-.5616695E+02
	18.00	36.25	.8239	-.5655992E+02
	18.00	36.50	.8295	-.5695251E+02
	18.00	36.75	.8352	-.5734474E+02
	18.00	37.00	.8409	-.5773671E+02
	18.00	37.25	.8466	-.5812839E+02
	18.00	37.50	.8523	-.5851984E+02
	18.00	37.75	.8580	-.5891110E+02
	18.00	38.00	.8636	-.5930225E+02
	18.00	38.25	.8693	-.5969321E+02
	18.00	38.50	.8750	-.6008405E+02
	18.00	38.75	.8807	-.6047479E+02
	18.00	39.00	.8864	-.6086545E+02
	18.00	39.25	.8920	-.6125603E+02
	18.00	39.50	.8977	-.6164651E+02
	18.00	39.75	.9034	-.6203691E+02
	18.00	40.00	.9091	-.6242726E+02
	18.00	40.25	.9148	-.6281763E+02
	18.00	40.50	.9204	-.6320793E+02
	18.00	40.75	.9261	-.6359821E+02
	18.00	41.00	.9318	-.6398846E+02
	18.00	41.25	.9375	-.6437869E+02
	18.00	41.50	.9432	-.6476888E+02
	18.00	41.75	.9489	-.6515909E+02
	18.00	42.00	.9545	-.6554927E+02
	18.00	42.25	.9602	-.6593945E+02
	18.00	42.50	.9659	-.6632964E+02
	18.00	42.75	.9716	-.6671980E+02
	18.00	43.00	.9773	-.6710994E+02
	18.00	43.25	.9829	-.6750008E+02
	18.00	43.50	.9886	-.6789026E+02
	18.00	43.75	.9943	-.6828040E+02
	18.00	44.00	1.0000	-.6867053E+02

STOP C

Example of Output Data

Table 5. Listing of computer-calculated stress distributions.

<u>Couple thickness</u> <u>μm</u>	<u>Interval of stress calculation,</u> <u>μm</u>	<u>Values assigned to $C^2/4Dt$</u>
----- Hypothetical Couples -----		
20	0.10	4, 8, 16, 18, 32, 64
40	0.10	4, 8, 16, 18, 32, 64
60	0.10	4, 8, 16, 18, 32, 64
80	0.25	4, 8, 16, 18, 32, 64
100	0.25	4, 8, 16, 18, 32, 64
140	0.25	4, 8, 16, 18, 32, 64
180	0.25	4, 8, 16, 18, 32, 64
220	0.25	4, 8, 16, 18, 32, 64
260	0.25	4, 8, 16, 18, 32, 64
300	0.10	4, 5, 6, 8, 9, 10, 11, 12, 14, 16, 18, 24, 32, 40, 48, 56, 64
340	1.0	4, 8, 16, 18, 32, 64
400	1.0	4, 8, 16, 18, 32, 64
600	2.0	4, 8, 16, 18, 32, 64
1,000	10.0	4, 16, 18
10,000	100.0	4, 16, 18
----- Experimental Couples ^a -----		
88	0.25	4, 5, 5.87, 6, 7, 8, 9, 10, 12, 14, ... 40, 44, 48 ... 80
170	0.25	4, 9, 18, 21.9
335	0.25	4, 9, 18, 57.6, 85

^a Several of the values of $C^2/4Dt$ represent actual experimental couples, others were assigned in order to aid general analysis of stress distributions.

APPENDIX D

Suggested Experiment: The Relationship Between Porosity, Marker Shifting, and Couple Bending

The results of this research indicated a stress-related synergism between porosity, marker shifting, and bending. This result requires a systematic confirmation of the type suggested here.

1. Prepare several thin-sheet Ag/Au couples of various thicknesses which experience bending during 750°C diffusion, say 40, 80, and 120 μm .
2. Marker all couples with iron oxide particles.
3. Apply shallow welds (few μm) so that various semi-infinite diffusion anneals may be applied.
4. Diffuse at 750°C under various hydrostatic pressures in order to vary the amount of porosity. Commercially-available argon will do this conveniently. Pressures which totally eliminate porosity (1,500 psi) will not alter the diffusion kinetics (see references 40, 44, 54, 71).
5. Measure bending, marker shifting, and porosity volume.*

*Porosity volume measurements cannot be made via conventional metallographic preparation. It is likely that it can be determined by (1) preparing conventional metallographic cross sections, lightly etched, (2) deep-plating and preserving the exposed porosity with (Watt's bath) nickel, (3) regrinding lightly with 2/0 or 4/0 SiC paper, and (4) final polishing with diamond and/or $\alpha\text{-Al}_2\text{O}_3$. If this fails to adequately preserve the porosity, alternate porosity-filling methods might be tried, such as electroless plating or vacuum-impregnation with epoxy.

6. Analyze the results with regard to the trade-off synergisms between porosity, marker shifting, and bending.
7. Useful microstructural information concerning the formation and shape of porosity might also be obtained from the couple.

LIST OF REFERENCES

1. Seeger, A., Jnl. Less-Common Metals, 28, 387 (1972).
2. Smigelskas, A. D. and Kirkendall, E. O., Trans. AIME, 171, 130 (1947).
3. da Silva, L. C. C. and Mehl, R. F., Trans. AIME, 191, 155 (1951).
4. Kuczynski, G. C. and Alexander, B. H., Jnl. Appl. Phys., 22, no. 3, 344 (1951).
5. Balluffi, R. W. and Alexander, B. H., Jnl. Appl. Phys., 23, 1237 (1952).
6. Barnes, R. S., Proc. Phys. Soc., 65B, 512 (1952).
7. Bardeen, J. and Herring, C., in Atom Movements, Cleveland, Ohio: The Am. Soc. for Metals, 1951, p. 87.
8. Brinkman, J. A., Acta Met., 3, 140 (1955).
9. Balluffi, R. W. and Seigle, L. L., Acta Met., 3, 170 (1955).
10. Balluffi, R. W. and Seigle, L. L., Acta Met., 5, 449 (1957).
11. Smith, C. S., Trans. AIME, 171, 136 (1947).
12. Doo, V. Y. and Balluffi, R. W., Acta Met., 6, 428 (1958).
13. Ayres, P. S., PhD. dissertation, Purdue University, Indiana, 1968.
14. Matthews, J. W. and Crawford, J. L., Phil Mag., 11, 977 (1966).
15. Matthews, J. W. and Jesser, W. A., Jnl. Vac. Sci. and Technol., 6, no. 4, 641 (1969).
16. Queisser, H. J., Jnl. Appl. Phys., 32, no. 9 1776 (1961).
17. Prussin, S., Jnl. Appl. Phys., 32, no 10, 1876 (1961).
18. Schwuttke, G. H. and Queisser, H. J., Jnl. Appl. Phys., 33, 1540 (1962).
19. Jaccodine, R. J., Appl. Phys. Letters, 4, no. 6, 114 (1964).

20. Joshi, M. L. and Wilhelm, F., Jnl. Electrochem. Soc., 112, 185 (1965).
21. McDonald, R. A., Ehlenberger, G. G., and Huffman, T. R., Solid St. Elect., 9, 807 (1966).
22. Czaja, W., Jnl. Appl. Phys., 37, 3441 (1966).
23. Levine, E., Washburn, J., and Thomas, G., Jnl. Appl. Phys., 38, 81 (1967).
24. *ibid*, p. 87.
25. Lambert, J. L., Phys. Stat. Sol. (a), 4, K33 (1971).
26. Ravi, K. V., Met. Trans., 3, no. 5, 1311 (1972).
27. Liu, Y. H. and Powell, G. W., Trans. AIME, 239, 998 (1967).
28. Bolk, A., Acta Met., 9, 632 (1961).
29. Goldman, A. J., Jordan, R. W., and Winter, J., Trans. AIME, 242, 295 (1968).
30. Reynolds, J. E., Averbach, B. L., and Cohen, Morris, Acta Met., 5, 29 (1957).
31. Ruth, V., Trans. AIME, 227, 778 (1962).
32. (a)--Gerken, J. M. and Owczarski, W. A., Weld. Res. Council Bull., no. 109, 1 (1956).
(b)--Kharchenko, G. K., Automatic Welding, 18, no. 2, 30 (1965).
(c)--Budge, J., van Hann, F. J., and Edwards, C., Vacuum, 21, no's 3 and 4, 99 (1971).
(d)--Weisner, P., Metal Constr. Brit. Weld. Jnl., 3, no. 3 (1971).
(e)--Alm, G. W., Adhesives Age, 31 (Sept. 1970).
33. Warlimont, H., Z. Metallk., 50, 708 (1959).
34. Pearson, W. B., Lattice Spacings and Structures of Metals and Alloys, vol. 2, New York: Pergamon, 1967, p. 80.
35. Kubaschewski, O. and Catterall, J. A., Thermochemical Data of Alloys, New York: Pergamon, 1956, p. 65.
36. Hansen, M., Constitution of Binary Alloys, New York: McGraw-Hill, 1958, p. 37.

37. Bolk, A., Acta Met., 9, 643 (1961).
38. Johnson, W. A., Trans. AIME, 147, 331 (1942).
39. Mallard, W. C., Gardner, A. B., Bass, R. F. and Slifkin, L. M., Phys. Rev., 129, no. 2, 617 (1963).
40. Albrecht, E. D. and Tomizuka, C. T., Jnl. Appl. Phys., 35, no. 12, 3560 (1964).
41. Cook, H. E. and Hilliard, J. E., Appl. Phys. Letters, 7, no. 12, 24 (1965).
42. Meyer, R. O. and Slifkin, L. M., Phys. Rev., 149, no. 2, 556 (1966).
43. Furnish, J., "Solid State Diffusion of Gold and Silver; A Literature Search" Los Alamos Report no. LA-3806-MS, Springfield, Va. 22151; U. S. Department of Commerce, Nov. 30, 1967.
44. Meyer, R. O., Phys. Rev., 181, no. 3, 1086 (1969).
45. Greene, M. H., Batra, A. P., Lowell, R. C., Meyer, R. O., and Slifkin, L. M., phys. stat. sol. (a), 5, 365 (1971).
46. Ziebold, T. O. and Ógilvie, R. E., Analytical Chem., 36, no. 2 322 (1964).
47. Smoluchowski, R., Trans. AIME, 171, 135 (1947).
48. Mehl, R. F., Trans. AIME, 171, 135 (1947).
49. Darken, L. S., Trans. AIME, 171, 138 (1947).
50. Darken, L. S., Trans. AIME, 175, 184 (1948).
51. Boltzmann, L., Wied. Ann., 53, 959 (1894).
52. Matano, C., Jap. Jnl. Physics, 8, 109 (1933).
53. Kohn, A., Levasseur, J., Philibert, J., and Wanin, M., Acta Met., 18, no. 1, 163 (1970). See especially their Fig. 9.
54. Clay, B. D. and Greenwood, G. W., Phil. Mag., 25, no. 5, 1201 (1972).
55. Seith, W. and Heumann, T., Diffusion of Metals: Exchange Reactions, 1955, transl. by the United States Atomic Energy Comm., AEC-tr-4506; OTS, Dept. of Commerce, Washington, D. C., 1962, p. 132.

56. Hartley, C. S., Steedly, J. E., and Parsons, L. D., in Diffusion in Body-Centered Cubic Metals, Metals Park, Ohio: Am. Soc. Metals, 1965, p. 51.
57. Dallwitz, M. J., Acta Met., 20, 1229 (1972).
58. Seitz, F., Phys. Rev., 74, 1513 (1948).
59. Zener, C., Acta Cryst., 3, 346 (1950).
60. Mott, N. F., Proc. Phys. Soc., B64, 729 (1951).
61. Fisher, J. C., Hollomon, H. H., and Turnbull, D., Trans. AIME, 202 (1948).
62. Bardeen, J., Phys. Rev., 76, 1403 (1949).
63. Bardeen, J. and Herring, C., Imperfections in Nearly Perfect Crystals, John Wiley and Sons: New York, 1952, p. 261.
64. Shockley, W., private communication, Seitz, F., Phys. Rev., 79, 722 (1950).
65. Amelinckx, A., Bontinck, W., Dekeyser, W., and Seitz, F. Phil. Mag., 2, 355 (1957).
66. Hirth, J. P. and Lothe, J., Theory of Dislocations, New York: McGraw-Hill, 1968, p. 568.
67. Weertman, J. and Weertman, J. R., Elementary Dislocation Theory, New York: MacMillan, 1964, pp. 57, 72-77.
68. Hirth and Lothe, *loc. cit.*, p. 564.
69. Westmacott, K. H., Barnes, R. S., and Smallman, R. E., Phil. Mag., 7, no. 8, 1585 (1962).
70. Amelinckx, S., Solid State Phys., Supp. 6, "The Direct Observation of Dislocations", New York: Academic, 1964, pp. 378-380.
71. Barnes, R. S. and Mazey, D. J., Acta Met., 6, 1 (1958).
72. Seitz, F., Acta Met., 1, 355 (1953).
73. Sundquist, B. E., Acta Met., 12, 67 (1964).
74. Beeré, W. and Reynolds, G. L., Acta Met., 20, 845 (1972).
75. Norris, D. I. R., Phil Mag., 23, no. 181, 135 (1971).
76. Balluffi, R. W., Acta Met., 2, 194 (1954).

77. Seith and Heumann, 1955, loc. cit., pp. 137-9.
78. Pearson, G. L. and Bardeen, J., Phys. Rev., 75, no. 5, 865 (1949).
79. Cathcart, J. V., in Oxidation of Metals and Alloys, Ohio: Am. Soc. Metals, 1971, p. 27.
80. Kellerer, H. K. and Wingert, L. W., Met. Trans., 2, no. 1, 113 (1971).
81. Turnbull, D. in Atom Movements, Cleve., Ohio: Am. Soc. Metals, 1951, p. 129.
82. Turnbull, D. and Hoffman, R. E., Acta Met., 2, 419 (1954).
83. Quere, Y., Conf. Jnl. Phys. Soc. Japan, 18, supp. 111, 91 (1963).
84. Jeannotte, D. and Machlin, E. S., Phil. Mag., 8, 1835 (1963).
85. Clarebrough, L. M., Segall, R. L., Loretto, M. H., and Hargreaves, M. E., Phil. Mag., 9, 377 (1964).
86. Richardson, F. D. and Jeffes, J. H. E., Jnl. Iron Steel Inst., 160, 261 (1948).
87. Ham, J. L., Parke R. M., Herzig, A. J., Trans. ASM, 31, 849 (1943).
88. Metals Handbook, 8th ed., vol. 1, Metals Park, Ohio: Am. Soc. Metals, 1961, p. 422.
89. Graphite Products Division, Bulletin no. 115, The Carborundum Co., Sanborn, N. Y. 14132, approximately 1969.
90. Love, G. R. and Shewmon, P. G., Acta Met., 11, 899 (1963).
91. Robinson, J. T., PhD. dissertation, U. of Texas at Austin, 1970.
92. Ruth, V. and Powell, G. W., Acta Met., 12, no. 2, 264 (1964).
93. Powell, G. W. Trans. AIME, 233, 1906 (1965).
94. Ziebold, T. O., The Electron Microanalyzer and Its Application, Ziebold, T. O. (ed.), Cambridge, Mass., Massachusetts Institute of Technology, 1965, p. S-3.
95. Reiswig, R. D., Microstructures, 1, no. 2, 15 (1970).
96. Hartley, C. S. and Hubbard, K., "A Computer Program for the Mantano Analysis of Binary Diffusion Data", ASD-TDR-62-858, Nov. 1962, avail. at OTS, Dept. of Commerce, Washington 25, D. C.

97. Moon, D. M., and Robinson, W. H., Canad. Jnl. Phys., 45, 1017 (1967).
98. Raj, R. and Ashby, M. F., Met. Trans., 3, no. 7, 1937 (1972).
99. Garofalo, F., Fundamentals of Creep and Creep-Rupture in Metals, New York: Macmillan, 1965, p. 111.
100. Cuddy, L. J., Met. Trans., 1, 395 (1970).
101. Amelinckx, S., Solid State Phys., Supp. 6, loc. cit., p. 336.
102. Shewmon, P. G., Diffusion in Solids, New York: McGraw-Hill, 1963, p. 129.
103. Fraikor, F. J., and Hirth, J. P., Jnl. Appl. Phys., 38, No. 5, 2312 (1967).
104. Timoshenko, S. and Goodier, J. N., Theory of Elasticity, 2nd ed., New York: McGraw-Hill, 1951, p. 399.
105. Sherby, O., Acta Met., 10, 135 (1962)
106. Sherby, O. D. and Burke, P. M., "Mechanical Behavior of Crystalline Solids at Elevated Temperatures", in Progress in Materials Science, B. Chalmers and W. Hume-Rothery, eds., 13, no. 7, New York: Pergamon, 1968, p. 358.
107. Makin, S. M., Rowe, A. H., and LeClaire, A. D., Proc. Phys. Soc., (London), B70, 545 (1957).
108. Garofalo, F., loc. cit., p. 50.
109. Sherby and Burke, loc. cit., p. 342.
110. Weertman, J., ASM Trans. Quart., 61, 681 (1968).
111. Jones, H., Mater. Sci. Eng., 4, 113 (1968).
112. Sherby and Burke, loc. cit., p. 358.
113. Crank, J., The Mathematics of Diffusion, Oxford Univ. Press, 1956, p. 15.
114. Heumann, V. T. and Kottmann, A., Z. Metallkunde, 44, 139 (1953).
115. Bokshtein, S. Z., in Diffusion Processes, Structure, and Properties of Metals, S. Z. Bokshtein, Ed., transl. by Consultants Bureau Enterprises, Inc., New York, 1965, p. 2.

116. Balluffi, R. W., Lie, K. H., and Seidman, D. N., in Vacancies and Interstitials in Metals, A. Seeger et al., eds., New York: American Elsevier Publ., 1970, p. 134.
117. Hirth, J. P., Met. Trans., 3, 3047 (1972).
118. Bückle, H. and Blin, J., Jnl. Inst. Metals, 80, 385 (1951/52).
119. Seith and Heumann, 1955, loc. cit., p. 133.
120. Seith, W. and Ludwig, R., Z. Metallkunde, 45, 401 (1954): reported in Seith and Heumann, 1955, loc. cit., p. 140.
121. LeClaire, A. D. and Barnes, R. S., Jnl. Metals, 3, 1060 (1951).
122. Fogel, C. M., Introduction to Engineering Computations, International Textbook, Co.: Scranton, Pa., 1960, p. 93.

